Universita' di Siena

Doctorate School in Physics

Thesis

Design and Characterization of Optical Cavities and Length Sensing and Control System of an Advanced Gravitational Wave Interferometer

---

Candidate:
Alberto Stochino

Supervisor:
Prof. Rana Adhikari
California Institute of Technology

Tutor:
Prof. Piersimone Marrocchesi
Università di Siena

14 November 2010

Ai miei genitori

Abstract

The international network of interferometric gravitational wave detectors has passed its first generation and is now entering an advanced phase that will bring it closer to the realm of routine astronomy. This transition began with the construction of the second generation of the Laser Interferometric Gravitational wave Observatory (Advanced LIGO) and will continue with Advanced Virgo and LCGT. The advanced detectors, expected to reach a sensitivity of 10^{-20} m/$\sqrt{\text{Hz}}$, will be able to detect gravitational radiation from massive black hole mergers and black hole or neutron star inspirals into massive black holes out to a distance of 180 megaparsec.

To achieve the design sensitivity, gravitational wave interferometers will implement an advanced optical configuration and new subsystems designed to improve the signal-to-noise ratio to the limits imposed by fundamental noise sources such as optics thermal noise and laser shot noise. Technical noise suppression will be largely obtained by the optical cancellation occurring at the readout port of the interferometer and by hundreds of control loops designed to maintain the system at its optimal working point. Much of interferometer design is thus devoted to defining the optimal optical parameters that ensure the best performance.

As with any construction plan, the optical design must include tolerance margins prescribing acceptable ranges of variability of the actual system parameters from their nominal values. To this end, we considered the effects on the interferometer performance of length mismatches of the main optical cavities from their nominal values and arm length asymmetries. The LIGO Caltech 40m advanced gravitational wave interferometer prototype has been the ideal model for our analysis. We studied how the control signals used to keep the interferometer at its working point may be altered by macroscopic length offsets in any of the optical cavities. In particular we analyzed how these offsets may affect the length sensing and control scheme of the interferometer.

Frequency and amplitude noise on the input laser beam can couple into the gravitational wave channel, limiting the detector sensitivity. In this thesis we studied how these noise couplings depend on asymmetries of the system arising from length mismatches between the cavities. Applying the results from our analysis of controls and of noise couplings, we defined tolerance margins on the precision of cavity lengths.

A measuring tool is necessary to implement lengths and tolerances as defined by the optical design. We present here an interferometric technique that we developed to measure

the absolute length of the optical cavities with a precision of order of 10^{-6}. This technique is useful to characterize the optical cavities and diagnose the interferometer performance at any time. We demonstrated how a variation of this approach can also be used to perform metrology measurements on the mirrors of the optical cavities.

Finally we show how we applied the results from the cavity length analysis to adjust the optical design of the Caltech 40m interferometer, and to design and build the length sensing and control RF system used for interferometer locking.

Contents

List of Tables

List of Figures

Chapter 1

Gravitational Waves

In this chapter we introduce gravitational waves as solutions to the equations of general relativity. We discuss their nature and their sources in the universe. Finally we present the interferometric technique used to detect the effect of gravitational waves on mass distributions.

1.1 Gravitational waves from Einstein's equations

The theory of General Relativity (GR) describes space-time as a 4-dimensional differential manifold, with a metric defined by a covariant, second rank, symmetric tensor denoted by $g_{\mu\nu}$ [1]. From the metric, the invariant differential interval ds is obtained as

$$ds^2 = g_{\mu\nu} dx^\mu dx^\nu. \tag{1.1}$$

Within this theory, matter determines the metric of space-time. The equations of motion emerge as a result of the tendency of bodies to follow geodesic trajectories. Einstein's equations synthesize this matter-metric dependence by defining a tensor $G_{\mu\nu}$, the *Einstein tensor*, function of the metric, and a tensor $T_{\mu\nu}$, the *stress-energy tensor*, embodying the description of the mass distribution. The relationship between these tensors is

$$G_{\mu\nu} = \frac{8\pi G}{c^4} T_{\mu\nu} \tag{1.2}$$

where G is Newton's constant, and c the speed of light.

Near a source, the effect of mass on the metric can be large, but, from far away, a weak-field approximation allows us to describe the effect of gravitational fields as perturbations to a flat space Minkowski metric $\eta_{\mu\nu}$, such that:

$$g_{\mu\nu} \simeq \eta_{\mu\nu} + h_{\mu\nu}. \tag{1.3}$$

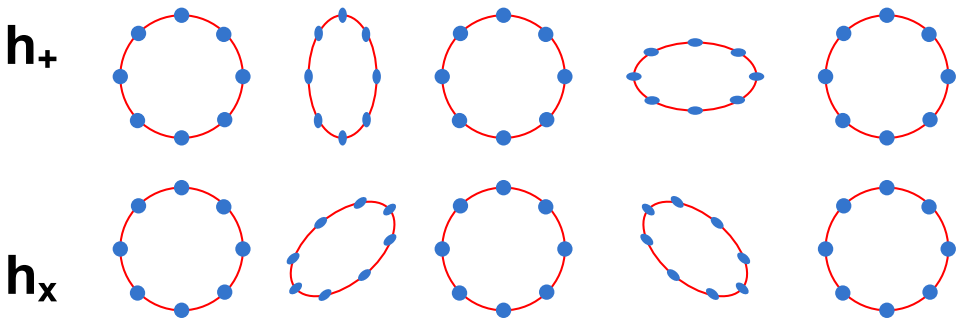

Figure 1.1: Effects on a circular lumped mass distribution of the two possible polarizations of gravitational wave radiation h_+ and $h_\times$.

In the approximation that $T_{\mu\nu}$ does not depend on $h_{\mu\nu}$, 1.2 becomes

$$\Box h_{\mu\nu} = -16\pi T_{\mu\nu} \tag{1.4}$$

where $\Box = -\partial^2 t + \nabla$ is the flat-space d'Alembertian operator. In the far field approximation 1.4 becomes

$$\Box h_{\mu\nu} = 0 \tag{1.5}$$

which is the wave equation. The solutions, in a traceless gauge, for a wave propagating along the z-axis, can be written as:

$$h_{\mu\nu} = \begin{pmatrix} 0 & 0 & 0 & 0 \\ 0 & h_+ & h_\times & 0 \\ 0 & h_\times & -h_+ & 0 \\ 0 & 0 & 0 & 0 \end{pmatrix} e^{i(\omega t - kz)} \tag{1.6}$$

where h_+ and $h_\times$ denote the two main polarizations.

1.1.1 Effect of gravitational waves on mass distributions

The effect of an incoming gravitational wave, as in 1.6, on the distance between two test masses located on the x-axis and separated by a distance L can be simply calculated. For instance, in the case of h_+ polarization:

$$L(x_1, x_2) = \int_0^{L_0} \sqrt{|g_{xx}|}\, dx \simeq L_0 \left(1 - \frac{h_+}{2}\right) \tag{1.7}$$

which implies that the distance L fluctuates by a fraction

$$\frac{\delta L}{L} = \frac{h_+}{2}. \tag{1.8}$$

This effect forms the basis of interferometric gravitational wave detection, as it is discussed in section 1.3. Figure 1.1 shows the effect of the two polarizations on a lumped mass distribution.

1.2 Gravitational wave sources

The sources of gravitational waves are events involving the dynamics of peculiar mass distributions. Energy conservation implies that only quadrupole terms of $T_{\mu\nu}$ can radiate.

Because of that, gravitational radiation is quite different from electromagnetic radiation. While photons are emitted in the outer layers of astrophysical bodies, gravitational waves are the products of the dynamics of their inner structure. This allows them to carry information otherwise inaccessible through optical observation.

1.2.1 Amplitude

From [2, 3], we can roughly estimate the order of magnitude of gravitational waves from an astrophysical source, by a dimensional argument. If we denote with Q the quadrupole moment of the source, then

$$h \sim \frac{G\ddot{Q}}{c^4 r} \sim \frac{G}{c^4}\frac{E_{kin}^{ns}}{r} \sim 10^{-19}\left(\frac{E_{kin}^{ns}}{M_\odot c^2}\right)\left(\frac{1\text{ Mpc}}{r}\right) \tag{1.9}$$

where E_{kin}^{ns} is the non symmetric part of the kinetic energy of the system, and r the distance from Earth. Assuming $E_{kin}^{ns} \sim M_\odot c^2$, the gravitational wave amplitude from an intergalactic source or a source at cosmological distance would be

$$\begin{aligned} h &\lesssim 10^{-21} \quad \text{intergalactic distance} \\ h &\lesssim 10^{-23} \quad \text{Hubble distance} \end{aligned}$$

1.2.2 Frequency

Applying a similar dimensional argument, we can also roughly estimate the upper limit frequency of a radiating source. Considering that the size of the source cannot exceed its Schwarzshild radius $2GM/c^2$, and the wave period cannot be shorter than the time taken by light to go around its circumference, the frequency must be limited by

$$f \leq \frac{c^3}{4\pi GM} \sim 10^4\text{ Hz}\frac{\mathrm{M}_\odot}{\mathrm{M}}. \tag{1.10}$$

1.2.3 Sources

Because of the small amplitude of gravitational waves, only massive astrophysical objects are good candidates for observation. An extensive analysis of sources is given in [1]. Here we cite only some:

- *coalescing compact binaries*: consisting of either two neutron stars, two black holes or one of each
- *binary stars*

- *rotating neutron stars*: detectable for non axis-symmetric mass distributions
- *neutron star instabilities*: due to rapid changes of the inner structure
- *supernovae*
- *supermassive black holes*: $M > 10^5 M_\odot$
- *stochastic backgrounds*: due to density fluctuations in the early universe

1.2.4 Experimental evidence of gravitational waves

To date[1], gravitational waves have evaded attempts of direct detection. Strong, indirect evidence of their existence is provided from the timing of binary pulsar systems [4]. These systems lose energy under the form of gravitational radiation, and thus their radius and period become shorter. The orbit decay of a binary pulsar system was first observed in 1974 by Hulse and Taylor [5] on the change of pulsar timing of PSR B1913+16. The observation was in great agreement with the expected energy loss rate by gravitational radiation.

1.3 Gravitational wave interferometric detection

A worldwide effort is ongoing to detect gravitational waves. The most promising and sensitive detection technique is obtained with Michelson interferometers, which detect h as in 1.7, by measuring the change in distance between two test masses attached to the end mirrors (see chapter 2).

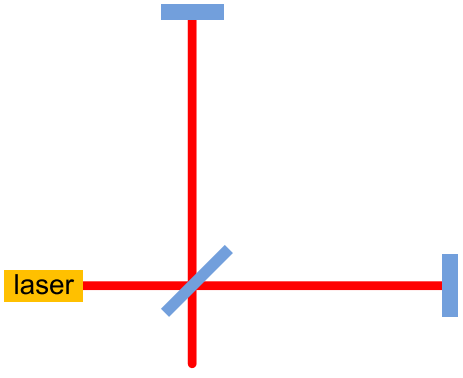

Figure 1.2: Gravitational wave laser interferometer. A laser beam explores the metric by measuring the different times taken by the light to travel and come back along each arm of the interferometer.

Detectors based on this technique are the two LIGO interferometers in the United States [6], Virgo, in Italy [7], GEO, in Germany [8], TAMA [9] and the forthcoming LCGT in Japan [10]. The LIGO detectors in particular have by now reached a sensitivity of 2×10^{-23} $/\sqrt{\text{Hz}}$ at 200 Hz (figure 1.3).

[1] Sunday 14 November, 2010.

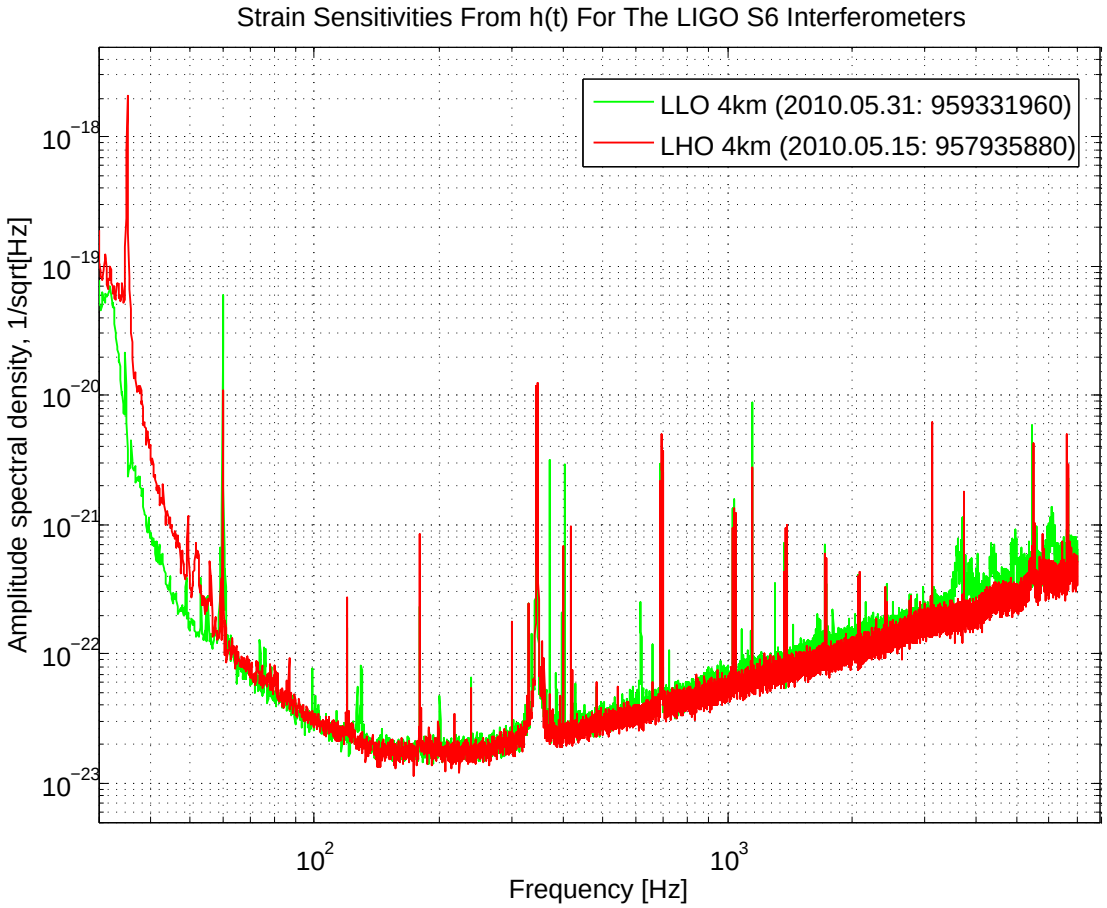

Figure 1.3: LIGO Interferometers strain sensitivity as of May 2010. LHO = Hanford, WA observatory; LLO = Livingston, LA observatory.

The construction of the second generation of gravitational wave interferometers started in 2010, immediately after the conclusion of the 6^{th} LIGO science run [11]. An overall improvement in sensitivity by a factor of 10 is expected, reaching the fundamental noise limits due to ground seismic motion [12], optics thermal noise [13] and laser shot noise [14] (figure 1.4).

Further improvement to the sensitivity, over a broader frequency range than the advanced interferometers, is expected by the 3^{rd} generation of ground detectors [15] and by the space antenna LISA [16].

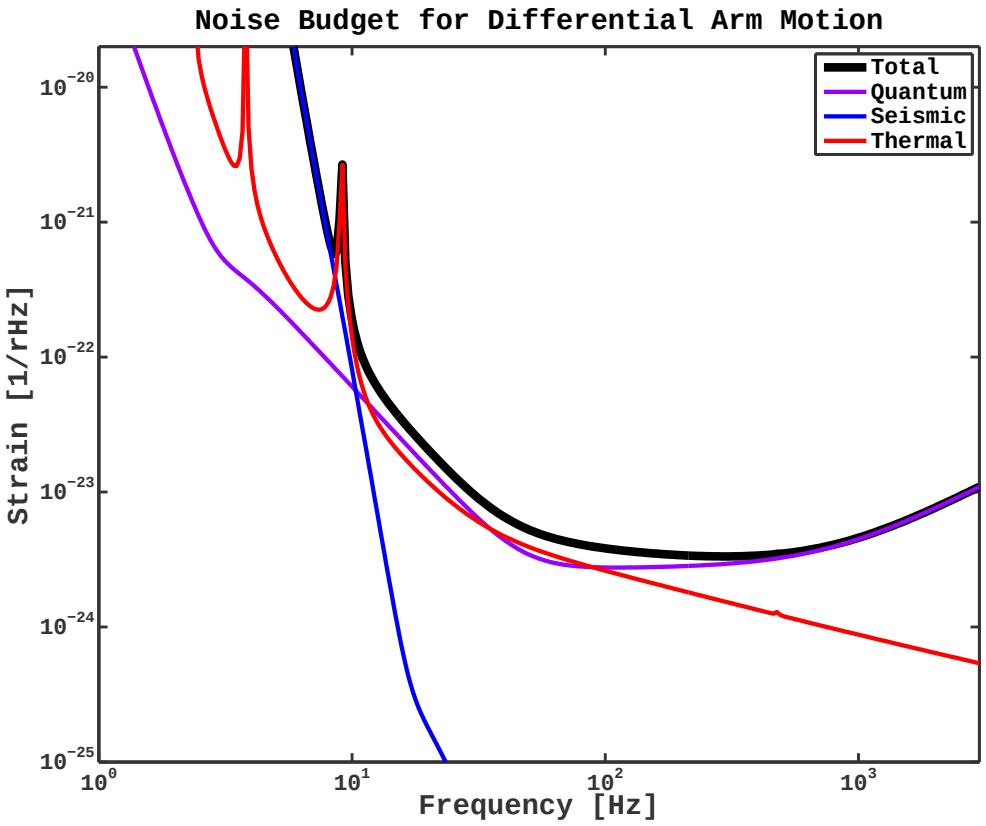

Figure 1.4: Advanced LIGO noise budget. Seismic noise dominates below 10 Hz, shot noise (quantum noise) dominates above 100 Hz. The neutron star-neutron star inspiral sensitivity range is 183 Mpc.

Chapter 2

Advanced Interferometric Gravitational Wave Detectors

In this chapter we introduce the fundamental parts of an advanced gravitational wave interferometric detector.

2.1 Measuring lengths with laser interferometry

The basis of laser interferometric techniques to measure distances is the comparison between the field of a laser beam directed at a target and the reflected field returning to the starting point. The relative phase between the two fields is proportional to the length of the optical path. If ω is the angular frequency of the laser, and L is the distance between the reference point and the target, the phase $\Delta\phi$ accumulated during the round-trip is

$$\Delta\phi = \frac{2\omega}{c} L. \tag{2.1}$$

By using the wavelength $\lambda = 2\pi c/\omega$ as a reference unit, the distance L can be separated into a *macroscopic* part $\Delta L = n\lambda$, with n an integer, and a *microscopic* residual $\delta l < \lambda/2$. The round-trip phase depends only on the microscopic length:

$$\delta\phi = \frac{2\omega}{c}\delta l \qquad \text{(modulo } \pi\text{)}. \tag{2.2}$$

2.1.1 Fabry-Perot cavities

The sensitivity of the phase measurement can be enhanced by using a Fabry-Perot optical cavity (figure 2.1). This cavity functions as an optical resonator for the input light: for frequencies of the laser such that an integer number of half-wavelengths is contained in the cavity length, the light interferes coherently with itself every time it bounces from the end mirrors. When this happens, the cavity resonates and the amplitude of the reflected field is amplified.

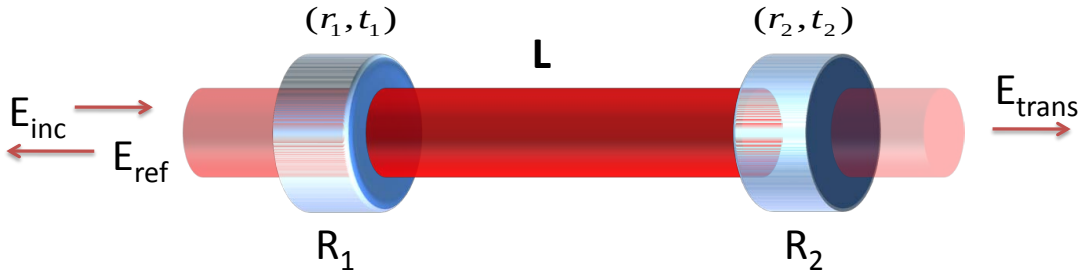

Figure 2.1: Fabry-Perot Cavity. E_{inc}, E_{ref} and E_{trans} are the incident, the reflected and the transmitted fields respectively; $r_{1/2}$ and $t_{1/2}$ are the reflectances and transmittances of mirrors 1 and 2.

Seen from the input laser, the cavity is equivalent to a mirror with reflectance r_{fp}

$$r_{fp} = -r_1 + \frac{t_1^2 g_{rt}}{r_1(1 - g_{rt})} \tag{2.3}$$

where r_1 and r_2, and t_1 and t_2 are the reflectances and the transmittances of the end mirrors, respectively, and g_{rt} is the cavity gain, defined as

$$g_{rt} = r_1 r_2 \exp\left(i\frac{2\omega}{c}L\right). \tag{2.4}$$

The resonant frequencies ω_{res} are those for which the optical phase accumulated one way along the cavity is π:

$$\omega_{res} = n \times \omega_{fsr} \tag{2.5}$$

$$FSR \equiv \frac{\omega_{fsr}}{2\pi} = \frac{c}{2L}. \tag{2.6}$$

with c the speed of light, n an integer number, and FSR is the cavity *Free Spectral Range* [17]. At frequency $\delta\omega$ away from resonance, the relative phase between the incident and the reflected field is

$$\delta\phi = \Im\left[r_{fp}(\omega_{res})\right] = \frac{r_2\left(1 - r_1^2\right)}{\left(1 - r_1 r_2\right)^2}\frac{2L}{c}\delta\omega. \tag{2.7}$$

Using the equivalence

$$\frac{\delta\omega}{\omega} = \frac{\delta L}{L} \tag{2.8}$$

the precision of the length measurement $\delta L/L$ for a phase $\delta\phi$ is

$$\frac{\delta L}{L} = \frac{\left(1 - r_1 r_2\right)^2}{r_2\left(1 - r_1^2\right)}\frac{\delta\phi}{2\pi} \tag{2.9}$$

in which

$$\frac{\left(1 - r_1 r_2\right)^2}{r_2\left(1 - r_1^2\right)} \propto \mathcal{F}^{-1} \tag{2.10}$$

and $\mathcal{F}$ is the *finesse* of the cavity, defined as

$$\frac{\pi\sqrt{g_{rt}}}{1-g_{rt}}. \tag{2.11}$$

Thus the precision of the length measurement is amplified by a factor proportional to the finesse of the cavity.

Gravitational wave interferometers increase their displacement sensitivity with kilometer-scale Fabry-Perot cavities with finesse of a few hundreds (i.e. $\mathcal{F} = 450$ in Advanced LIGO).

2.2 Gravitational Wave Sidebands

The electric field reflected by a moving mirror, oscillating at a frequency ω_a and amplitude A, in the approximation of $A \ll \lambda$, is

$$E_r = E_i \left(1 + \frac{\pi A}{\lambda} e^{i\omega_a t} - \frac{\pi A}{\lambda} e^{-i\omega_a t}\right). \tag{2.12}$$

The result is a *phase modulated field*, with sidebands at frequency ω_a on top of the carrier field. The magnitude of this sidebands is proportional to the amplitude of the mirror motion.

The strain h of the cavity lengths caused by gravitational waves induces the same effect on the field reflected by a mirror at distance L from the phase measurement point. Then the amplitude of the sidebands is $A = hL$. Ground based gravitational wave detectors aim at detecting waves in the frequency range between 10 Hz an 1 kHz.

The amplitude of the gravitational wave sidebands can be increased by considering longer optical paths L, and also by using optical cavities. A Fabry-Perot cavity can amplify sidebands within the width of its resonances. For a cavity of finesse $\mathcal{F}$ the resonance width ω_c is defined as the offset from the carrier frequency at which the circulating optical power in the cavity falls by 3 dB (or 1/2). The cavity bandwidth, finesse and free spectral range are related by:

$$\omega_c = \frac{\omega_{fsr}}{\mathcal{F}}. \tag{2.13}$$

In a simplified fashion, the effect of gravitational wave strain on a Fabry-Perot cavity can be represented as if the input mirror were fixed and the end mirror moved with the amplitude and the frequency of the strain. It is possible to define the dynamical response of the cavity as the transfer function between the end mirror displacement and the amplitude of the circulating sideband. The cavity behaves as a low pass filter, and its transfer function has a pole at ω_c.

2.3 Michelson Interferometer

Analogous to the gravitational wave sidebands, frequency and intensity fluctuations of the laser introduce phase modulation sidebands around the main carrier frequency. These are

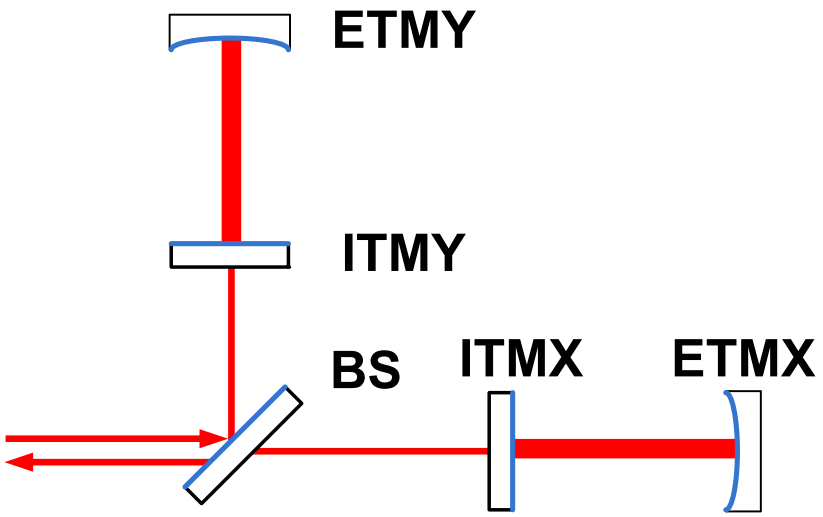

Figure 2.2: Fabry-Perot Michelson. ITM = Intermediate Test Mass; ETM = End Test Mass.

totally indistinguishable from mirror displacement and as such, they limit the sensitivity of the length measurement.

By using a Michelson interferometer it is possible to distinguish laser frequency noise from the gravitational signal. Because of the differential effect of gravitational waves on two orthogonal directions of space, the signal sidebands from the two arms of a Michelson interferometer have opposite phases, whereas laser noise sidebands appear with the same phase. When the fields returning from the two arms recombine at the beam splitter, laser noise cancels and gravitational wave sidebands survive (figure 2.3).

The integration of Fabry-Perot cavities into a Michelson interferometer further increases the signal-to-noise ratio of the detector (figure 2.2).

In a real system, this noise cancellation effect at the dark port of the interferometer is not perfect. Asymmetries between the reflectances of the two arms partly spoil the field recombination (more on this in chapter 5).

2.4 Phase measurement

The gravitational wave sidebands of 2.12 have frequency $f = (\omega_0 + \omega_a)/2\pi \sim 10^{14}$ Hz, which is beyond the bandwidth of any existing photodetector. It is thus necessary to down-convert the signal to accessible frequencies. Either heterodyne or homodyne detection may serve this function. When applied to gravitational wave interferometers, these schemes are called *RF readout* or *DC readout*, respectively.

2.4.1 Optical heterodyne detection

Optical heterodyne detection is analogous to its counterpart used in RF electronics. A reference laser field at frequency Ω is used as a local oscillator to down-convert the gravitational wave sidebands to a frequency $\omega' = \omega_0 \pm \omega_a - \Omega$. The local oscillator field E_{LO}

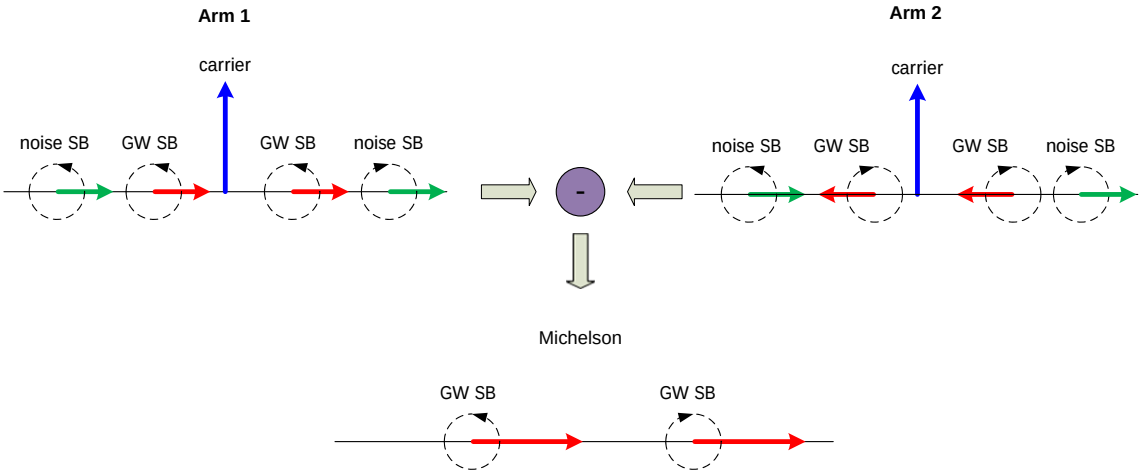

Figure 2.3: Signal and noise sidebands. Gravitational wave sidebands have opposite phases in the arms and survive subtraction. Common mode noise sidebands cancel.

and the signal sideband field E_{sig} interfere at a photodiode. The power P of the resulting field contains a DC components, due to the amplitude of the individual fields, and a beat note at a frequency ω':

$$\begin{aligned} P &= \left| E_{LO} e^{i\Omega t} + E_{sig} e^{i(\omega_0+\omega_a)t} - E_{sig} e^{i(\omega_0-\omega_a)t} \right|^2 \\ &\approx P_{DC} + 2E_{LO}E_{sig} \sin(\omega_0 + \omega_a - \Omega) + 2E_{LO}E_{sig} \sin(\omega_0 - \omega_a - \Omega) . \end{aligned} \tag{2.14}$$

In heterodyne detection the local oscillator is provided by a pair of RF modulation sidebands imprinted on the input laser beam before it enters the interferometer. These are set such that they do not circulate in the arm cavities and thus their phases remain a stable reference despite movements of the cavity's mirrors (more about the RF sidebands frequency in chapter 4).

The sidebands are generated by phase modulation of the laser beam. An electro-optical device (i.e. an EOM), driven by a modulation signal $V_m(t) = V_0 \cos(\omega_m t)$ modulates the phase of the field by changing the refraction index of an optical medium where the laser goes through. The effect on the electric field is the introduction of sidebands around the main laser frequency ω_0:

$$E_{in} = E_0 e^{(i\omega_0 t + \gamma \cos \omega_m t)} = E_0 e^{i\omega_0 t} \sum_{n=-\inf}^{n=\inf} i^{|n|} J_{|n|}(\gamma) e^{i\gamma\omega_m t} \tag{2.15}$$

where J_n is the n-th order Bessel function and γ the modulation depth. In the case of advanced interferometers, the RF modulation has typically a frequency $f_m = \omega_m/2\pi \sim$ 10 MHz (figure 2.4).

When the differential length of the Michelson interferometer is an integer multiple of $\lambda/2$, the carrier fields at frequency ω_0 interfere constructively at one port and destructively at the other. However the local oscillator sidebands can be transmitted to the dark port,

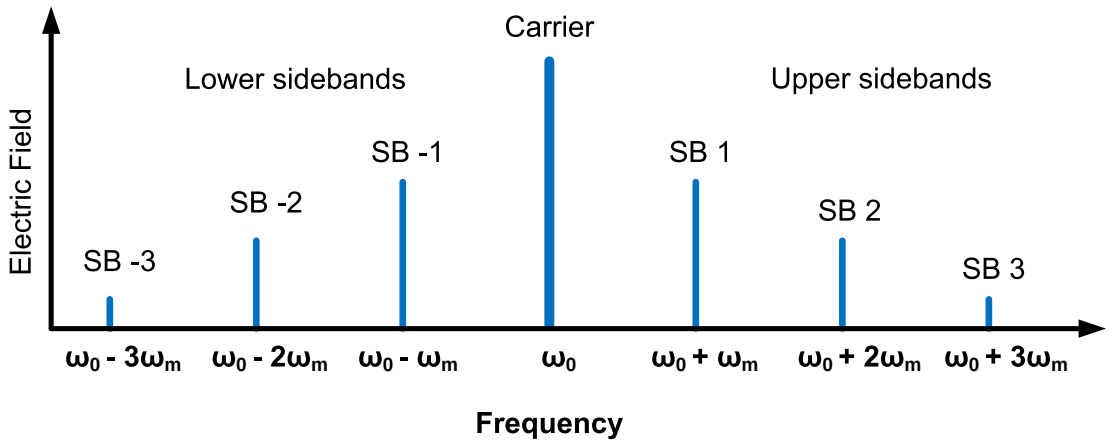

Figure 2.4: Sidebands appear on the sides of the laser carrier frequencies at distances multiple of the modulation frequency ω_m, and with amplitude dependent on the amplitude of the modulation.

if the Michelson arms have different macroscopic lengths. This length difference is called Schnupp asymmetry [18] (see Appendix A).

The resulting beat note on the photodiode signal is then mixed with the same oscillation used for generating the RF sidebands. The gravitational wave signal $E_{sig}\sin(\omega_a)$ is contained in the demodulated signal.

2.4.2 Optical homodyne detection

In homodyne detection the local oscillator is provided by the carrier itself: $\Omega = \omega_0$. This carrier light is obtained by introducing a microscopic offset between the two Michelson arms and letting some of the light leak to the dark port. There it beats with the gravitational wave sidebands, producing a signal proportional to $E_{sig}\sin(\omega_a)$ (figure 2.5).

2.5 Enhancing the SNR

The electric fields circulating in the interferometer are subjected to shot noise, or, in a more general sense, amplitude and phase quantum fluctuations [19]. Power fluctuations of a field of power P due to shot noise have amplitude

$$\delta P_{shot} = \sqrt{\frac{2hc}{\lambda}P}. \tag{2.16}$$

2.5.1 Coupled cavities

One way to improve the shot noise SNR is to increase the laser power. However this would also increase the frequency and amplitude noise of the laser, thus affecting the overall SNR. The solution adopted by gravitational wave interferometers is the coupling of an additional optical cavity to the bright port of the Michelson [20]. This technique is

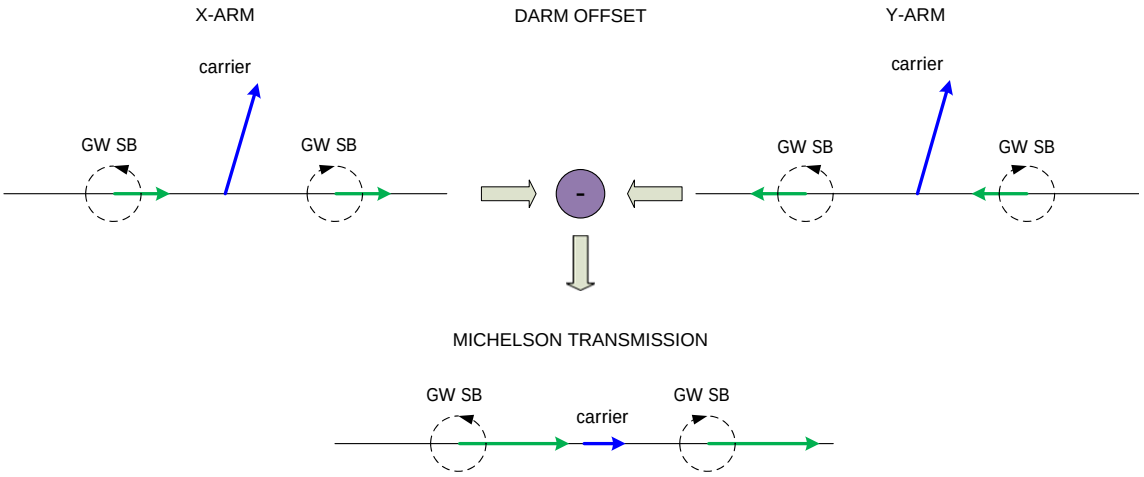

Figure 2.5: Phasor diagram of heterodyne detection. A static length offset is induced between the two arm cavities. Some light leaks through the dark port, effectively rotating the carrier's phase. Its projection onto the phase quadrature enables it to beat with the gravitational wave acoustic sidebands.

called *power recycling* (figure 2.6) and the mirror which forms the coupling cavity is called the *power recycling mirror*, or PRM.

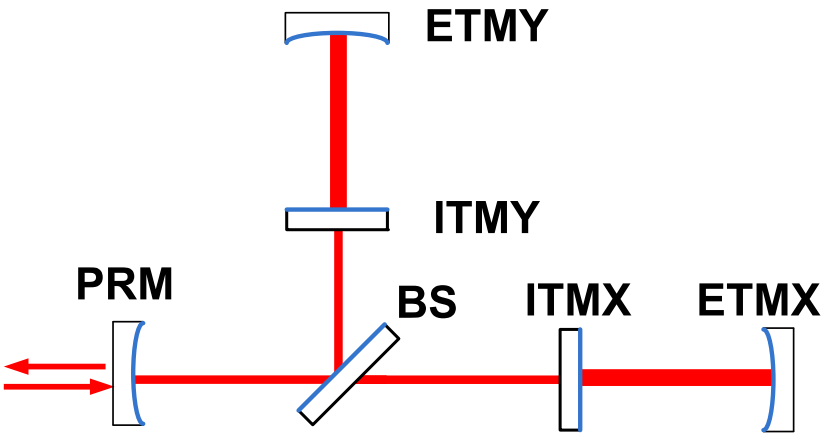

Figure 2.6: Power Recycled Fabry-Perot Michelson.

Since the Michelson combines the two arm cavities, for the light that exits the bright side of the beam splitter, the interferometer is equivalent to a single Fabry-Perot cavity of length equal to that of the arm cavity. Its end mirror is identical to that of the arm cavities, and its input mirror is a *compound* mirror with the reflectivity of the Michelson [18]. Adding a mirror in front of the bright port is equivalent to juxtaposing an optical cavity of length

$$l_{prc} = l_{prm-bs} + \frac{l_x + l_y}{2}, \tag{2.17}$$

where l_{prm-bs} the distance between the PRM and the beam splitter (BS), and $l_{x/y}$ are the distances between BS and the two ITMs, respectively (figure 2.7). This cavity is called the *power recycling cavity* (PRC).

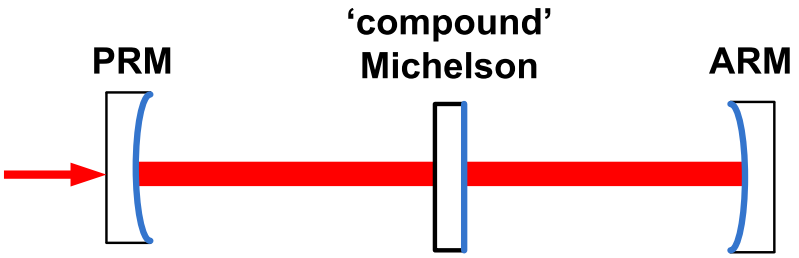

Figure 2.7: Coupled cavity.

The PRM reflects back into the interferometer most of the light that exits the bright port of the Michelson, effectively increasing the circulating power. Depending on the amount of phase accumulated by the laser field in a round trip in the power recycling cavity, this light may be only passively reflected back into the interferometer. But, if the round trip phase is zero (modulo π), the light can also resonate in PRC and thus be subjected to additional filtering by the power recycling cavity.

Some confusion may arise when defining this resonant condition for the light in the power recycling cavity. In fact, for the carrier light to resonate, the cavity must be *anti-resonant*. The reason for that, as explained in detail in Appendix A, is that as soon as the carrier becomes resonant in the arm cavity, it sees the ITM's reflectances flipping sign. Then the cavity gain (equation 2.4) also changes sign, and the resonant conditions on the PRC length are reversed.

The resulting coupled cavity responds with an effective cavity pole which, following [21, 22], can be written as

$$\omega_{cc} = \frac{1 + r_{prm} r_{arm}(\omega_{res})}{1 + r_{arm}} \omega_c \tag{2.18}$$

where r_{prm} is the reflectance of the PRM, ω_c is the arm cavity pole (equation 2.13), and r_0 is the reflectance of the arm cavity at resonance:

$$r_0 \equiv r_{arm}(\omega_{res}) \approx \frac{r_{etm} - r_{itm}}{1 - r_{etm} r_{itm}}. \tag{2.19}$$

Then the coupled cavity has gain

$$g_{prc} = \frac{t_{prm}}{1 + r_{prm} r_{arm}} \tag{2.20}$$

Using Laplace notation, and normalizing the gravitational wave audio sideband frequency ω_a, we define the quantities

$$s_{cc} = i\frac{\omega_a}{\omega_{cc}} \tag{2.21}$$

$$s_c = i\frac{\omega_a}{\omega_c}, \tag{2.22}$$

then the arm cavity reflectance at frequencies near resonance can be approximated as

$$r_{arm} \approx r_0 \frac{1 + s_c/r_0}{1 + s_c} \tag{2.23}$$

and the amplitude of the field circulating in the coupled cavity is

$$E_{prc}^{(cc)} = E_{in} g_{prc} \frac{1 + s_c}{1 + s_{cc}}. \tag{2.24}$$

For an anti-resonant PRC, the response 2.24 has a pole at the coupled cavity pole ω_{cc}, and a zero at the arm cavity pole ω_c. Also since $s_{cc} < s_c$, the low-pass filter cut-off is at a lower frequency than the arm-cavity alone.

The power recycling cavity thus increases the circulating power and performs additional filtering to laser frequency and amplitude noise.

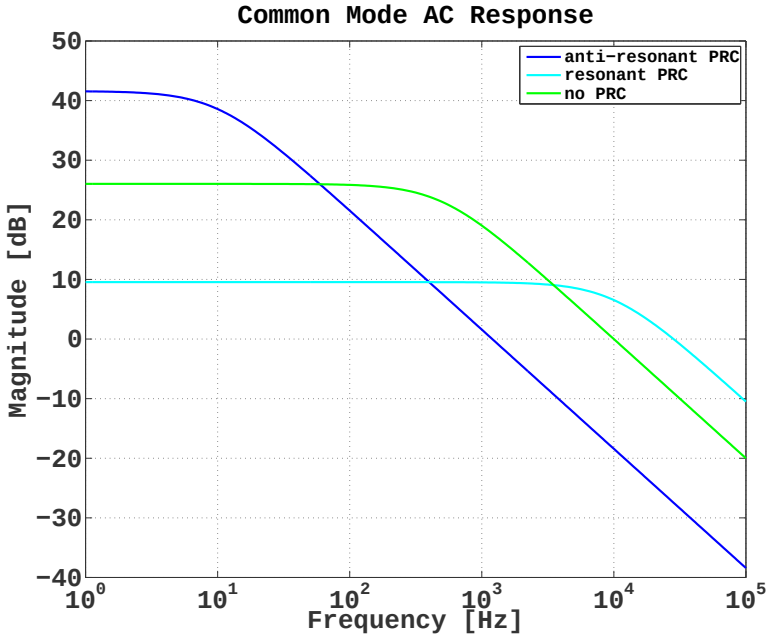

Figure 2.8: Power recycling cavity gain (i.e. circulating power divided by input power).

2.5.2 Interferometer common and differential mode

The Michelson has 2 longitudinal degrees of freedom: common mode and differential mode. The first results from the average length change of the arm cavities, and it is usually represented with

$$L_+ = \frac{L_x + L_y}{2}, \tag{2.25}$$

the second arises from the relative length change of the arms, and is usually indicated with

$$L_- = L_x - L_y. \tag{2.26}$$

When the interferometer is locked, the output ports decouple these degrees of freedom: the fields at the bright port respond to the common mode, and the fields at the dark port the differential mode. Because of this, the common mode laser noise is directed to the bright port, and the gravitational wave sidebands, originated by the differential arm motion, are deviated to the dark port.

As a recycling cavity can be coupled to the common mode of the interferometer, an extra cavity can also be coupled to the differential mode by adding a mirror to the dark side of the beam splitter. This forms the so-called *signal recycling cavity* (SRC) is formed in this way [23] (figure 2.9). The mirror used to reflect the signal back into the interferometer is called the *signal recycling mirror* (SRM).

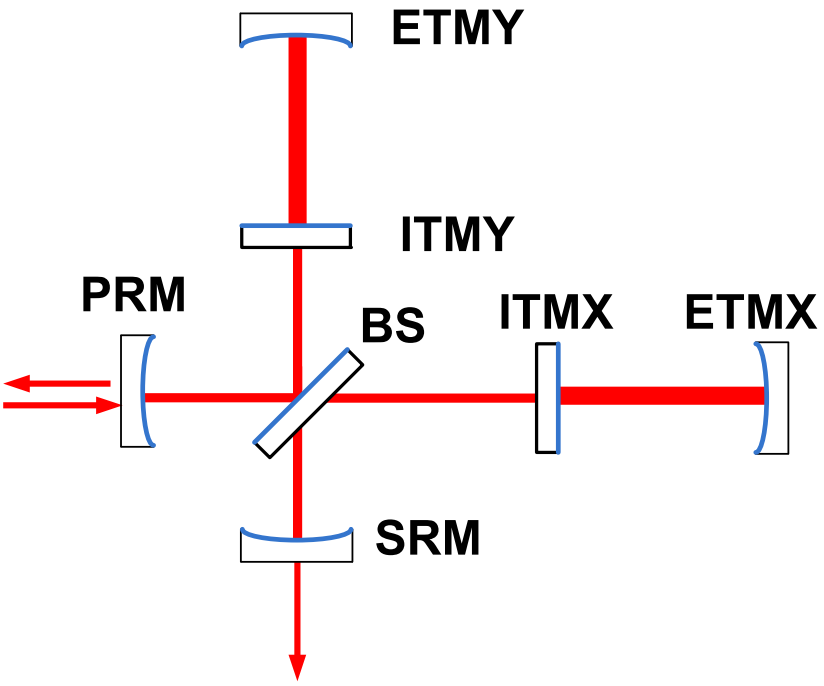

Figure 2.9: Signal Recycling Cavity.

The purpose of the signal recycling cavity is to amplify the gravitational wave sidebands. Low pass filtering is not desired in this case, since it would reduce the bandwidth of the interferometer for gravitational waves. Thus, in an opposite fashion to the power recycling cavity, the signal recycling cavity is set to be *resonant*. In this way, when this cavity is coupled to the resonant arms, the gravitational wave signal does not resonate.

The coupled cavity response 2.24 to the gravitational wave sidebands originated in the arms is

$$E_{src}^{(cc)} = E_{in} g_{src} \frac{1 + s_{prc}}{1 + s_{cc}} \tag{2.27}$$

where s_{prc} is the pole of the signal recycling cavity *alone*.

2.6 Interferometer Control

As explained in the previous section, the state of the interferometer is determined by the microscopic lengths of the cavities. In the real system, several disturbances act on the mirrors, moving them at the micron level. To keep the microscopic length from changing, it is necessary to control the mirrors.

The Pound-Drever-Hall technique serves this function [24] by measuring the phase of the light reflected by a cavity. This technique uses RF modulation sidebands imprinted on the input laser as a local oscillator. These sidebands must have a modulation frequency such that they do not circulate in the cavity. This ensures that their phase provides a stable reference even if the cavity moves. The carrier light circulates in the cavity and then is reflected. When the interference between the RF sidebands and this carrier is measured by a photodiode, it produces a beat note at the RF modulation frequency. The signal obtained by demodulating this beat note carries information about the phase gained by the carrier, relative to the phase of the RF sidebands. The demodulation signal can then be used as an error signal for the cavity length. Applied to an actuator on one of the end mirror, this signal can keep the microscopic length to zero (figure 2.10).

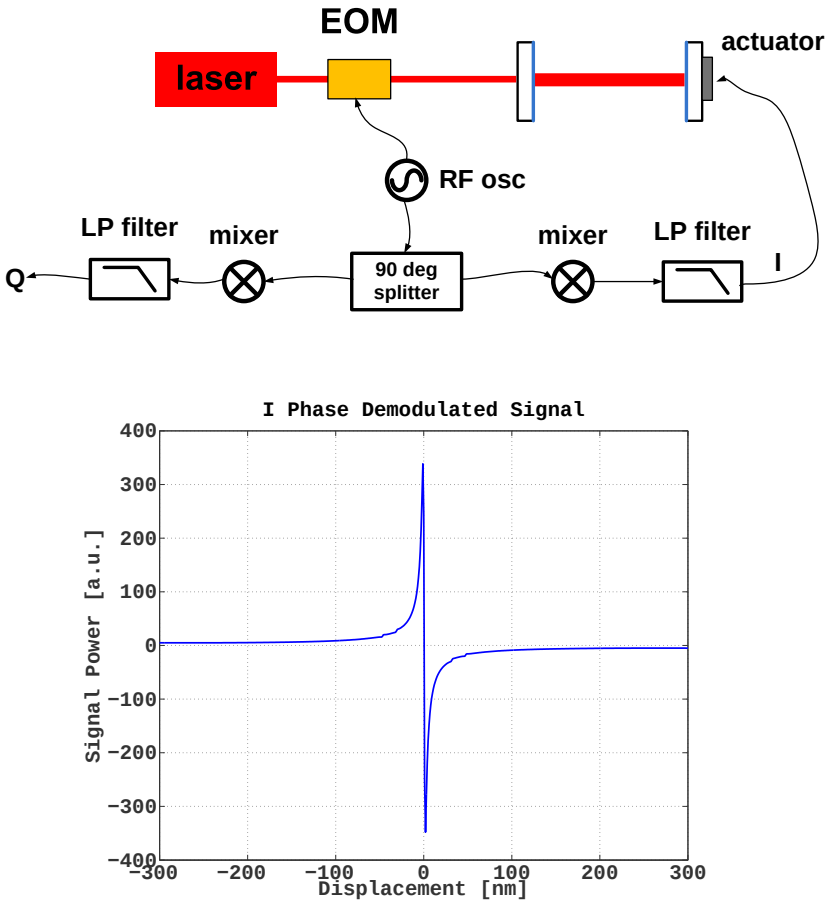

Figure 2.10: Pound-Drever-Hall Technique. Top: cavity setup; Bottom: error signal obtained from the I-phase of the signal demodulation.

Applying this technique to all the cavities of the interferometer, it is possible to ensure the locking conditions on any degree of freedom. Complications arising from cavity cross-talk when all cavities have to be locked simultaneously will be discussed in chapter 4.

Chapter 3

The Caltech 40m Advanced Gravitational Wave Interferometer Prototype

The 40m laboratory at the California Institute of Technology[1] hosts an advanced LIGO gravitational wave interferometer prototype, with 40 m long arms, scaled 1:100 to the observatories. This facility provided the testbed for the work discussed in this thesis. In this chapter we give a brief description of the main features of the lab.

3.1 Scientific Scope

The 40m interferometer is a LIGO facility whose main mission is to serve as a test bench for the Advanced LIGO gravitational wave interferometers. Active since the 1980's, after 2000 it has served as a prototype for the development of length sensing and control techniques of a Dual-Recycled Fabry-Perot Michelson interferometer (DRFPMI) [25, 21]. In 2007 the optical design of Advanced LIGO was finalized, with several changes from the 2001 configuration [26]. As a consequence, starting in 2009 the 40m has been upgraded to the new Advanced LIGO design [27].

The 40m is not a noise prototype: the high environmental noise that characterizes its location[2], and the absence of high attenuation seismic isolation systems, make it unsuitable for high arm displacement sensitivity. However it provides an ideal facility for the development and testing of subsystems and advanced experimental techniques.

[1] 1200 E California Blvd., Pasadena, 91125 CA, USA.
[2] The Caltech campus is located in the greater Los Angeles metropolitan area.

Figure 3.1: 40m view from the beam splitter corner station

3.2 Interferometer description

Main laser

The 40m main laser is a 1064 nm Nd:YAG NPRO with a 2 W power (Innolight Mephisto). Before entering the interferometer the NPRO beam is filtered by a Pre-Mode Cleaner (PMC) monolithic cavity: the laser is locked to this cavity by the Pound-Drever-Hall technique. After this stage, the laser is frequency stabilized by a dedicated servo (FSS) which locks it to a reference cavity. An additional Intensity Stabilization Servo (ISS) controls the power of the output beam.

After these stabilization stages, the resulting beam, referred as *PSL* (Pre-Stabilized Laser), passes through an Electro-Optical Modulator (EOM) which adds the modulation sidebands used to control the interferometer's degrees of freedom and to extract the gravitational wave signal at the dark port (cfr. section 2). Finally the beam is injected into the input mode cleaner. When the interferometer is locked, an additional frequency stabilization servo is engaged by locking the laser to the mode cleaner, and this, in turn, to the arm common mode. The details of this common mode freqeuncy stabilization servo can be found in [21].

Main optical cavities

The 40m interferometer is a signal recycled and power recycled interferometer. The power recycling mirror is preceded by an Input Mode Cleaner (IMC), a triangular cavity used for filtering the space profile of the input beam, and to stabilize its axis and angle before entering the interferometer. Also, and most important, the mode cleaner serves as a reference cavity to stabilize the frequency of the laser. Similarly, the signal recycling mirror is followed by an Output Mode Cleaner (OMC) cavity used to filter the transmitted beam from laser higher spatial modes and additional unwanted sidebands [21]. Figure 3.2 shows the optical layout of the interferometer. The recycling cavities are folded using folding mirrors (PR2-PR3, SR2-SR3). A more detailed description of the features of the optical cavities is presented in chapter 4 of this thesis.

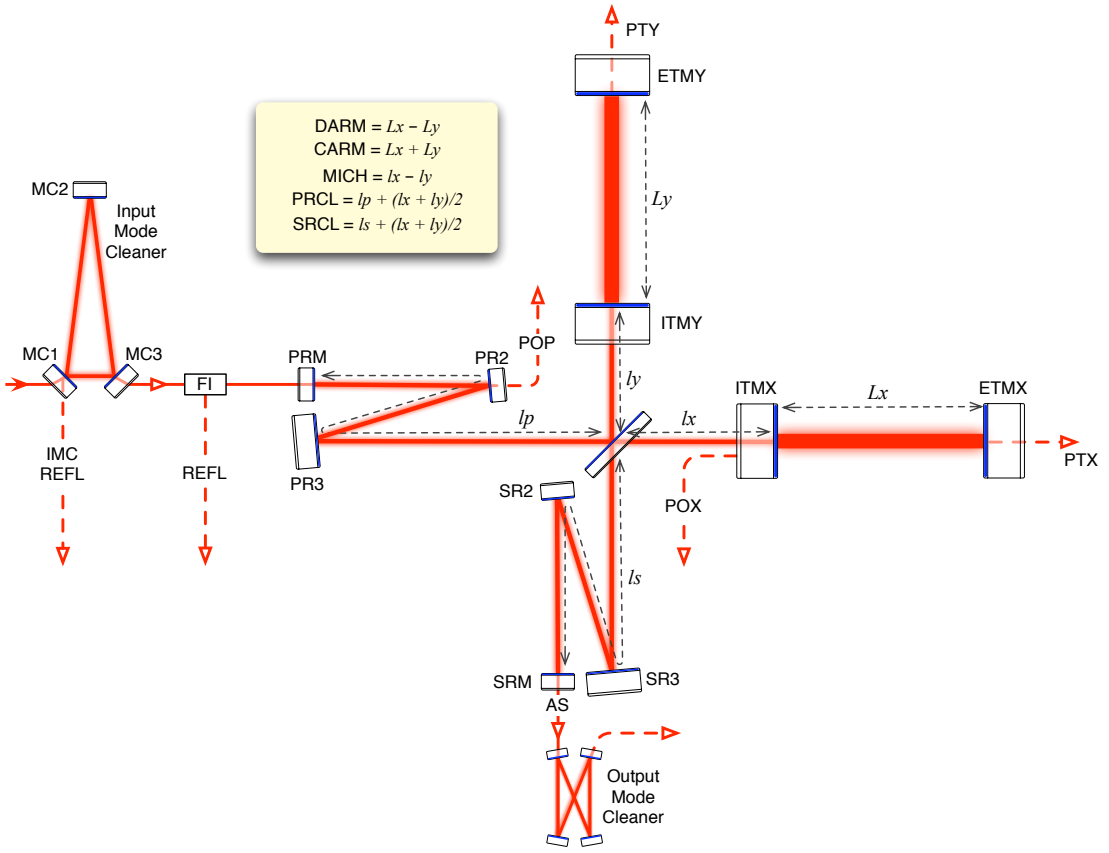

Figure 3.2: 40m optical configuration (from [26]).

Optics

The 40m optics parameters are summarized in figure 3.3. The main optics (ETM's, ITM's, PRM, SRM) are made of Corning 7980 Fused Silica. Their size and weight are: 3" (76 mm) diameter; 2" (50 mm) thickness; and 250 g. Figure 3.4(a) shows one of the main mirrors. Four magnets, attached to the back surface of each mirrors, are used to actively drive the optics by means of coil actuators. Collocated within the actuators are also shadow detectors (OSEM, [29]) used as position sensors of the mirrors (figure 3.4(b)).

Suspensions

The main optics are suspended by piano wires with a 40 μm diameter to single pendulum SOS seismic isolation towers [30] (figure 3.5(a)). The folding mirrors are suspended by tip-tilt passive isolation towers [31] (figure 3.5(b)). The optics tables with the main optics are supported by stack springs passive isolation systems [32].

Vacuum

The entire interferometer is maintained under vacuum at a pressure of about 10^{-6} Torr ($= 10^{-9}$ atm).

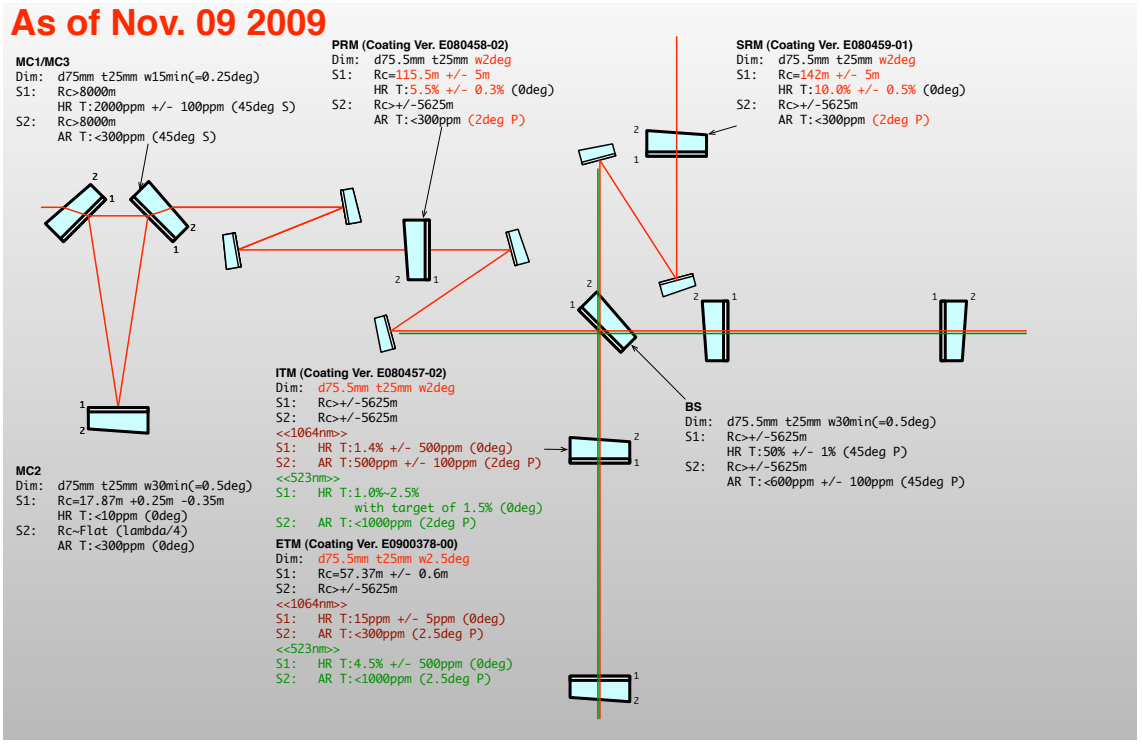

Figure 3.3: 40m optics properties [28].

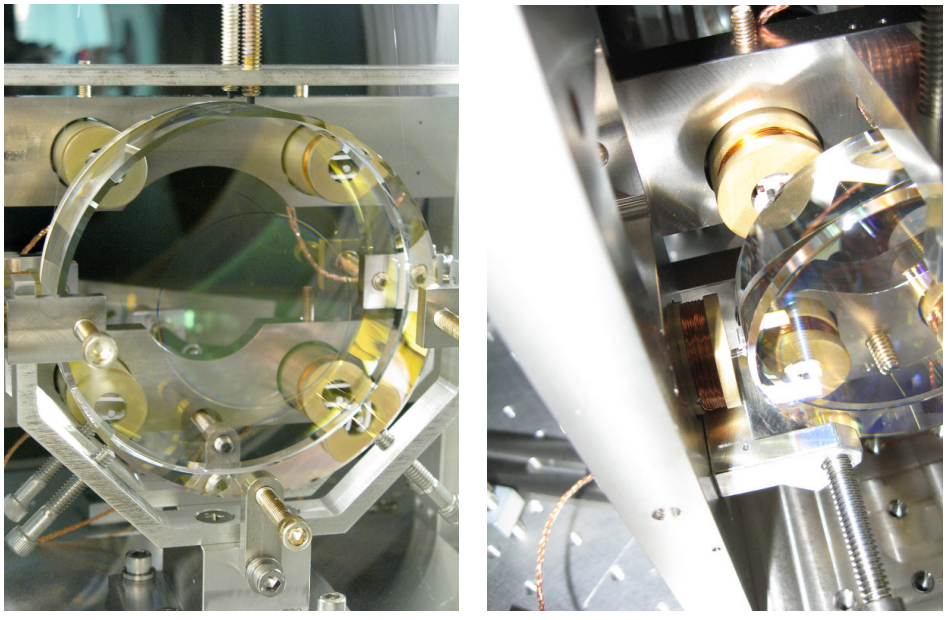

(a) (b)

Figure 3.4: (a) Test mass mirror; (b) Sensor/actuator OSEM used to measure the position of the mirror and as an actuator.

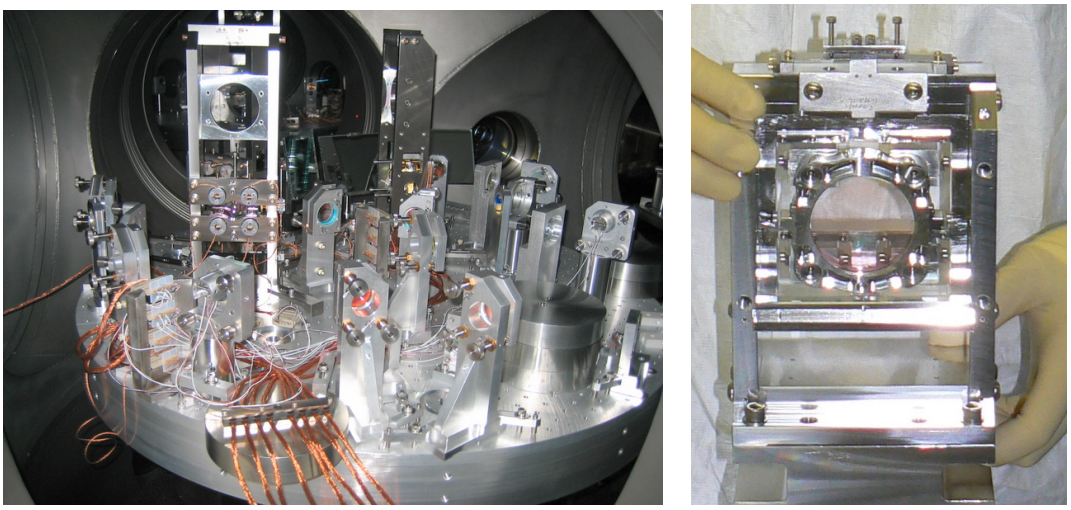

(a) (b)

Figure 3.5: (a) View of the beam splitter chamber showing two of the suspension towers used for the main optics; (b) Tip-tilt suspension system used for the folding mirrors.

Control and data acquisition system

The control and data acquisition system performs the digitization of the signals from the sensors and uses these to generate the appropriate driving signal to actively control the interferometer. Analog-to-digital and digital-to-analog converters (ADC and DAC) are used for the Input/Output process from sensors to actuators. A single dedicated CPU controls in real time the data flow for each mirror, combining local and global control signals (figure 3.6).

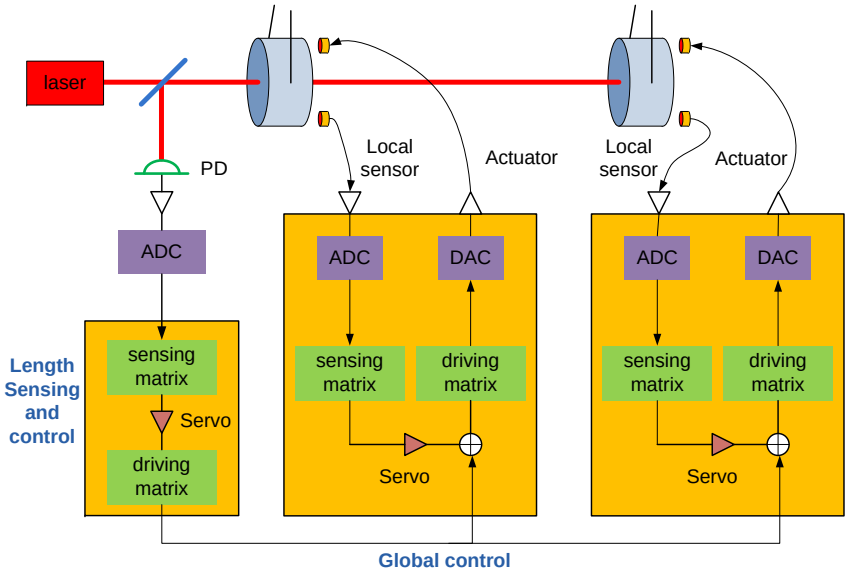

Figure 3.6: Local and global control and data acquisition system for one degree of freedom.

3.3 Length sensing and control system

The length sensing and control system (LSC) is used to determine the state of each cavity and to control the degrees of freedom until the resonant conditions are satisfied and the interferometer is at its working point.

RF modulation/demodulation system

The RF modulation sidebands are added to the main beam before it enters the interferometer. Three modulations, at $f_1 = 11$MHz, $f_2 = 55$MHz and $f_{mc} = 29.5$MHz, respectively are applied to a triple-resonant electro-optical modulator [33]. The same modulation signals are then used downstream to demodulate the photodiode outputs at the ports of the interferometer.

The design and the construction of the 40m RF system was part of this thesis. The details are discussed in Appendix B.

Degrees of freedom

There are 7 main optics in the Dual Recycled Fabry-Perot Interferometer: BS, ETMX/Y, ITMX/Y, PRM, SRM. If we consider only the longitudinal degrees of freedom (DOF), 7 coordinates are necessary to describe the whole system. However, since the electromagnetic field in the interferometer is unaffected by scale space transformations (i.e. a uniform expansions centered on the BS, [34]) or to rigid translations on the XY plane, the number of generalized coordinates is just 5. As listed in figure 3.2, these are:

- *CARM*: common arm length
- *DARM*: differential arm length
- *PRCL*: power recycling cavity length
- *MICH*: Michelson differential length
- *SRCL*: signal recycling cavity length

The degrees of freedom of the interferometers are optically sensed by Pound-Drever-Hall signals from the cavities (details in chapter 4).

Photodetectors

The main ports of the interferometer where the signal is measured are:

- *REFL*: located at the reflection output of the Faraday isolator installed before the power recycling mirror and after the input mode cleaner, it represents the bright/symmetric port of the interferometer;
- *AS*: located after the output mode cleaner, it represents the dark port of the interferometer;

- *POP1*: measures the field circulating in the power recycling cavity by a pick-off beam from one of the folding mirrors in that cavity;
- *POX/Y*: measures the field in the X/Y arm cavity by a pick-off beam obtained from the ITM;
- *PTX/Y*: also called TRX/Y, measures the arm cavity transmitted power from the weak transmission through the ETM;
- *REFL MC*: measures the mode cleaner reflected beam (used to lock the cavity);
- *MCT*: measures the mode cleaner transmission through the MC2 mirror.

The signals obtained from each port are listed in table 3.1.

Port	**Signal**	**Freq. [MHz]**
REFL	REFL I/Q1	11
	REFL I/Q2	55
	REFL 3I/Q1	33
	REFL 3I/Q2	166
	REFL DC	-
AS	AS I/Q2	55
	AS DC	-
POP1	POP1 I/Q1	11
	POP1 I/Q2	55
	SPOB 1	22
	SPOB 2	110
POX	POX I/Q1	11
POY	POY I/Q1	11

Table 3.1: Signals measured at each port, with the correspondent demod signal.

Additionally, at REFL MC, MCT and PTX/Y DC Quadrant Photo-Detectors (QPD) measure the angles of incidence of the beam. RF QPD's are also used as wave-front sensors to measure the mode cleaner angular degrees of freedom [35].

3.4 Noise budget

The sensitivity of the 40m interferometer is expected to be limited by seismic noise below about 100 Hz. A noise budget for the main noise contributions is shown in figure 3.7

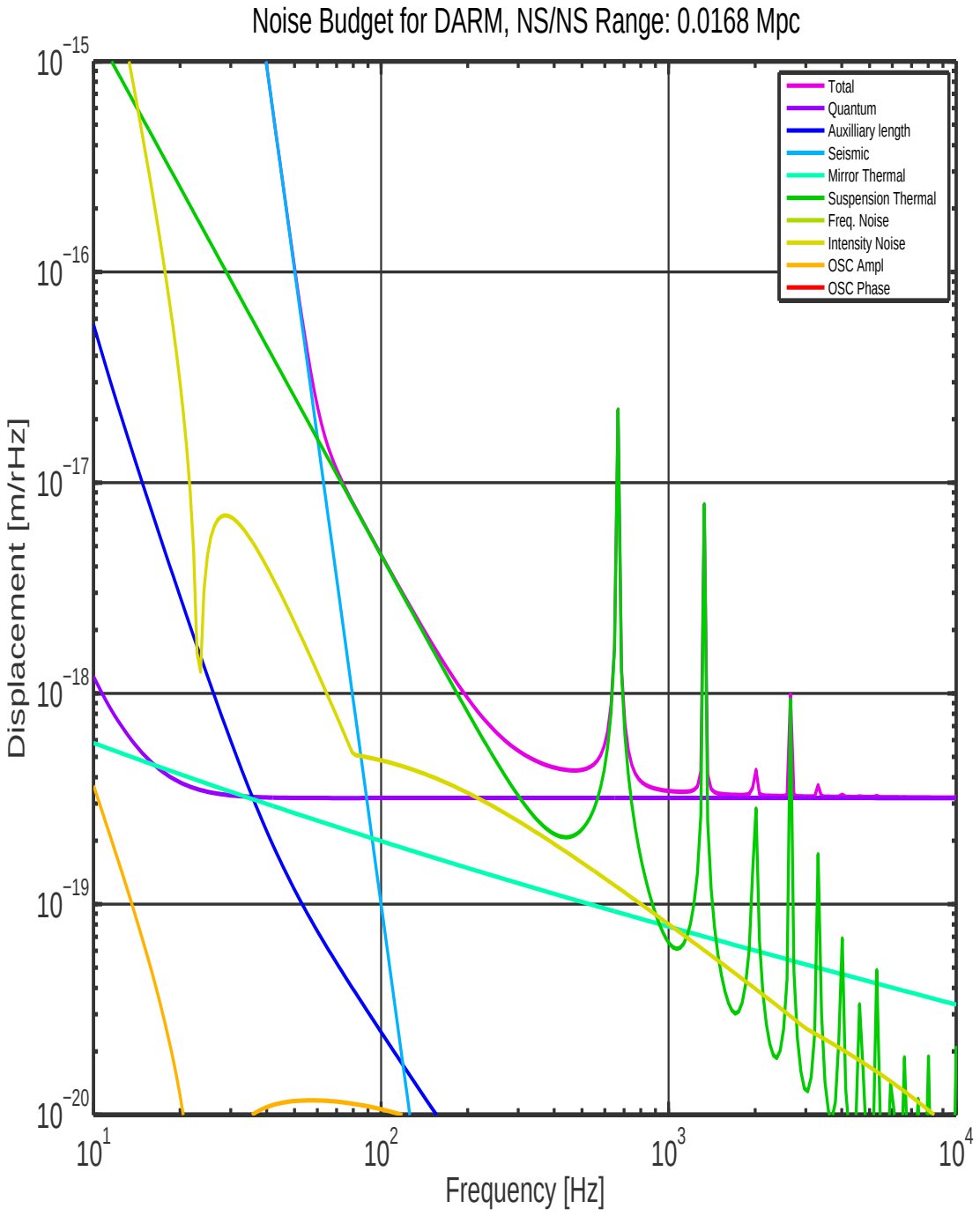

Figure 3.7: 40m Upgrade noise budget estimated with the Gravitational Wave Interferometer Noise Calculator software (GWINC).

Chapter 4

Optical Design

The 2010 upgrade of the Caltech 40m prototype conforms the interferometer to the final Advanced LIGO length sensing and control design [26]. Major upgrades in the modulation system, arm cavity finesse, and interferometer locking demand appropriate modifications to the optical configuration. This chapter describes the implementation of the Advanced LIGO design into the 40m Upgrade [27].

4.1 Cavity Lengths

One of the main changes in the 40m Upgrade from the previous system configuration, is the adoption of lower modulation frequencies. This has consequences on the optical layout of the interferometer, since longer recycling cavities are needed to accommodate lower frequency sidebands. In this section we discuss the design of the 40m cavity lengths according to the Resonant Sideband Extraction scheme (RSE) adopted by Advanced LIGO [36]. In particular, we present how some of the ideal RSE design parameters presented in Appendix A are adapted to fit the specific constraints imposed by the lab facility.

4.1.1 Length Offsets

The first constraint derives from the Mode Cleaner length. Any sideband must resonate in it before entering the interferometer. The 40m mode cleaner has a fixed length of about 13.564 meters, corresponding to a free spectral range of $f_{FSR} = 11.065399$ MHz. Because this differs from Advanced LIGO modulation frequencies (9 and 45 MHz), either the cavity length or modulation frequency of the 40m must be modified. The first option is not possible without major modifications to the lab structure. Thus the mode cleaner is kept as it is and its free spectral range is adopted for the modulations (see table 4.1).

Arms

The actual length of the 40m arm is different from the value required by the ideal design (see Appendix A for a definition). Much of the optical design is then dedicated to address this problem.

Modulation	Frequency [MHz]
$\mathbf{f_1}$	11.065399
$\mathbf{f_2}$	55.326995

Table 4.1: 40m Upgrade modulation frequencies. The values are different from those adopted in Advanced LIGO (9 and 45 MHz) because of a physical constraint imposed by the length of the existing mode cleaner cavity.

As a consequence of the mismatched length, the sidebands are no longer anti-resonant in the arm cavities and they accumulate some non-negligible phase upon reflection by the ITMs. In particular, the cavity is about 38 m long and is near the resonance of the f2 sideband located at $L_{arm} = 37.93$ m. To distance the cavity from resonance, its length is set at 38.4 m, at the limit edge of the optics table. At this length both sidebands gain only about 0.7° of phase after reflection from the ITMs (see figure 4.1).

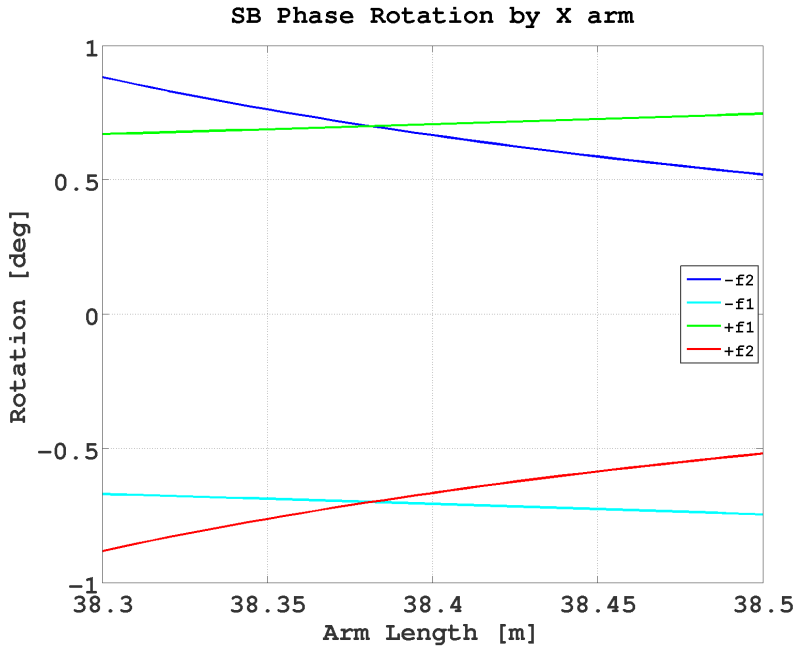

Figure 4.1: This numerical simulation of the 40m interferometer reveals a phase rotation experienced by the sidebands upon reflection from the ITMs because of the non ideal length of the arm cavities.

Recycling Cavities and Schnupp Asymmetry

Because the sidebands return from the arms with an additional phase, some modifications to the lengths of the recycling cavities and to the Schnupp asymmetry are necessary to compensate for it. The phase accumulated by the sideband fields from a round trip in the central part of the interferometer depends on the length of the recycling cavity and also on the length of the arms. This has several consequences on the fields at the sensing ports of the interferometer:

- f_1 or f_2, are no longer resonant
- the symmetry of their powers in the Michelson arms is disrupted (figure 4.2).
- the Schnupp asymmetry for the critical coupling condition of the f2 sideband going from PRC to SRC has to be calculated in the general case where the reflectance of the ITMs $r_{itm}(f_2)$ is not a purely real number:

$$L_{prc} = \frac{c}{2\pi f_2} \cos^{-1}\left(\frac{-r_{prm}}{\Re[r_{arm}(f_2)]}\right). \tag{4.1}$$

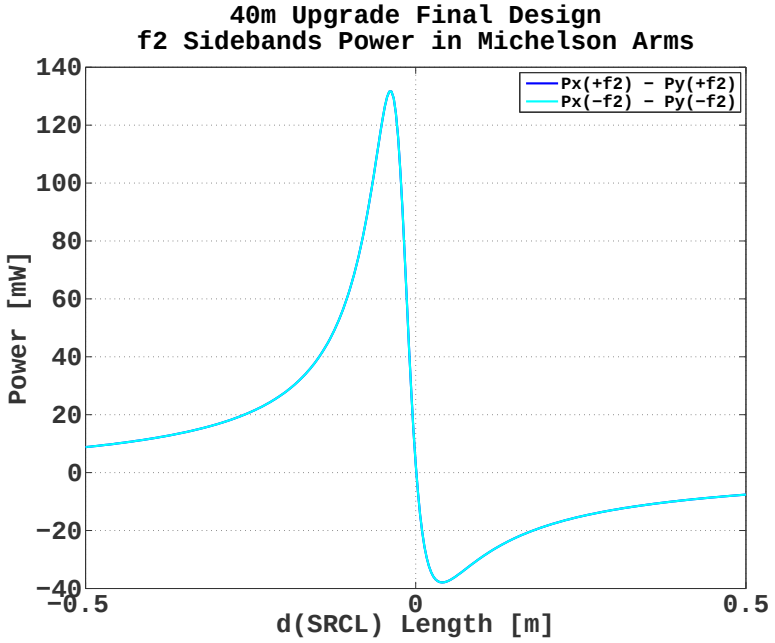

Figure 4.2: This plot shows how the presence of the signal recycling mirror causes a difference of the f_2 sideband field power between the two arms of the Michelson. The fields of the upper sidebands (+f2) and the lower sidebands (-f2) coincide: there is no sidebands unbalance.

No single parameter adjustment can compensate for the phase shift of the sidebands. The round-trip phase gain of each sideband depends simultaneously on 3 different parameters: PRC length, SRC length and Schnupp asymmetry. An analytical understanding of the cavity's response to the sideband fields is complicated by the many parameters involved. We therefore confront the problem with numerical simulations. With an iterative process, we explore the parameter space made by the recycling cavities' lengths and the Schnupp asymmetry.

The iteration's steps are:

1. PRC length tuning to make the f_1 sideband resonant in the cavity
2. SRC length tuning to equalize the sideband power in the Michelson arms
3. Schnupp asymmetry tuning to maximize the power of the f_2 sideband in SRC.

	Arms	PRC	SRC
Carrier	resonant	resonant	anti-resonant
f_1 **SB**	non-resonant	resonant	non-resonant
f_2 **SB**	non-resonant	max power	max power

Table 4.2: Summary of the conditions considered to determine an optimum set of parameters of the central interferometer.

Plots as in figures 4.3, 4.4, 4.5 were used to guide the iterations.

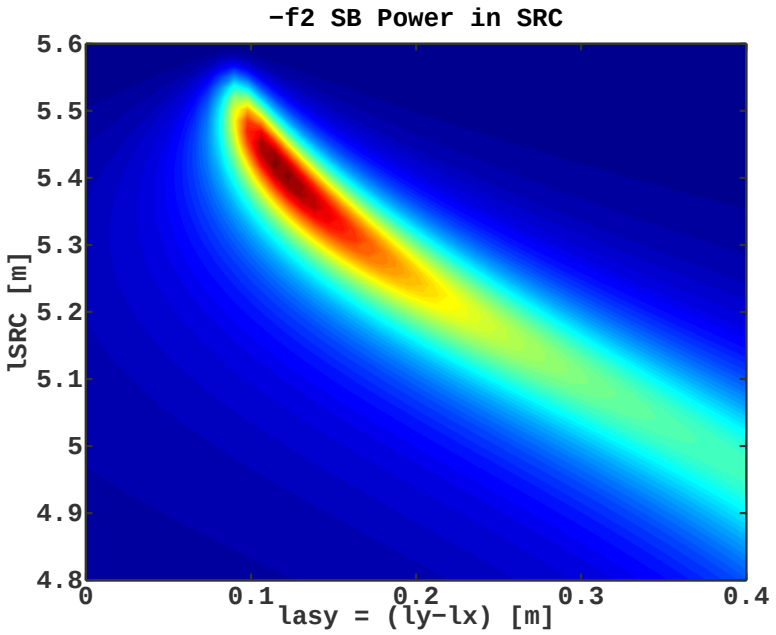

Figure 4.3: f2 sidebands power in the Signal Recycling Cavity. The critical coupling of f2 from PRC to SRC is approximated by maximizing the power in SRC (red = higher power).

The iteration converges to a solution that allows for the resonance of f_1 in the power recycling cavity to be restored. Also, the power of f_2 is balanced between the Michelson arms. Finally, the Schnupp asymmetry is set such that it maximizes the power of f_2 in SRC, though the critical coupling is no longer guaranteed (figure 4.5). The final design lengths are summarized in Table 4.3.

	Arms	PRC	SRC	Schnupp A.
Length [m]	38.4	6.7467	5.4225	0.0568

Table 4.3: Summary of design cavity lengths after compensating for the sidebands phase gain in the arms.

A sanity check on the transfer function between DARM and the dark port of the interferometer confirms the validity of the new set of parameters for the central cavity (see

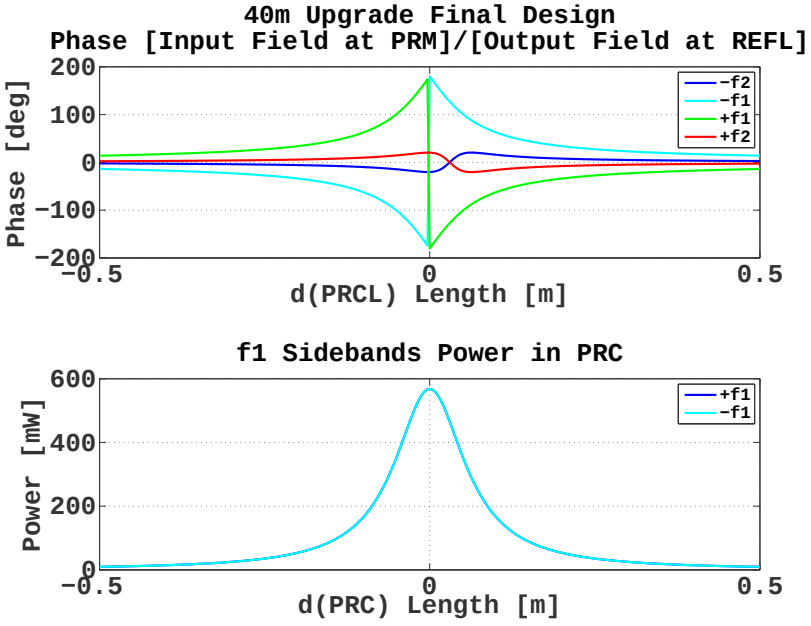

Figure 4.4: The resonance condition of f1 in the power recycling cavity is ensured by evaluating the reflectance of the interferometer to the sideband, as obtained from the ratio between the sideband field at the power recycling mirror and at reflection port REFL.

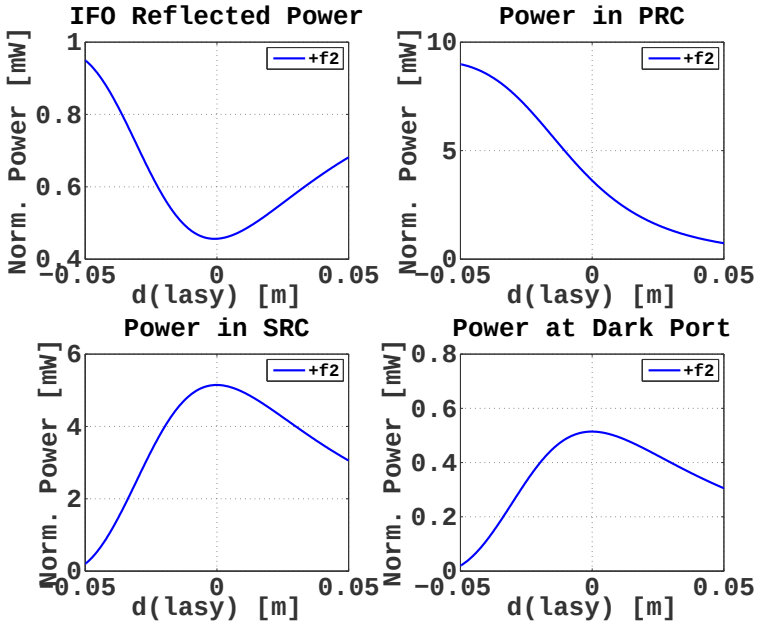

Figure 4.5: Clockwise: f2 sidebands power at the reflection port (REFL); power recycling cavity; signal recycling cavity; dark port (AS). Y axis normalized for the f2 power at the interferometer input (PRM). 50% of f2 is reflected, and 50% is transmitted to the dark port. f2 is not critically coupled from PRC to SRC as in the ideal arm length design.

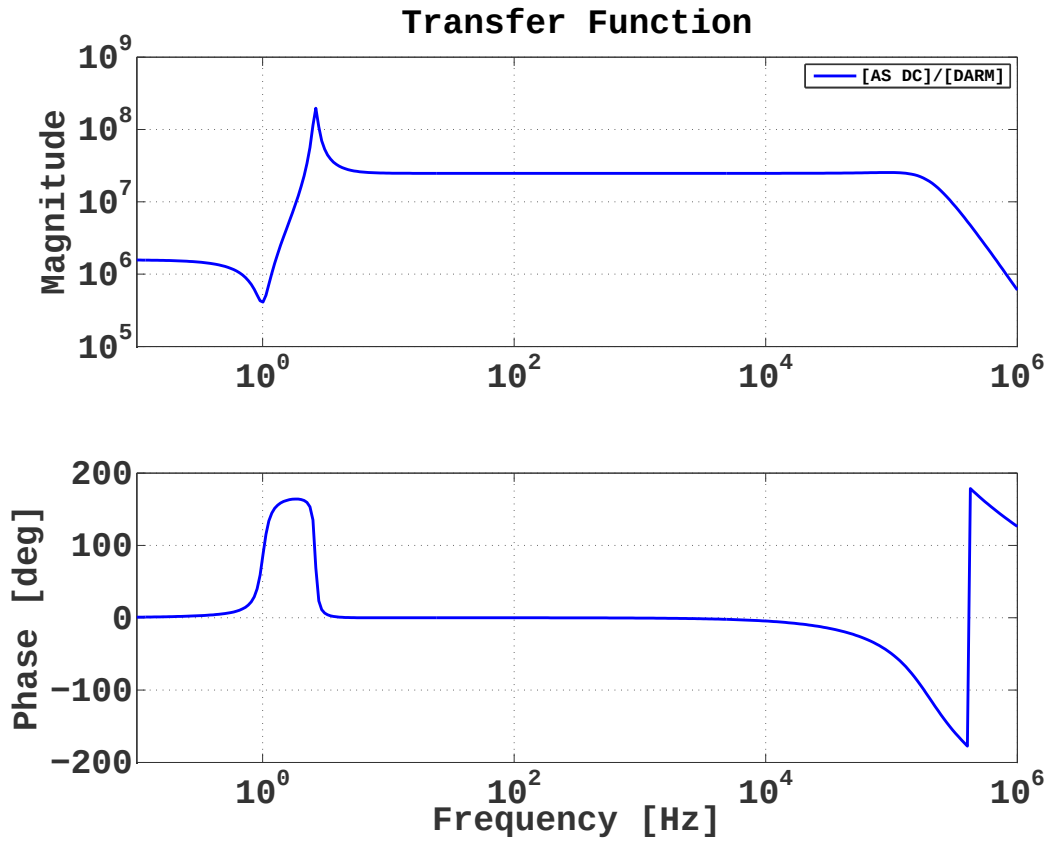

Figure 4.6: DARM to AS transfer functions. The cavity pole at 160 KHz agrees with expectations for the arm-SRC resonant coupled cavity. The peak at about 3 Hz is due to radiation pressure [21].

figure 4.6). The transfer function has a pole at 160 KHz, consistent with the expectations for the 40m resonant arm-prc coupled cavity (see sec. 2.5.1).

4.2 Optics Parameters

Selection of optics parameters such as radius of curvature and transmissivity simply follows the constraints of the optical design. The transmissivities of the optics are chosen first, implementing the design finesse and power at the ports. Finally, the radii of curvature are designed to allow for beam mode matching.

Cavity Finesse

The initial Advanced LIGO design of the arm cavity included a finesse of 1250 with the intention of reducing the power through the ITMs' sapphire substrate. As the final choice for the test mass substrate was diverted to fused silica, the support for a high finesse was outweighed by the other advantages that a lower finesse offers (i.e. easier lock acquisition). A finesse of 450 was retained for the final design and a more stringent requirement of 75ppm

round-trip loss was set. The ITM transmissivity was increased from 0.5% to 1.4% [37].

Mirror Radius of Curvature

The 40m ITMs are flat mirrors (RoC = 5625 m) and because of that they host the beam's waist. To guarantee beam mode matching to the arm cavity, the curvature of the end mirrors has to be:

$$\mathrm{RoC}_{etm} = L_{arm} + \frac{z_R}{L_{arm}} \tag{4.2}$$

where z_R is the Rayleigh range of the beam, which is related to the beam waist $w_0 = 3$mm by

$$z_R = \frac{\pi w_o^2}{\lambda}.$$

and $L_{arm} = 38.4$m is the arm cavity length.

The radius of curvature of the PRM and SRM are chosen to match the arm cavity mode using equation 4.2, with $L_{prc} = l_{pr-bs} + (l_x + l_y)/2$ and $L_{src} = l_{sr-bs} + (l_x + l_y)/2$ in place of the cavity lengths. Also, care must be taken to include the extra optical length due to the beam travel through the silica substrate of the ITMs and the beam splitter (the latter only for the signal recycling cavity). Table 4.4 shows the resulting design parameters.

	ITMs	**ETMs**	**PRM**	**SRM**
RoC [m]	5625	57.375	115.5	142
T	0.014	1.5×10^{-5}	0.055	0.10

Table 4.4: Design radii of curvatures and transmissivities calculated using the ideal optical parameters of table A.3.

Cavity g-Factor

The laser field transverse profile on the x and y direction, for a beam propagating along the z axis, can be expressed with the orthogonal set of Hermite-Gaussian functions $u_n(x, z)$ and $u_n(y, z)$, respectively [17]. With these it is possible to construct a basis of modes for the field such that the field can always be expanded as

$$E(x, y, z) = \sum_{0}^{\inf} E_{nm} u_n(x, z) u_m(y, z) e^{i(\omega t - kz)}. \tag{4.3}$$

The laser field behaves differently from a plane wave: the phase along the z axis does not depend only on kz, but it also includes the complex argument of $u_n(x, z)u_m(y, z)$. This contribution to the total phase is called *Guoy phase* Φ_{guoy} and it is an important factor for determining the resonance conditions of the field within an optical cavity. A Fabry-Perot cavity can be constructed to be resonant for any of the laser modes and the parameter that determines the resonant condition for a (n, m) mode is called the *g-factor*, and it is

defined as

$$g = \sqrt{\left(1 + \frac{L}{R_1}\right)\left(1 + \frac{L}{R_2}\right)} \tag{4.4}$$

where L is the length of the cavity, and R_1 and R_2 are the radii of curvature of the input and output mirrors, respectively. The conditions for which an optical cavity is resonant for the (n, m) mode define a cavity mode, denoted with TEM_{nm}.

Using the cavity lengths from table 4.3, we can obtain the cavity g-factor and transverse mode spacing of table 4.5.

	Arms	**PRC**	**SRC**
g-factor	0.3285	0.9405	0.9609
FSR [MHz]	3.904	22.218	27.643
TMS [MHz]	1.1934	1.7433	1.7518

Table 4.5: Cavity g-factors and Transverse Mode Spacing (TMS) for the 40m cavities with the adjusted lengths as in Table 4.3.

4.3 Design of Length Sensing and Control Signals

The derivatives of the sensing signals measured from the ports (see sec 3.3) with respect to the motion of the degrees of freedom are called *frequency discriminants* [34]. They basically represent the slope of the PDH error signals around the working point. The matrix that collects all possible frequency discriminants from each DOF to any channel is called the *sensing matrix*. Of all the components of this matrix only a few are used to effectively control the interferometer. The choice of which to use is based on the state of the interferometer. At any time, the desirable sensing matrix is the most diagonal one, because it allows for less coupling between the degrees of freedom.

During lock acquisition, which brings the interferometer into science mode, the set of control signals is switched as the frequency response of the degrees of freedom varies (see sec. 4.4 for more). This process is rather complex, since the physical plant of the interferometer can depend significantly on the microscopic state of the optical cavities. This has been thoroughly analyzed for initial LIGO in [38], Advanced LIGO in [39] and the 40m in its configuration before to the 2010 upgrade in [21].

4.3.1 Sensing Matrices

The calculation of the optical sensing matrix for science mode can be obtained by numerical simulation tools such as Optickle [40]. Table 4.6 shows the result for the 40m Upgrade configuration with the parameters listed in table 4.3. In this open loop computation, the CARM mode dominates all signals, except for the one at the dark port. A dedicated

control loop for CARM can be used to suppress the motion below the point where the contributions from the other degrees of freedom are recovered [34, 41].

(a)

	PRCL	**MICH**	**SRCL**
POP1 Q2	3.0e+03	**-7.5e+03**	-7.1e-01
POP1 I1	**7.9e+04**	-2.8e+02	8.2e+01
POP1 I2	-6.6e+03	-1.1e+03	**8.1e+03**

(b)

	PRCL	**MICH**	**SRCL**
POP1 Q2	1.5e+03	**3.8e+03**	3.6e-01
POP1 I1	**4.0e+04**	1.4e+02	4.1e+01
POP1 I2	3.3e+03	5.4e+02	**4.0e+03**

Table 4.6: Sensing matrices for the short degrees of freedom, in W/m at DC (a) and at 100 Hz (b). The arm cavities are excluded. The dominant discriminants of the matrix are the same at all frequencies.

Following this analysis we proposed the set of control signals in table 4.7. Simulations

CARM	**DARM**	**MICH**	**PRCL**	**SRCL**
REFL I1	AS DC	POP1 Qf_2	POP1 If_1	POP1 If_2

Table 4.7: Set of control signals chosen to control the interferometer in a full lock state.

confirmed the linearity of the proposed error signals (figure 4.7). Linear ranges around a few nanometers are guaranteed for the degrees of freedom.

DARM Error signal for DC Readout

Figure 4.7 shows the quadratic dependece of the dark port's DC power on the DARM displacement. The DARM offset imprinted on the arms brings the working point to one side of the parabola, where the derivative of the signal is not zero. There one has to apply a correction to the signal to recover the linearity with DARM. Following [42], for a small displacement of DARM around the nominal offset x_0, the power at the dark port P_{AS} is:

$$P_{AS} \simeq P_0 \left(\frac{x_0^2 + 2x_0\delta x + \mathcal{O}(\delta x^2)}{x_f^2} \right) + P_0\kappa. \tag{4.5}$$

where x_f is the fringe width, κ a unit-less constant and P_0 the power output at the DARM offset. Solving for the DARM signal, one gets:

$$\delta x = \frac{x_f^2}{2x_0}\left[\frac{P_{AS}}{P_0} - \kappa\right] + \frac{x_0}{2}. \tag{4.6}$$

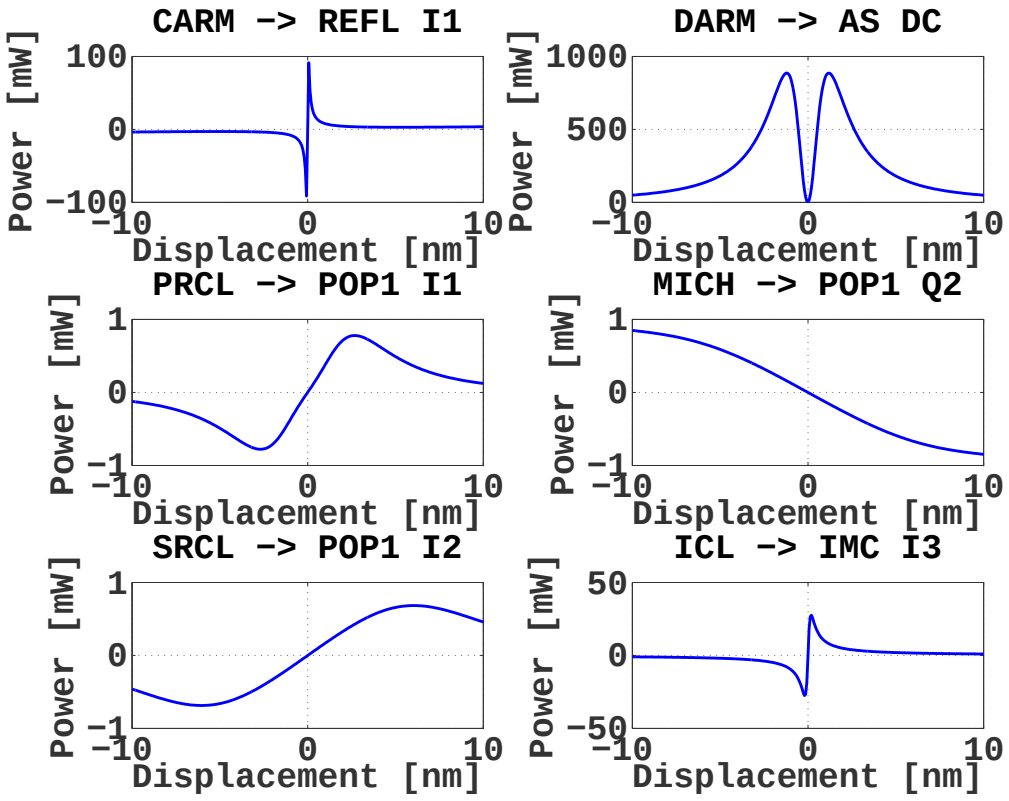

Figure 4.7: The error signals chosen for controlling the interferometer (tab. 4.7) in locked regime are plotted. Linear ranges of about few nanometers are guaranteed.

where the various constants can be obtained empirically.

4.3.2 Modulation Depth

The modulation depth, which defines the amplitude of the sidebands (cfr. section 2.4.1), must be chosen to minimize the differential arm length displacement noise due to shot noise [3]. The light at the dark port is the sum of the f_2 sideband transmitted by the SRM and the carrier leaked through a contrast defect at the beam splitter (i.e. when a DARM offset is induced). The carrier power ($\propto J_0(\Gamma)^2$) and the sideband power ($\propto J_1(\Gamma)^2$) introduce non-stationary shot noise [43]. Following [22], the noise at the port is then:

$$S_{AS_Q} = 2\sqrt{P_{in}h\nu\left[J_0(\Gamma)^2 g_{cr}^2 c_d + \frac{3}{2}2J_1(\Gamma)^2 t_{sb}^2\right]} \tag{4.7}$$

where g_{cr} is the carrier gain in the coupled cavity, $c_d \equiv P_{AS}/P_{BS}$ is the contrast defect, and t_{sb}^2 is the transmissivity of the sideband through the dark port.

The electronics noise of the photodiodes come into play as well, and one must ensure that, for the chosen modulation depth, shot noise remains dominant (see Appendix C).

	REFL	AS	POP1	POX	POY
-110.654	0.045	0.000	0.000	0.000	0.000
-66.392	0.181	0.000	0.000	0.000	0.000
-55.327	10.650	0.001	0.060	0.046	0.043
-44.262	0.181	0.000	0.000	0.000	0.000
-22.131	0.045	0.000	0.000	0.000	0.000
-11.065	14.256	0.000	0.568	0.283	0.284
0	2.010	0.248	17.207	8.596	8.595
11.065	14.256	0.000	0.568	0.283	0.284
22.131	0.045	0.000	0.000	0.000	0.000
44.262	0.181	0.000	0.000	0.000	0.000
55.327	10.650	0.001	0.060	0.046	0.043
66.392	0.181	0.000	0.000	0.000	0.000
110.654	0.045	0.000	0.000	0.000	0.000

Table 4.8: Field power in mW at the 40m ports. First column is Frequency (in MHz). Values computed according to the adjusted optical design of September 22 2010. Laser power: 2W; modulation depth 0.2

Fields Power at the Ports

In order to tune the modulation depth so the signals at the ports are shot noise limited, we computed the expected power in the RF signals as measured before demodulation (table 4.9). To better understand the RF signals power, we also computed the powers in the fields at each port (table 4.8). A modulation depth ranging between 0.1 and 0.2 proved equally good in overcoming electronics noise at the photodiodes (Appendix C).

PD	DC	f1	f2	3f2	3f2
REFL	53	3.8e-03	3.4e-03	3.0e-05	7.4e-06
AS	0.25	2.8e-03	3.2e-02	1.9e-05	1.3e-05
POP1	1.8e+01	7.1e-05	1.4e-05	3.0e-07	7.4e-09
POX	9.3	2.5e-02	1.0e-02	1.0e-04	5.8e-06
POY	9.3	2.5e-02	9.8e-03	-	-

Table 4.9: RF power at the ports for the frequencies: $f1$, $f2$, $3 \times f1$ and $3 \times f2$. First column is Frequency (in MHz). Values computed as in the adjusted optical design of September 22 2010. DC Readout: DARMoffset=10pm; fields computed up to the 5th order modulation for each SB. Laser Power: 2W

4.4 3f Signals for Lock Acquisition

Bringing the interferometer from a completely uncontrolled state to science mode involves several intermediate stages, during which the control of the degrees of freedom is handed off from one set of error signals to another. The lock of the 5 main cavities is acquired gradually. Initially, the central cavities are locked and the arms are brought close to resonance, with a CARM offset from resonance (about 50% of full cavity power). Then the arm cavities are slowly brought into lock until the circulating power ramps up to its maximum. The transition to this state is very critical for the fields circulating in the central part, since the phase of the carrier experiences a rotation as the arms become resonant. As the end mirrors move from a few picometers away to perfect resonance, the reflectance of the arm cavities suddenly flips sign, passing from -1 to 1, and consequently any error signals used to control the short degrees of freedom (MICH, PRCL, SRCL) that would rely on the beat of the carrier with a sideband become destabilized (see figure 4.8).

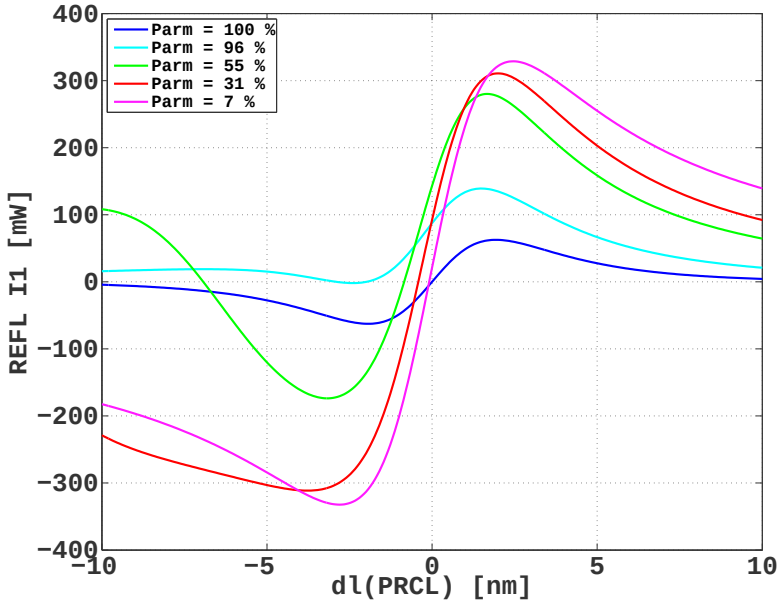

Figure 4.8: Optickle 1f error signals for different PRCL offsets (dl)

The solution previously adopted at the 40m to circumvent this problem was the so called *double-demodulation signals*. In this scheme, the control of the central cavities is made independent from the carrier by using the beat between the two RF sidebands f1 and f2. This approach was problematic during the Advanced LIGO prototyping at the 40m in 2004-2009. The main complication was the presence of unwanted offsets in the error signals that made the locking point prone to displacements, shifting the cavities from their ideal locked state. This was attributed to the difficulty in controlling the double-demodulation phases, which proved to be very sensitive to changes in the optical plant of the interferometer [21].

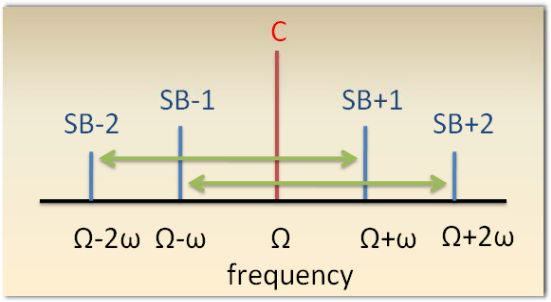

Figure 4.9: Bessel sideband expansion for a modulation at frequency Ω over a carrier ω. 3f signals are produced by interference between second order and first order modulation sidebands.

A second approach, the *3f demodulation* scheme (or simply *3f*) [44], developed at the TAMA300 gravitational wave interferometer in Tokyo, Japan [45] is the proposed solution for the 40m Upgrade. Rather than using the beat between two different RF sidebands generated by two separated modulation systems, as in double-demodulation, in 3f the discriminants are obtained from beat-notes between sidebands of different orders of the same modulation (figure 4.9). The beat may arise from interference between J_2 with J_{-1}, or between J_{-2} with J_1, using the Bessel coefficient to call them. The $J_{\pm 2}$ sidebands act as local oscillator and provide a stable phase reference against which to measure the phase of the $J_{\pm 1}$ sidebands. The 3f signals proved to be much more decoupled from CARM, and they can serve to hold the central part locked until full lock is reached by the arms. Then hand off to the standard signals as in 4.7 would eventually bring the interferometer into science mode.

Using an analysis similar to that which identified a set of control signals for the full locked interferometer, we defined the sensing matrix for the central part based on 3f signals shown in table 4.9(a). This combined with the analysis of the error signals (figure 4.10), enabled us to define a set of control signals for the central part, as in table 4.9(b).

(a)

	PRCL	MICH	SRCL
REFL I3f1	**7.9e+06**	1.3e+05	9.5e+04
REFL Q3f1	3.0e+04	8.2e+04	**1.8e+05**
REFL I3f2	**2.0e+05**	1.6e+05	6.2e+04
REFL Q3f2	1.3e+05	5.8e+04	**2.0e+05**
POX I3f1	**1.3e+03**	6.9e+01	4.5e+01
POX Q3f1	**3.9e+03**	2.8e+02	1.9e+01
POX I3f2	**1.6e+02**	8.8e+01	4.1e+01
POX Q3f2	8.2e+01	6.8e+01	**1.3e+02**
POP1 I3f1	**2.5e+03**	1.6e+02	4.0e+01
POP1 Q3f1	**8.3e+03**	3.3e+02	8.1e+00
POP1 I3f2	**1.8e+02**	7.6e+01	1.6e+02
POP1 Q3f2	5.1e+01	5.4e+01	**1.0e+02**

(b)

MICH	PRCL	SRCL
REFL Q $3f_2$	REFL I $3f_1$	REFL I $3f_2$

Table 4.10: (a) Matrix of discriminants of 3f error signals. Demod phase set as: REFL I3f1 for PRCL, REFL I3f2 for SRCL and the others for MICH. (b) 3f set of control signals.

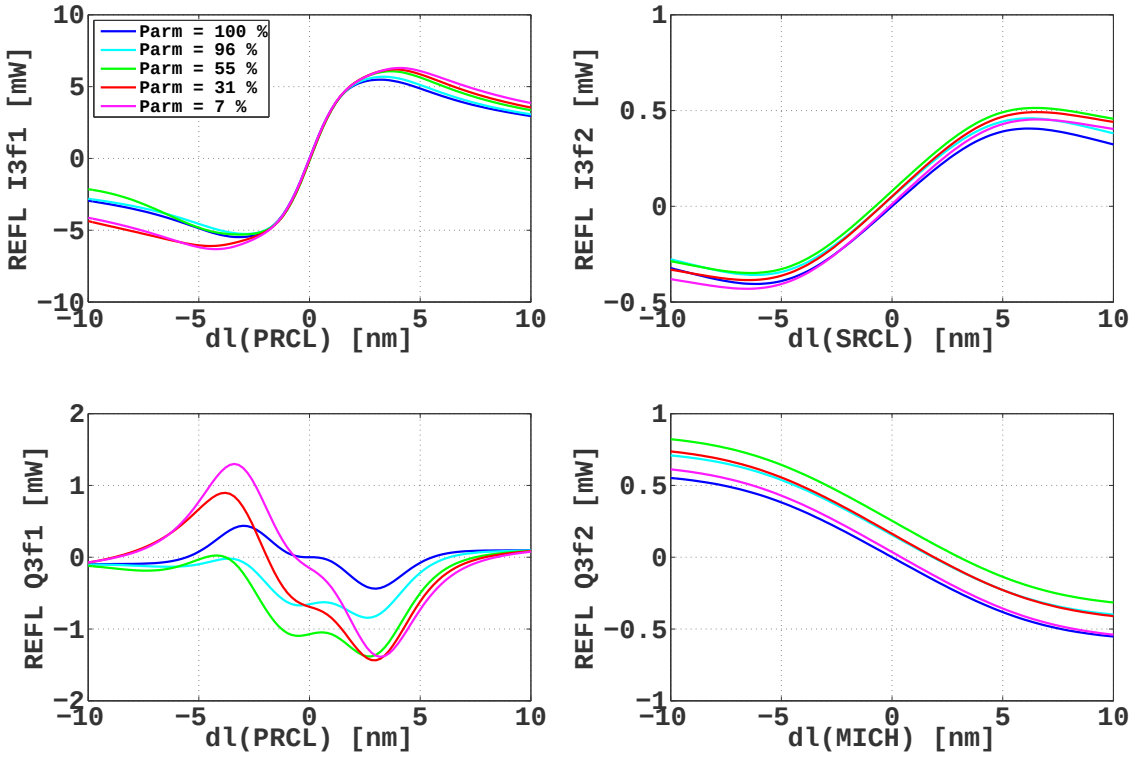

Figure 4.10: Optickle 3f error signals for different CARM offsets

4.5 Summary of Results

We studied an ideal optical design of the 40m interferometer in order to implement the Advanced LIGO length sensing and control scheme. Facing the constraints imposed by the lab facility, we modified the 40m baseline design and a new set of design parameters has been proposed. Simulations showed that the adapted configuration preserves the interferometer sensitivity to differential arm motion. A set of signals to control the degrees of freedom in full lock regime has also been proposed. Finally, we defined a set of control signals for lock acquisition based on the 3f signal extraction technique.

Chapter 5

Dependence of Control Signals and Noise on Cavity Absolute Length

Work previously done at the 40m demonstrated that upper and lower sidebands may become unbalanced in the recycling cavities of a detuned dual-recycled interferometer [21]. In these circumstances, some of the control signals, specifically the ones obtained by double demodulation (cfr. section 4.4), may acquire static offsets and shift the locking point of the cavities from resonance. As a result, the interferometer's overall performance deteriorates: the common mode noise rejection performed by the Michelson is partly spoiled; and optical coupling routes open for laser and oscillator noise to the dark port. The control of the interferometer is also affected by microscopic offsets: the optical plant of the interferometer becomes less diagonal and more dependent on the microscopic state of the cavities; cross-talks between the degrees of freedom increase. This also increases the noise at the dark port, since the control loops provide larger noise couplings.

We used numerical simulations to investigate whether similar, or other effects, may arise from *macroscopic* offsets of the cavity lengths from the nominal values. Since the optical design of the 2010 40m prototype includes these kind of offsets (cfr. section 4.1.1), this study provides tools immediately applicable to the construction of the interferometer.

5.1 Open-Loop Analysis

In this chapter we will consider an ideal model of the 40m in which the arm cavity lengths are such that the f1 and f2 sidebands are nearly anti-resonant (Appendix A). The lengths of the other cavities are set according to the RSE conditions listed in Table A.2. On top of this model, we will consider macroscopic offsets on the main degrees of freedom: CARM, DARM, MICH, PRCL, SRCL. Throughout our analysis the interferometer will always be virtually fully locked; that is, with zero microscopic offsets on all degrees of freedom. In this section, we will also consider a virtual state without control loops to maintain lock. In section 5.2, these loops will be closed. Now, however we will focus on the *optical* effects of macroscopic offsets.

5.1.1 Sideband Imbalance Due to Arm Length Mismatch

Upper and lower sidebands become unbalanced by going through a cavity that has an asymmetric response for frequencies around the carrier. This is the case, for instance, when the phase accumulated by the carrier in the cavity is less than π radians (modulo π) (i.e. when the cavity is detuned [41]). The gain of power recycling cavity and signal recycling cavity, and the Michelson reflectivity are symmetric for frequencies around the carrier, if this is either exactly resonant or anti-resonant. Simulations of macroscopic offset in the main degrees of freedom confirmed that, in an open loop state of the interferometer, sideband imbalance does not occur and cavity locking points do not shift from resonance.

5.1.2 Sideband Asymmetry in the Michelson

As discussed in section 4.1.1, in a signal recycled interferometer, CARM and DARM macroscopic offsets may introduce asymmetries between the RF sideband power between the two Michelson arms. At the 40m, the ratio between the power of the f2 sidebands in the short Michelson x-arm (l_x) and y-arm (l_y) is maximum for a CARM macroscopic offset with the arm cavities about 10 cm off from the resonance of f2, which is about 10% of the modulation's resonant length $\lambda_{f2}/4 = c/(4f2)$ (figure 5.1).

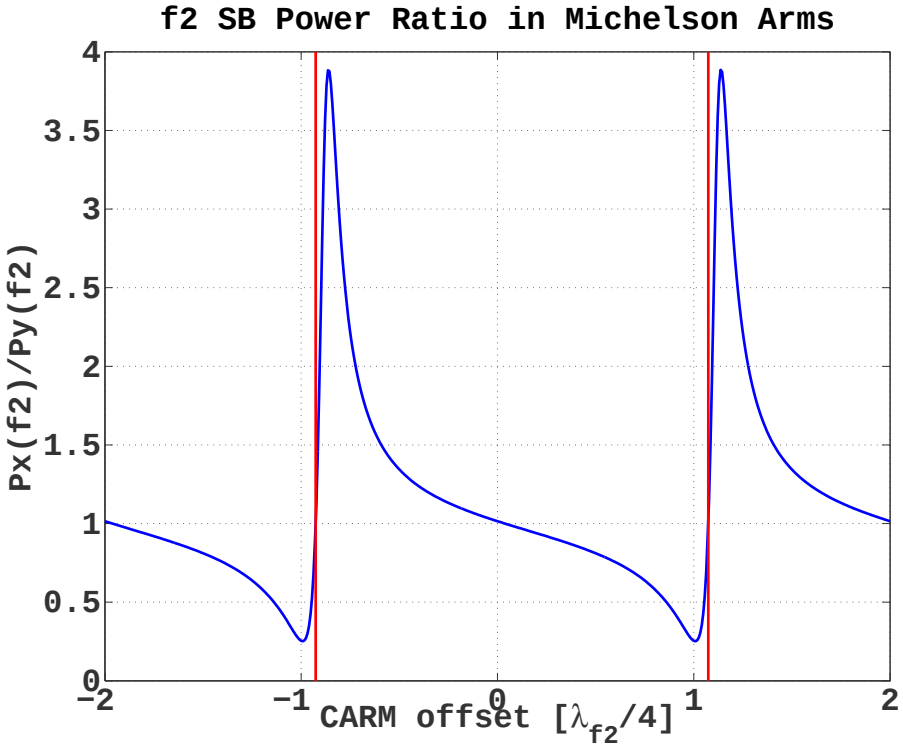

Figure 5.1: The power of the f2 sidebands is different in the two arms of the Michelson (between BS and ITMs) if there is a CARM macroscopic offsets. The plots above show the f2 sidebands power ratio versus macroscopic offset in units of the f2 modulation's resonant length $\lambda_{1/4} = c/(4f_2)$. The red lines mark the f2 arm resonances. The result proved to be independent from the DARM microscopic offset used for DC readout.

For a realistic offset $\Delta_{\mathrm{CARM}} < 0.20$ m, the power change in the two arms is approximately linear:

$$P_x \approx P_y(1 - \Delta_{\mathrm{carm}}/2). \tag{5.1}$$

For $\Delta = 0$, $P_x = P_y \approx 200$ mW, and in the linear region where $\Delta < 0.20$ m, $P_x - P_y < 10$ mW, that is about 10% different from P_x and P_y when the CARM offset is zero.

A 1-2% difference between P_x and P_y is caused by the small CARM offset $\delta = 0.10$ m present also in the nominal optical design[1]. Since this is unavoidable, the CARM macroscopic offset should be limited to it: any other asymmetry between P_x and P_y is highly undesirable and should be avoided. CARM should be set within 1-2 cm from the design value, or, in general, within less than 1% of the f2 modulation's resonance length $\lambda/4 = (c/4f2)$.

The DARM macroscopic offset has no effect on the power balance between the two Michelson arms, except for very large offset values, where f2 begins to resonate in the arm cavities. Starting from a DARM offset of $\lambda_{f2}/4$ (about 1 m at the 40m), the power ratio increases until the point where the power in one arm exceeds the other by several orders of magnitude (figure 5.2). Our analysis showed that this effect of DARM is due to the residual $\delta = 10$ cm in CARM; it can be avoided simply by ensuring that the DARM macroscopic offset is less than $\lambda_{f2}/4$.

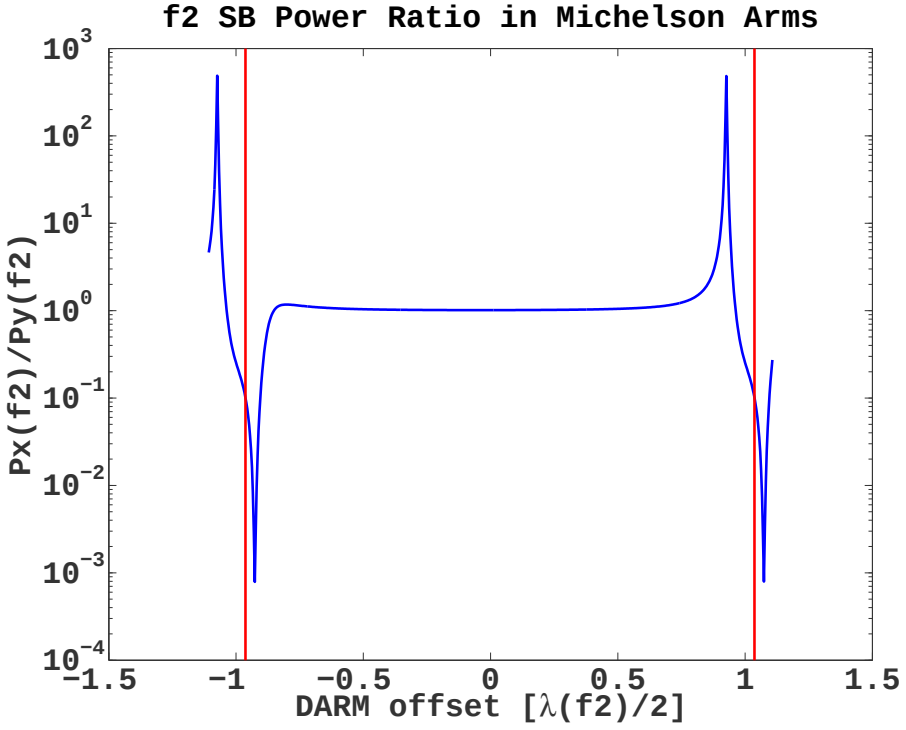

Figure 5.2: DARM macroscopic offset. The red lines mark the f2 arm resonances. The spikes are a consequence of the CARM offset $\delta = 10$ cm included in the interferometer optical design. This effect is not caused by the DARM *microscopic* offset used for DC readout.

[1]The purpose of δ is to avoid resonances of the sidebands' even harmonics

The symmetry of the Michelson appears to be broken by the fact that PRC and SRC have different lengths: each ITM sees the rest of the interferometer as a compound mirror with different reflectivity. In fact, the effect is present in our simulations when the signal recycling mirror is absent.

In a real interferometer it is highly undesirable to have differences in sideband power between the Michelson arms, since important signals, such as those from POX, POY, POP, and SPOB, are obtained from the fields in those segments of the central cavity.

5.1.3 Error Signals

Introducing PRCL and SRCL macroscopic offsets may also break the anti-resonant condition for the sidebands in the arm cavities: the sidebands acquire a non-zero phase upon reflection from the ITMs, which affects their resonance conditions and power buildup in the recycling cavities with direct consequences on the interferometer's sensing matrix (fig.5.3).

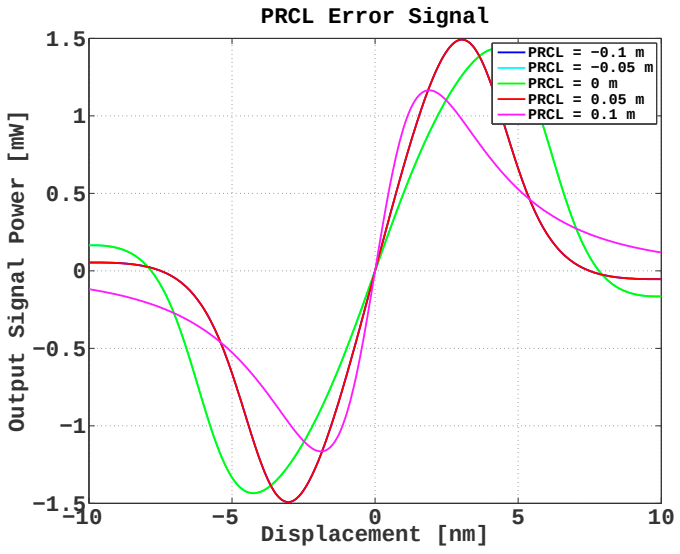

Figure 5.3: PRCL error signal change for different macroscopic offsets of the power recycling cavity. The demodulation phase is re-tuned at each offset value. The blue and the cyan plot are covered by the red and the purple lines, respectively: the cavity field responds symmetrically to negative and positive offsets.

Dependence of 3f error signals on cavity absolute length

The 3f signals can be affected by mismatches of cavity absolute lengths from the nominal values (see table A.3) in three ways:

1. the phase of the $J_{\pm 2}$ sidebands depends on the CARM offset
2. the upper and lower sidebands $J_{\pm 1}$ are reflected differently by the interferometer
3. $J_{\pm 3}$ sidebands also appear on the photodetector

The first situation occurs when the $J_{\pm 2}$ sidebands are not completely reflected by the interferometer. This is the case when the RF sidebands are exactly anti-resonant in the arm and their even harmonics are resonant. At the 40m an offset $\delta = 10$ cm is sufficient to avoid that region (cfr. A.3).

The second point depends on the asymmetric reflectivity of the recycling cavities for microscopic offsets in PRCL and SRCL. When PRM or SRM swing around their locking position the reflectivity of the interferometer for J_{+1} and J_{-1} are different (i.e. red and green lines in figure 5.4).

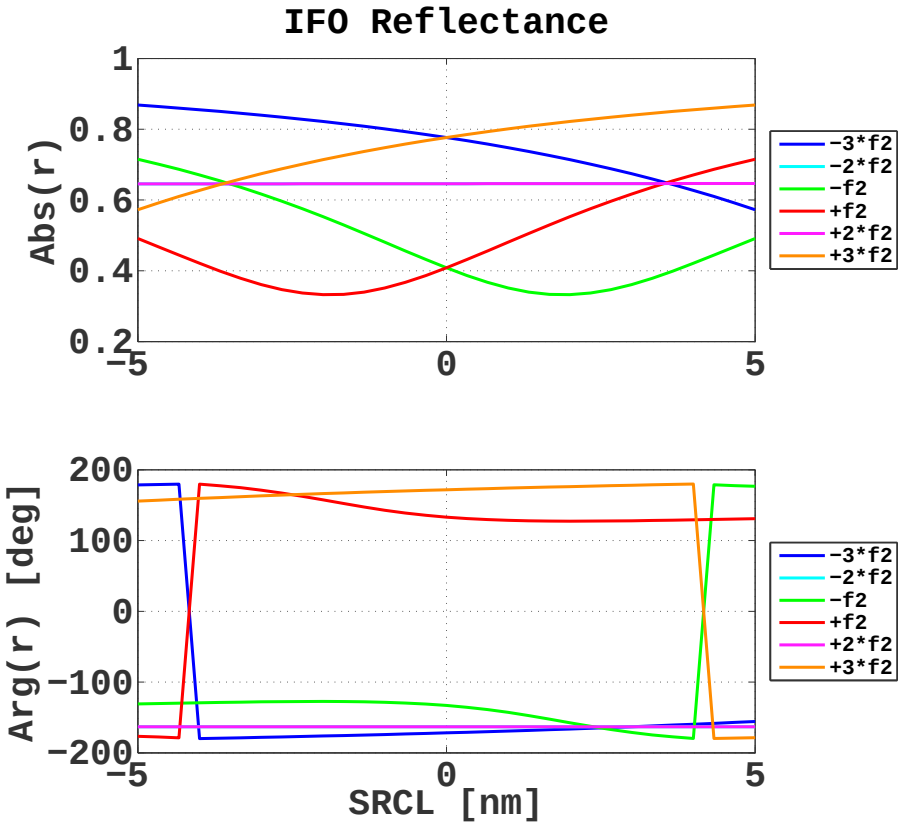

Figure 5.4: Interferometer reflectances for the first three modulation orders of the f2. Obtained from the ratio of the fields entering the power recycling mirror and the field at the symmetric port.

The third case is due to the contribution of 3rd order sidebands present in the beam. These beat against the carrier and add offsets to the 3f demodulation signals, causing the cavity locking point to shift (figure 4.10). Simulations of the 40m error signals reveal locking point offsets of less than 1 nanometer. Since the 3f signals are intended only for the transition stage to the full lock, this offset is considered tolerable.

Figure 5.5 shows how a small macroscopic offset of 10 cm in the length of the power recycling cavity can also spoil the 3f error signals. To avoid this, the recycling cavities should be set at their nominal lengths with sub-millimeter precision.

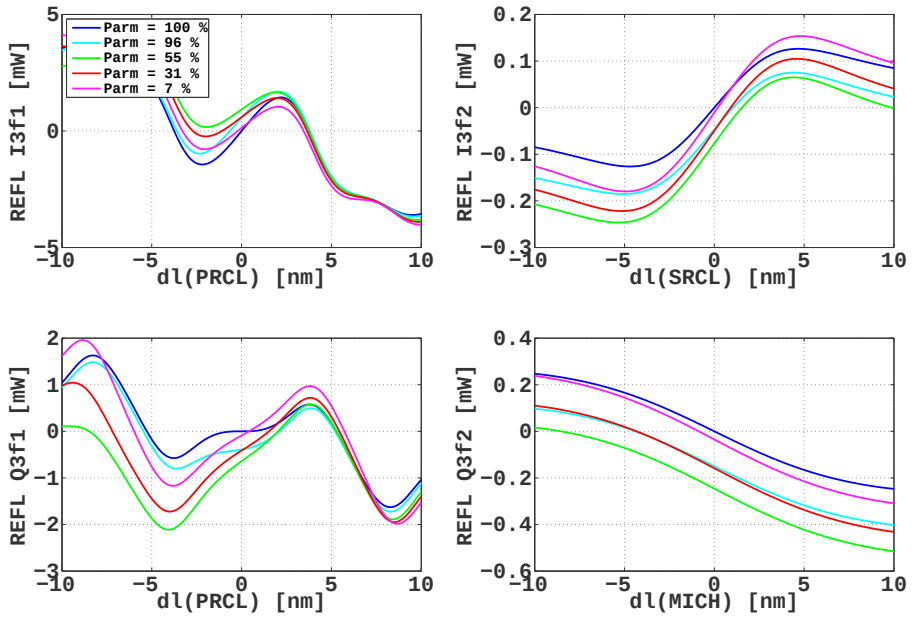

Figure 5.5: 3f error signals for a 1 cm macroscopic offset in PRCL from the ideal lengths of the 40m Upgrade as in table A.3.

5.1.4 Optical Noise Couplings

The laser that illuminates the interferometer, and the oscillator used to generate the modulation sidebands are both affected by amplitude and frequency noise. These noises appear as acoustic sidebands around carrier and RF modulation sidebands, potentially masking the gravitational wave signal. As explained in section 2.5, the optical plant of the interferometer is designed with the goal of rendering the dark port as immune as possible to common mode noise sources, such as laser and oscillator frequency and amplitude noise. In principle, a Michelson interferometer should provide a perfect solution for that. In reality, several factors intervene to spoil the noise cancellation at the dark port.

Any asymmetry in the Michelson prevents it from perfectly decoupling common and differential modes. Contrast defects, due to differences in losses between the arm cavities, allow extra light to leak to the dark port. The DARM offset imposed for DC readout also offers a path for laser noise to couple into the dark port by directly changing the interference contrast. Arm finesse imbalances, due to different reflectivity between the input optics, cause slightly different filtering for the carrier's sidebands, preventing common noises from perfectly canceling[46].

From [47] we can write the contributions of these asymmetries as the following:

$$\Delta r_c = \frac{\xi}{1+s_c} + \frac{2s_c}{(1+s_c)^2}\frac{\Delta\mathcal{F}}{\mathcal{F}} + \frac{2i}{(1+s_c)^2}\frac{\omega_0 \Delta L_-}{\omega_c L}. \tag{5.2}$$

where s_c is the arm cavity pole; ω_0 the carrier frequency; $\Delta\mathcal{F}$ the finesse imbalance; ΔL_- the DARM microscopic offset; and ξ the contrast defect .

In a DC readout configuration, the most relevant optical couplings are those from the

input laser. For a power recycled Michelson it is possible to express these couplings in an analytical form. From 5.2, using the two-photon formalism, and according to [47], in the absence of a signal recycling mirror, we can write in the following expressions the couplings of laser input frequency noise $d\nu$ and intensity noise dP into both the amplitude and phase quadratures of the field a_1 and a_2 at the transmission side of the beam splitter:

$$\begin{aligned} a_1 =& -\frac{\pi\delta\nu}{\sqrt{2}\omega_a}\frac{2}{(1+s_{cc})(1+s_c)}\frac{\omega_0\Delta L_-}{\omega_c L} \\ &+ \frac{1}{4\sqrt{2}}\frac{\delta P}{P}\left\{\frac{\xi}{1+s_{cc}} + \frac{2s_c}{(1+s_{cc})(1+s_c)}\frac{\Delta\mathcal{F}}{\mathcal{F}}\right\} \\ a_2 =& \frac{\pi\delta\nu}{\sqrt{2}\omega_a}\left\{\frac{\xi}{1+s_{cc}} + \frac{2s_c}{(1+s_{cc})(1+s_c)}\frac{\Delta\mathcal{F}}{\mathcal{F}}\right\} \\ &+ \frac{1}{4\sqrt{2}}\frac{\delta P}{P}\frac{1}{(1+s_{cc})(1+s_c)}\left\{\frac{2\omega_0\Delta L_-}{\omega_c L}\right. \\ &\left.+ \mathcal{K}(1+s_c)^2 \times \left[\sigma + \frac{\Delta\omega_c/\omega_c}{(1+s_c)^2} + \frac{\Delta m}{2m}\right]\right\}. \end{aligned} \tag{5.3}$$

where s_{cc} is the coupled cavity pole and the latter three terms are technical radiation pressure noise, with Δm being the difference between the masses of the suspended optics [21].

In a dual recycled interferometer, the noises in 5.3 are partially reflected by the signal recycling mirror back into the differential mode of the interferometer, further complicating the response to input noise.

The expressions in 5.3 do not contain any relevant contribution from a possible macroscopic offset in CARM or DARM. This is expected only if the noise around the carrier is considered, since this depends on the microscopic offsets, rather than on the absolute cavity lengths. However, experimental work previously conducted at the 40m [21] confirmed the inadequacy of 5.3 in predicting the actual noise couplings in the interferometer, since the optical couplings account only for a fraction of the overall noise. Most often, the largest contribution is indirect, and it comes from the control loops. The main coupling routes for laser and oscillator noise are listed in Table 5.1.

DC Readout Noise Couplings			
Laser Noise		**Oscillator Noise**	
Intensity	**Frequency**	**Amplitude**	**Phase**
AS DC $\propto$ RIN	Arm cavity finesse unbalance; $\propto f^{-1}$ above coupled cavity pole ω_{cc}	Noise in auxiliary degrees of freedom and carrier amplitude noise complementary to SB amplitude; $\propto f^{-1}$ above coupled cavity pole ω_{cc}	Noise in auxiliary degrees of freedom and sideband leakage through the OMC

Table 5.1: Main coupling routes in a DC readout signal extraction scheme.

5.2 Closed Loop Analysis

The sensing and control schemes described in section 2.6 may provide additional routes for laser and oscillator noise to couple into the readout signals of the interferometer's degrees of freedom. Figure 5.6 shows how noise at the interferometer's input can appear on the sensing channels in the simplified case of a system with only two degrees of freedom.

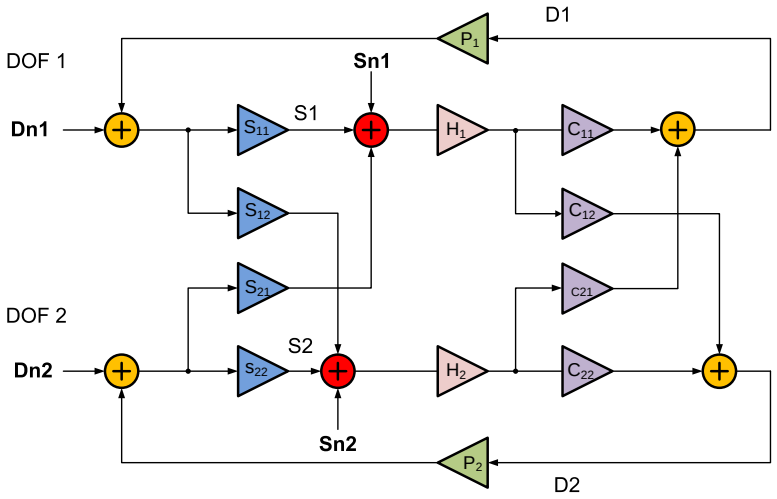

Figure 5.6: Loop couplings diagram for the simplified case of a system made with only 2 degrees of freedom. Each DOF also couples into the other DOF's sensing channel. Similarly the actuation on one DOF, also affects the other. In this way, displacement noise and sensing noise in one loop become displacement noise on the other.

Here S_{ij} are the elements of the sensing matrix from DOF i to sensor S_j; H_i the elements of a diagonal control matrix for the driving signal D_i; C_{ij} the driving matrix from H_i to D_j; finally P_i are the elements of a diagonal physical plant. Having assumed the main degrees of freedom as the basis for the sensing and control space, the physical plant of the interferometer is diagonal, and the cross-talk is due to non-diagonal sensing and driving matrices. In this general case, each sensor senses all DOFs because of the not perfectly diagonal form of the sensing matrix. Also the driving matrix is not diagonal, and trying to actuate onto only one DOF results in actuating the others too. The sensing noise on each sensor couples into all DOFs and the displacement noise of one DOF couples into the control loop of the other.

The real interferometer has multiple degrees of freedom and at least 6 of them are controlled simultaneously (CARM, DARM, MICH, PRCL, SRCL). To estimate the coupling of sensing noise due to common mode noise in the DARM signal we turned to numerical simulations. We computed the DARM displacement noise at closed-loop and distinguished the contributions of direct optical mechanisms from the contributions due to cross-coupling with other degrees of freedom. Indeed sensing noise in an auxiliary DOF also becomes displacement noise when a loop is closed onto it. Since the DARM sensor may sense all the other DOFs, this displacement noise can then be converted into actual DARM motion.

5.2.1 Noise Couplings

We simulated laser and RF modulation oscillator noise couplings to DARM 40m's ideal optical design (cfr. section 4.1.1), and we considered the different scenarios of macroscopic offset in the main degrees of freedom.

The results show that, even if the optical couplings are not significantly affected by macroscopic offsets due to mismatches in the cavity lengths from the nominal design, the closed-loop couplings may change considerably.

Among the contributors to DARM noise from noises in the input laser beam, laser intensity noise and oscillator amplitude noise are the most important in a DC readout signal extraction scheme (see section 2.4.2). Our simulations showed that the couplings of laser intensity noise and oscillator amplitude noise to DARM are not dangerously affected by macroscopic length offsets in any of the cavities. The largest simulated changes occur for DARM macroscopic offsets: these affect particularly the cross couplings through CARM and SRCL's loops (figure 5.7). The worst case is when the DARM offset is such that the f2 sidebands are resonant in either of the arm cavities. The overall coupling (of both oscillator and laser noise) is dominated by cross-coupling through auxiliary degrees of freedom below the loops' bandwidth (typically $\lesssim$100 Hz). Generally, the coupling is mainly optical above the loops' UGF and it is not affected by cavity absolute length changes. The same trend is observed in both oscillator amplitude noise and laser intensity noise couplings. In fact fluctuations in sidebands amplitude are correlated with laser intensity fluctuations since phase modulation subtracts power from the carrier.

In ideal conditions, the f1 and f2 oscillator phase noises are of minor importance for DC readout. However, in the presence of CARM (or DARM) macroscopic offsets, such that the RF sidebands become nearly resonant in the arm cavities, their couplings increase by 2 orders of magnitude over the entire frequency range. The cross-coupling analysis attributes this increase to optical coupling caused by the phase picked up by the sideband in the non-antiresonant arms (figure 5.8).

Large changes in couplings of oscillator noise come also from offsets in the recycling cavities. In particular, we found the Schnupp asymmetry (i.e. MICH macroscopic offset) to be very important for the f1 oscillator phase noise. The main contribution to the coupling is optical, due to the phase accumulated by the RF sidebands in the arms. Below 100 Hz, cross coupling from the loops of the auxiliary DOFs dominate (Figure 5.9).

5.2.2 Feedforward path compensation

To limit the effect of the cross-couplings to DARM, the main loops include *feedforward* corrections. In particular these corrections are applied for MICH and PRCL. In the analysis presented in this section, the feedforward filters were not adjusted, while the noise couplings were calculated for different macroscopic offsets. This implies that in general the results showed here represent an estimate in excess of the actual couplings.

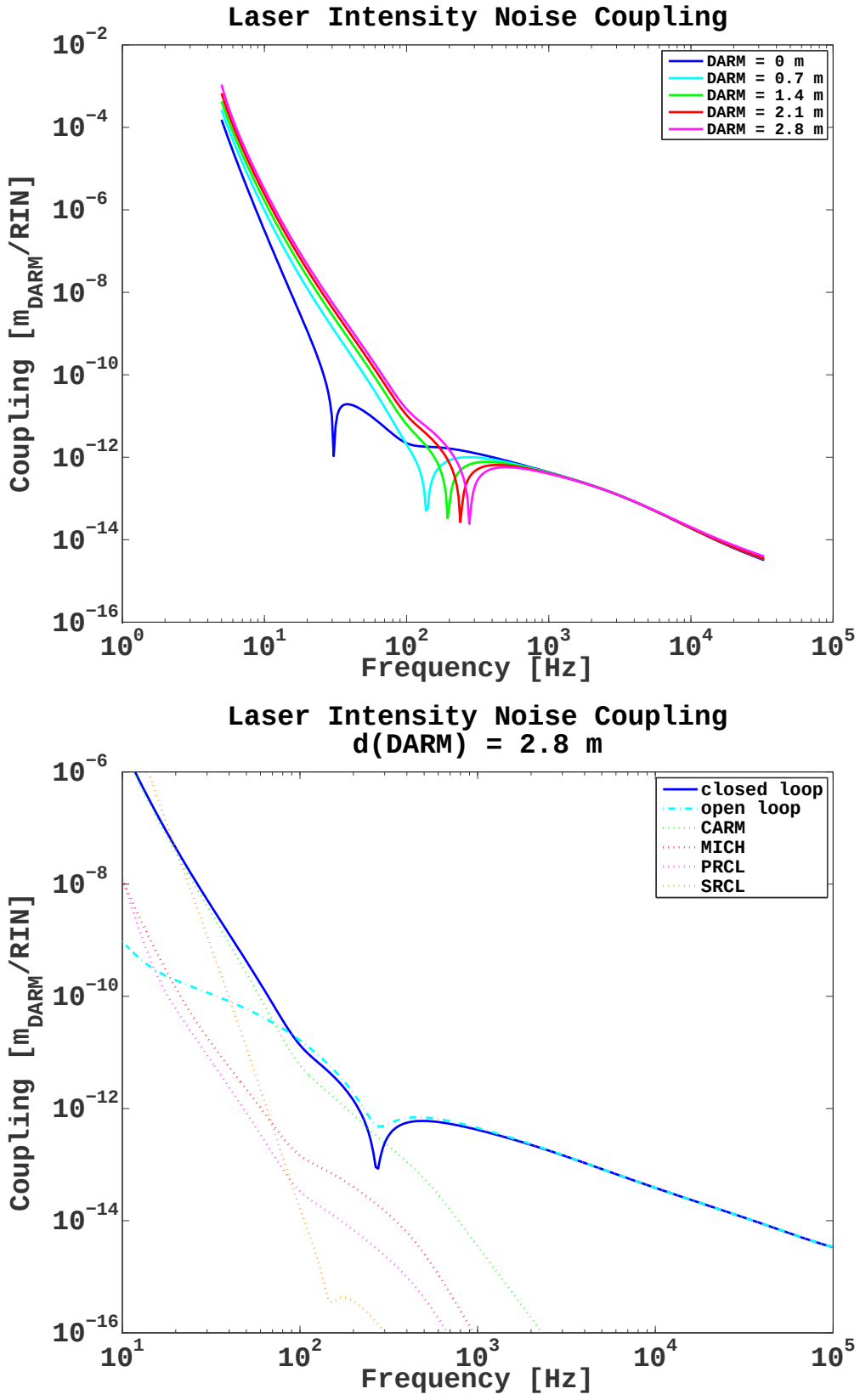

Figure 5.7: Laser intensity noise coupling increasing within the bandwith of the auxiliary loops for CARM and SRCL. Extreme case of f2 near resonance in both arm cavities budgeted on bottom plot.

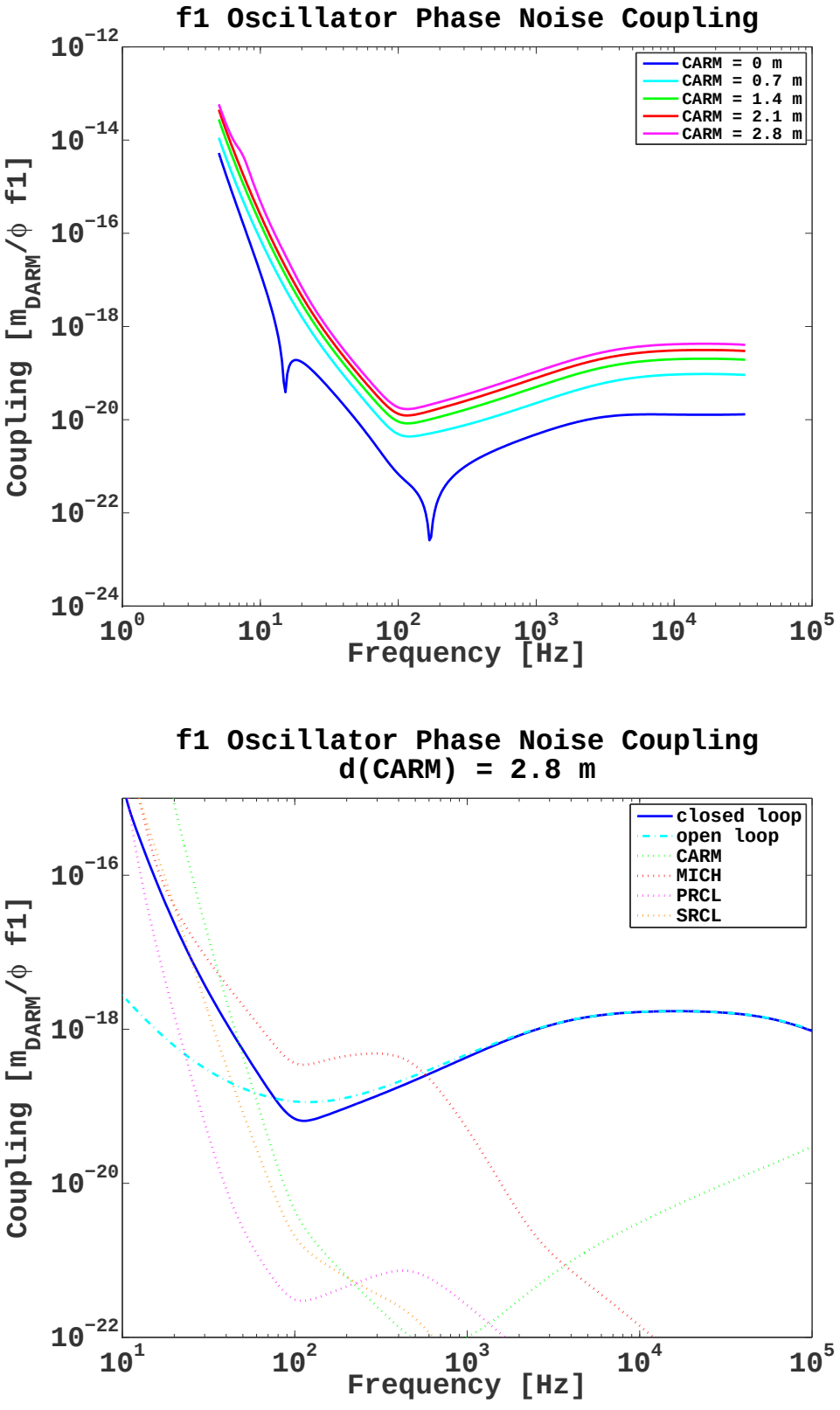

Figure 5.8: f1 oscillator phase noise coupling increases mainly because of a larger optical coupling caused by the phase gained by the sideband in the arms. The extreme case of f2 near resonance in both arms budgeted on bottom plot.

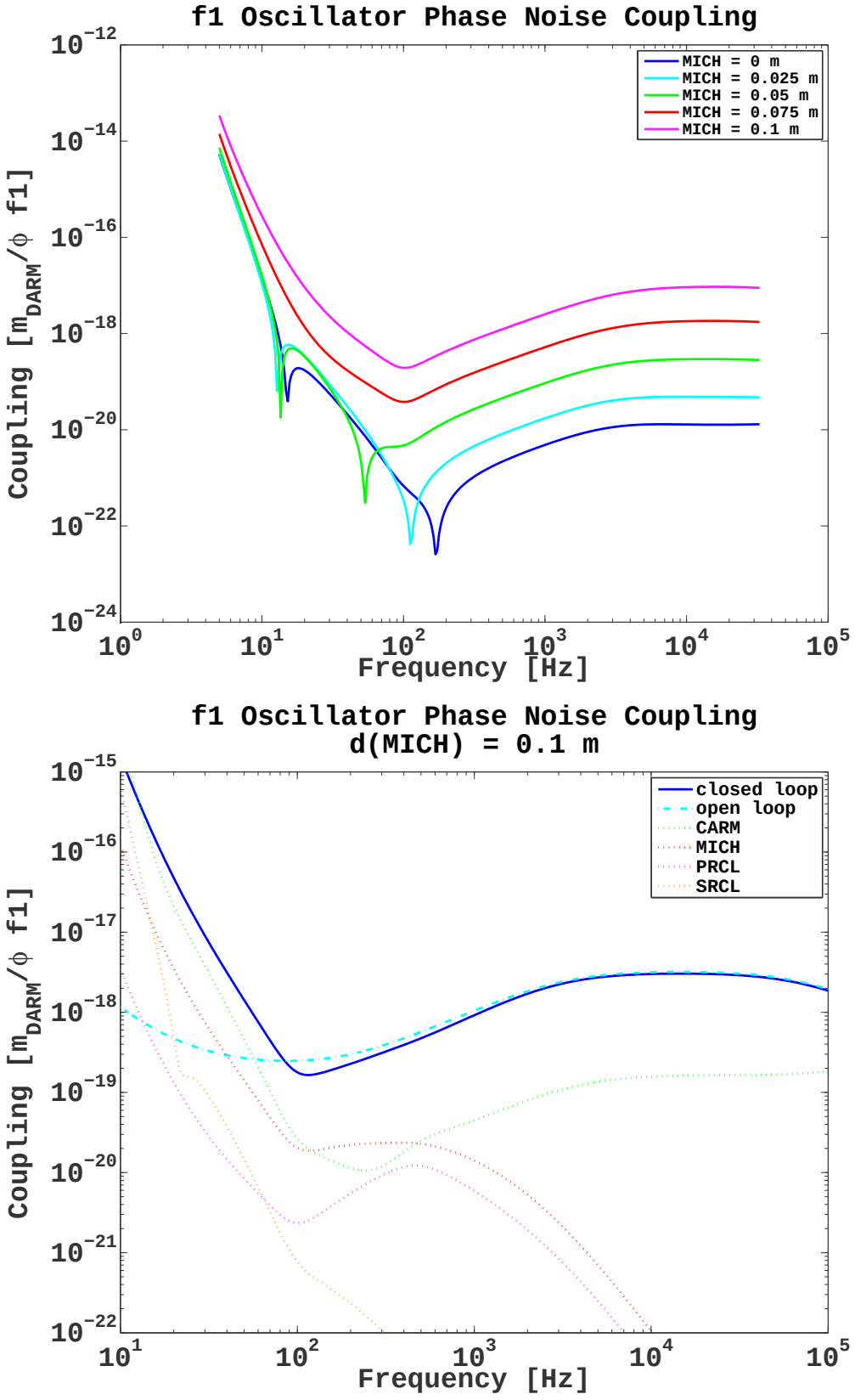

Figure 5.9: f1 oscillator phase noise coupling increases mainly because of a larger optical coupling caused by the phase gained by the sideband in the arms. Extreme case of f2 near resonance in both arms budgeted on bottom plot.

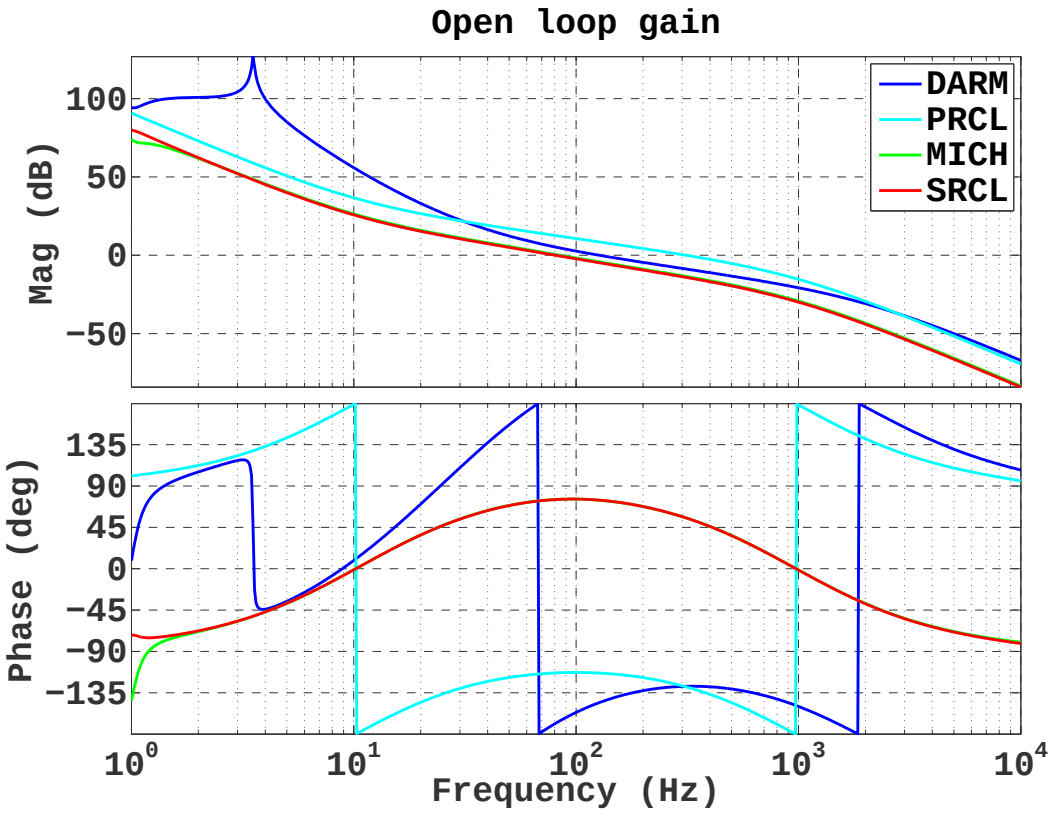

Figure 5.10: Open loop gain for the adjusted 40m configuration of table 4.3. These open loop gains were calculated by opening each loop alternatively, keeping all other loops closed.

5.3 Summary of results

The cavity length of the interferometer may be mismatched from their nominal values both at construction time and during commissioning time, as the static position of the optics table is adjusted. It is important to quantify the extent of this effect on the performance of the interferometer, in terms of controls and sensing noise. We studied the issue under different aspects and we included the effects of the control loops to obtain more realistic answers.

We found that laser and oscillator noise couplings do not change considerably for realistic macroscopic length offsets ($\sim$ cm) in the optical cavities. Large effects on the couplings occur only when any of the RF sidebands is close to resonance in the arm cavities. Experience at the 40m prototype shows that this scenario is possible.

Mismatches in the arm cavity lengths from the nominal design may prevent the fulfillment of the RSE resonant conditions. In particular, offsets in the recycling cavity lengths significantly affect the optical plant of the interferometer, to the point that the sensing matrix becomes hardly invertible. The control of the interferometer consequently becomes more difficult by cross-talk between the degrees of freedom. Moreover, a less stable plant allows more laser and oscillator noise to couple into the gravitational wave channel.

A highly undesirable consequence of having the arms less than 50 cm away from resonance is that the f2 sideband may have up to 10 times more power in one Michelson arm than the other. The same effect occurs for macroscopic offsets in the SRM position. Such an unwanted effect may seriously compromise the error signals obtained from the central part of the interferometer and thus the control of the cavities.

From a quantitative analysis of the error signals and the fields of the sidebands in the cavities, we conclude that the length of the arm cavities should be set at their ideal point with a precision of 1 cm or less; the recycling cavity length should be set within 1 millimeter; and finally the Schnupp asymmetry within one tenth of a millimeter.

The noise couplings to the dark port generally do not change in alarming ways for offsets on the order of centimeters on CARM, DARM, PRCL, SRCL. For MICH (the Schnupp asymmetry), just a few millimeters can have rather large effects on oscillator phase noise couplings.

However, even with very large macroscopic offsets (as in the 40m case), the overall DARM noise due to laser frequency noise (the main source of noise on the input beam) remains unchanged.

The present analysis considered only the laser fundamental modes. The contributions of higher order modes have not been taken into account. However their role might be crucial in determining the effects of mismatched cavity lengths on the overall performances of the interferometer [48].

Chapter 6

Measurement of Cavity Length and g-factor

In chapter 5 we discussed the implications of length mismatches in the optical cavities from their nominal value. In this chapter we introduce a technique developed at the Caltech 40m prototype interferometer [49] to measure absolute length and g-factor of the optical cavities. Measurements from the 40m arm cavities and power recycling cavity are presented.

6.1 Cavity Absolute Length

Being able to determine the absolute length of the optical cavities is essential for characterizing and diagnosing the performances of the interferometer. It is especially important during the interferometer's installation, when it is necessary to set the cavity within the allowed tolerances of the nominal design.

6.1.1 Measuring Cavity Absolute Length With Two Beating Lasers

Interferometric techniques have been developed with the purpose of measuring cavity length in gravitational wave detectors [50, 51, 52]. The precision of these methods typically increases with their complexity. At the 40m we developed a technique to measure the length of the arm cavities and the power recycling cavity without modifying the interferometer's configuration.

This technique uses an auxiliary laser beam to illuminate the interferometer from the dark port. The cavity to be measured is locked to the main PSL laser beam, which serves as the master laser in a phase-locked loop with the auxiliary laser (more in section 6.1.3). The frequency of the auxiliary laser is tuned until it resonates in the cavity appearing on transmission. There, it interferes with the main laser beam, also transmitted by the cavity, by beating at a frequency equal to the difference between the frequencies of the two lasers. As the frequency of the auxiliary laser is scanned, the beat amplitude follows a specific pattern determined by the cavity transmissivity as a function of laser frequency.

The measurement of transmitted power can then be used to fit an analytical model of the cavity transmissivity and thus to determine cavity parameters such as absolute length and g-factor (figure 6.1).

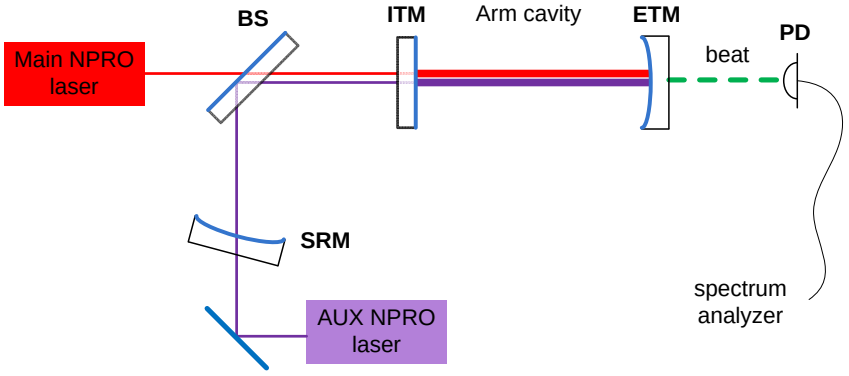

Figure 6.1: The two-laser technique applied to a simple Fabry-Perot cavity. The cavity is locked to the main laser by a PDH signal. An auxiliary laser is phase locked to the main laser, so that their relative frequency is held at a constant value set externally. When the relative frequency becomes an integer multiple of the free spectral range, the auxiliary beam resonates inside the cavity and is transmitted. At the transmission port the main laser and the auxiliary laser produce an amplitude modulated beam oscillating at the beat-note frequency.

The dark port was chosen for the injection of the auxiliary beam to have a sufficiently high beat power and thus to enhance the measurement SNR. Injecting from the power recycling mirror, although potentially convenient for the signal power, is not technically feasible without avoiding the mode cleaner.

6.1.2 The technique

When two coherent laser fields $\mathbf{E}_1 = E_1 \exp(i\omega_1 t)$ and $\mathbf{E}_2 = E_2 \exp(i\omega_2 t)$ interfere, the resulting field $\mathbf{E}$ has an amplitude

$$\begin{aligned} |\mathbf{E}|^2 &= (\mathbf{E}_1 + \mathbf{E}_2)\,(\mathbf{E}_1 + \mathbf{E}_2)^* \\ &= E_1^2 + E_2^2 + 2E_1E_2 \sin[(\omega_1 - \omega_2)t] \\ &= E_{dc} + E_{ac} \sin[(\omega_1 - \omega_2)t]. \end{aligned} \tag{6.1}$$

The latter term in 6.1 represents an amplitude modulated field at a frequency $\omega_m = \omega_1 - \omega_2$ measurable by a photodetector. When the cavity under test is locked for E_1, then E_{ac} provides a measurement of E_2 as it gets transmitted by the cavity.

In principle, if the cavity is phase-locked to the main PSL laser, the maximum precision of the measurement is determined by the RMS frequency noise of the main laser $\hat{\nu}_{rms}$ as it enters the cavity:

$$\frac{\delta L}{L} = \frac{\lambda}{c}\hat{\nu}_{rms}. \tag{6.2}$$

6.1.3 Phase Locked Lasers

To have a stable beat note as in 6.1, the relative frequency of the two lasers has to be held constant. This is not true with free running lasers, because of frequency fluctuations. A servo system is necessary to lock the two frequencies to each other. A Phase Locked Loop (PLL) [53] was used to lock the frequency of the auxiliary laser to the main laser at a relative frequency set externally by a local oscillator [54]. In this way, the absolute frequency of the system is still free to change, but the relative frequency is suppressed by the loop gain down to the limits of electronics noise.

The 40m PSL beam is obtained from a 1064 nm NPRO laser, then amplified by a LIGO Master Oscillator-Power Amplifier (MOPA) [25]. A second NPRO is the source of the auxiliary laser. Pick-off beams from each laser are used for the PLL setup as in figure 6.2.

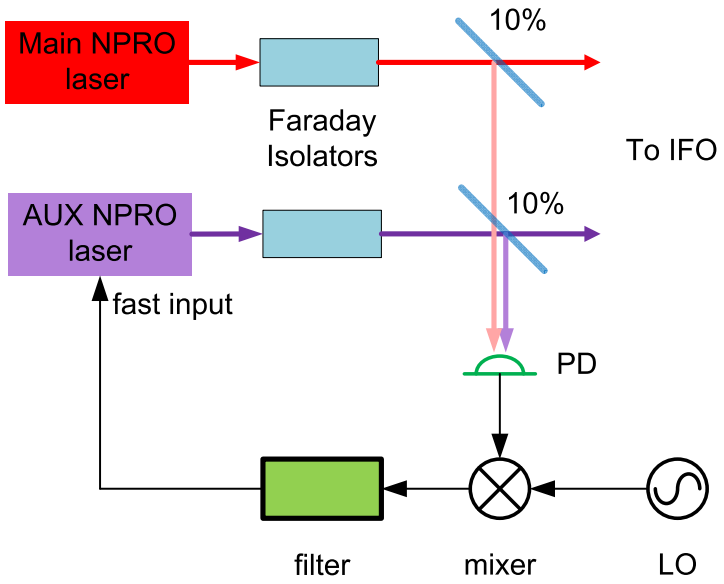

Figure 6.2: The relative frequency between the main PSL laser and the auxiliary laser is held constant by a PLL servo. A Marconi/IFR2023 frequency generator is used as a local oscillator with phase noise of 10^{-7} rad/$\sqrt{\text{Hz}}$ at 1 KHz.

Error Point

Referring to figure 6.3, the phases of the two laser fields can be written as:

$$\Phi_{PSL}(t) = \omega_0 t + \phi_0 + \gamma_0(t) \tag{6.3}$$

$$\Phi_{AUX}(t) = \omega_1 t + \phi_1 + \gamma_1(t) + \varphi_m(t) \tag{6.4}$$

where ω_0 and ω_1 are the frequencies of the main and the auxiliary lasers, respectively; ϕ_0 and ϕ_1 their phase offsets; $\gamma_0(t)$ and $\gamma_1(t)$ the phase fluctuations due to frequency noise; $\varphi_m(t)$ the contribution to the auxiliary field's phase due to frequency variations induced by the control signal.

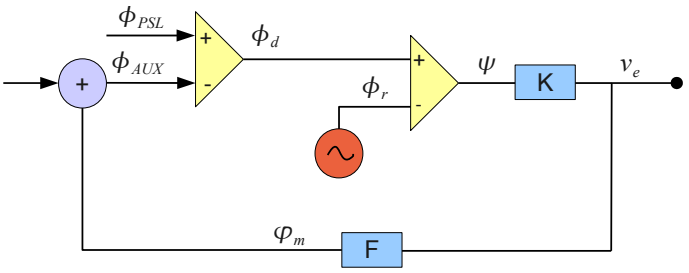

Figure 6.3: PLL diagram describing the phase along the loop.

The beat generated by the intereference of the two fields is measured on a photodiode. Here it produces a photocurrent with phase

$$\Phi_d(t) \equiv \Phi_1(t) - \Phi_0(t) = \omega_B t + \varphi_m(t) + \gamma_d(t) + \phi_d \tag{6.5}$$

where $\omega_B = \omega_1 - \omega_0$ is the beat frequency, $\gamma_d(t) = \gamma_1(t) - \gamma_0(t)$ the fluctuations and $\phi_d = \phi_1 - \phi_0$ the relative phase offset.

Next, the beat signal is mixed with that of a Local Oscillator (LO) with phase:

$$\Phi_{LO}(t) = \omega_{LO} t + \phi_{LO} \tag{6.6}$$

The product is low-pass filtered so that only the contribution of the differential phase survives:

$$\Psi(t) = \Phi_d(t) - \Phi_{LO}(t). \tag{6.7}$$

When the loop is closed and the PLL locked, $\omega_B = \omega_{LO}$ (see fig.6.4).

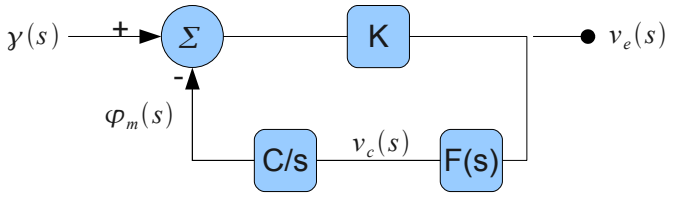

Figure 6.4: Diagram representing the phase loop in a locked state. $\gamma(t)$ is the combined Free Running Noise of the two lasers; $\varphi_m(t)$ is the contribution to the auxiliary laser phase from the servo; v_e is the loop's error signal; K the conversion factor from phase to voltage; F the servo filter; v_c the control signal; C the calibration function of the auxiliary laser that converts the control signal's voltage into the field's phase.

In the approximation of small random frequency fluctuations and thus of small control signal ($[\gamma_d(t) + \varphi_m(t)] \ll 1$), the error point v_{err} is proportional to the relative phase between the beat and the local oscillator:

$$v_e(t) = K \sin[\Psi(t)] \approx K\,[\gamma_d(t) + \varphi_m(t)] \tag{6.8}$$

where K is the PLL proportionality coefficient between differential phase and the error signal amplitude. K is proportional to the beat, LO amplitude and mixer efficiency coef-

ficient.

The loop is closed through a compensation filter $F(t)$ and the phase of the control signal is:

$$\dot{\varphi}_m(t) = C\,[v_e(t) * F(t)] \tag{6.9}$$

where C represents the calibration of the auxiliary laser that converts input voltage ($V_e * F$) into the frequency of the light ($\dot{\varphi}_m$). For the NPRO of our experiment and within the bandwidth of our PLL, C is assumed to be frequency independent: $C(t) = C$.

Replacing $\varphi_m(t)$ from (6.8) into (6.9) and switching to Laplace domain, the error signal $\hat{v}_e(s)$ is obtained as a function of the Free Running Noise $\hat{\gamma}(s)$:

$$\hat{v}_e(s) = \frac{K}{1 - KC\hat{F}(s)/s}\,\hat{\gamma}(s). \tag{6.10}$$

One can then obtain the phase noise γ from the spectrum of the error point by compensating this for the loop gain, and dividing it for the calibration. In turn, the calibration can be obtained by measuring the peak amplitude of the beat note at the error point, when the PLL is not locked.

Open Loop Gain

From Figure 6.3, the Open Loop Gain (OLG) is

$$G_{OL} = \frac{KC\hat{F}(s)}{s}. \tag{6.11}$$

Loop Filter

Two parameters define the PLL performance [53]:

- Hold-in Range: the largest frequency step $\Delta\omega_H$ tolerated by a locked PLL before lock breaks, as given by:

  $$\Delta\omega_H = \pm\kappa_\nu \tag{6.12}$$

  where $\kappa_\nu = KCF(0)$ is the DC gain of the loop.

- Lock-in Range: the maximum initial frequency step $\Delta\omega_L$ between ω_1 and ω_2 that the PLL can overcome to acquire lock:

  $$\Delta\omega_L \simeq \pm\kappa_L : \tag{6.13}$$

  with $\kappa_L = KCF(\infty)$ the loop gain limit at infinite frequency.

To scan the frequency range quickly enough to avoid low frequency fluctuations of the transmitted power induced by fluctuations in mirror alignment, the PLL must have good

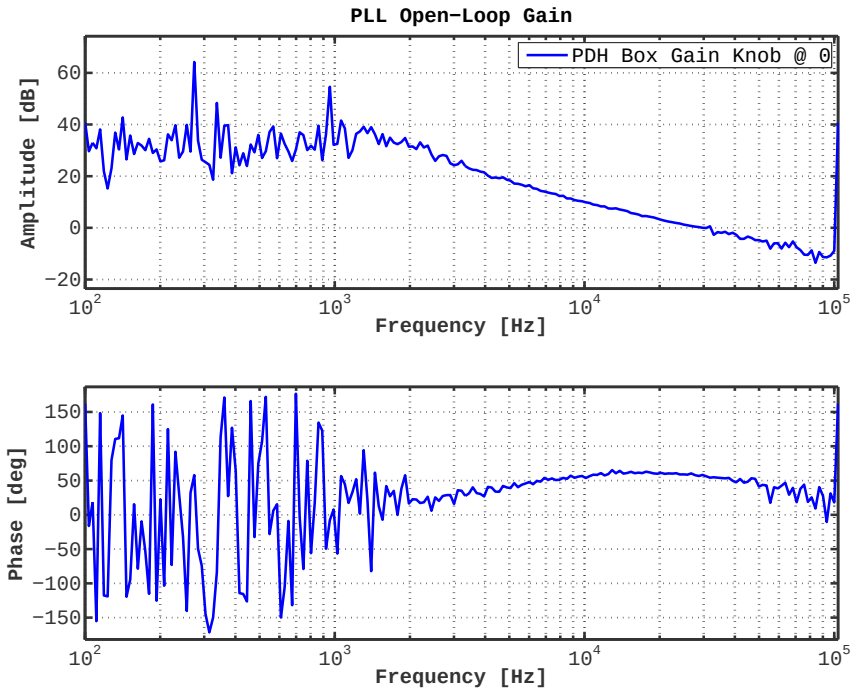

Figure 6.5: Open Loop Gain of the PLL. The UGF is at about 30 KHz.

tracking performance, and thus a large hold-in range. To sweep a large frequency range (for instance a few hundreds of MHz, as with the PRC case) it is necessary that the PLL can tolerate frequency steps of about 100-500 KHz at a time, thus the PLL has to have also a good lock-in range.

We used a second order loop filter shaped as

$$F(s) = \alpha \frac{s - s_0}{s - s_p} \tag{6.14}$$

with gain $\alpha \simeq 3 \times 10^{-2}$, s_0 a zero at about 5 KHz, and s_p a pole at about 5 Hz (Figure 6.6). The spectrum density of the phase error signal of the loop is shown in figure 6.7.

6.1.4 Experimental Setup

Figure 6.9 shows a representation of the PLL implemented to measure absolute length of arm cavities and power recycling cavity. Broadband InGaAs photodiodes (1 GHz) are used both at the PLL and at the transmission port to detect the beat between the lasers (1-100 MHz). A computer script sweeps the auxiliary laser frequency by driving the PLL's local oscillator via a GPIB interface. The same script also measures the cavity transmitted power through a power spectrum analyzer centered at the PLL frequency. The transmission profile is recorded and then fit with an analytical model.

The cavity under test is held locked by a standard PDH error signal: POX and POY, the demodulated signals at f1[1] obtained from photodetectors measuring ITM pickoff

[1] $f1 = 33$ MHz in the 2004-2009 configuration of the 40m on which the measurement was done.

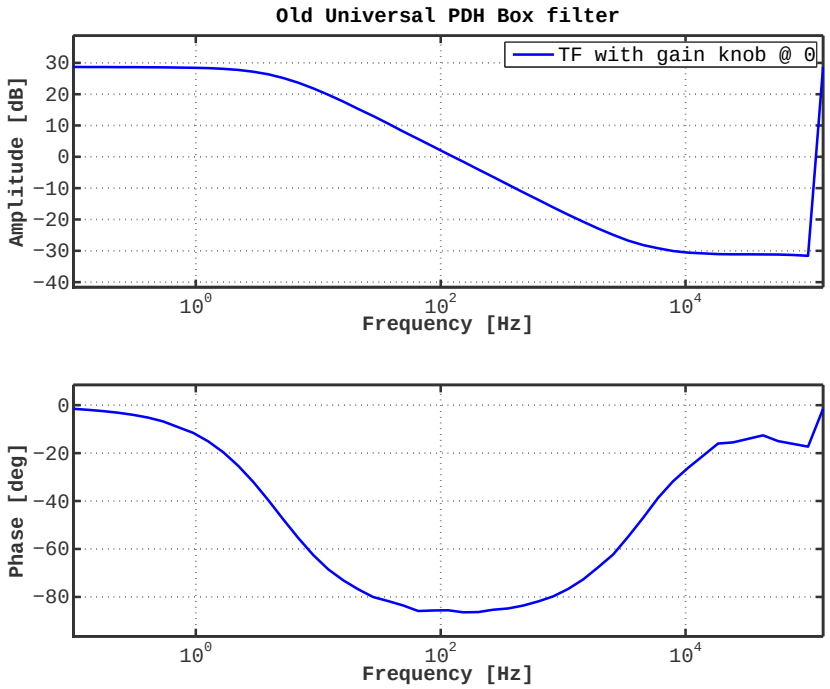

Figure 6.6: PLL passive lag-lead filter. Gain of 3×10^{-2}, pole at 5 Hz, zero at 5 KHz.

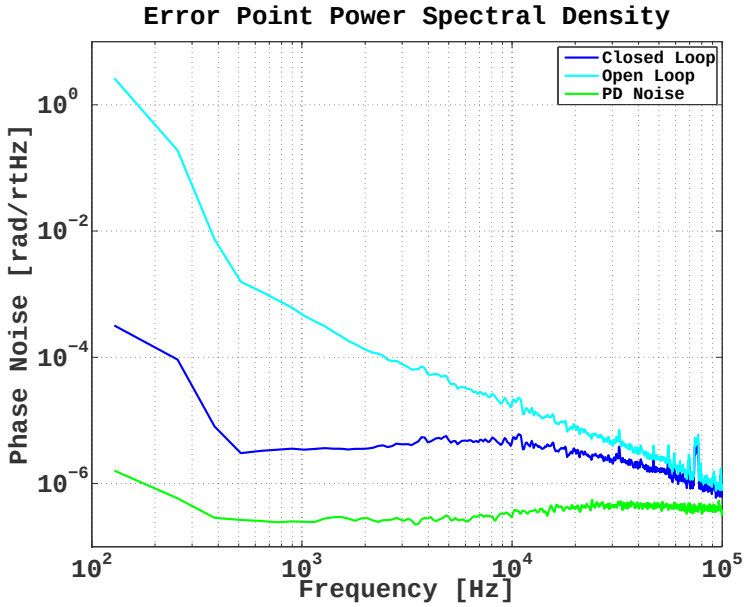

Figure 6.7: PLL error point spectrum density. The UGF is at about 30KHz.

beams, are used to lock the X and Y arm cavities, respectively; REFL33I, a demodulated signal at f1 from the bright port of the interferometer, is used to lock the power recycling cavity.

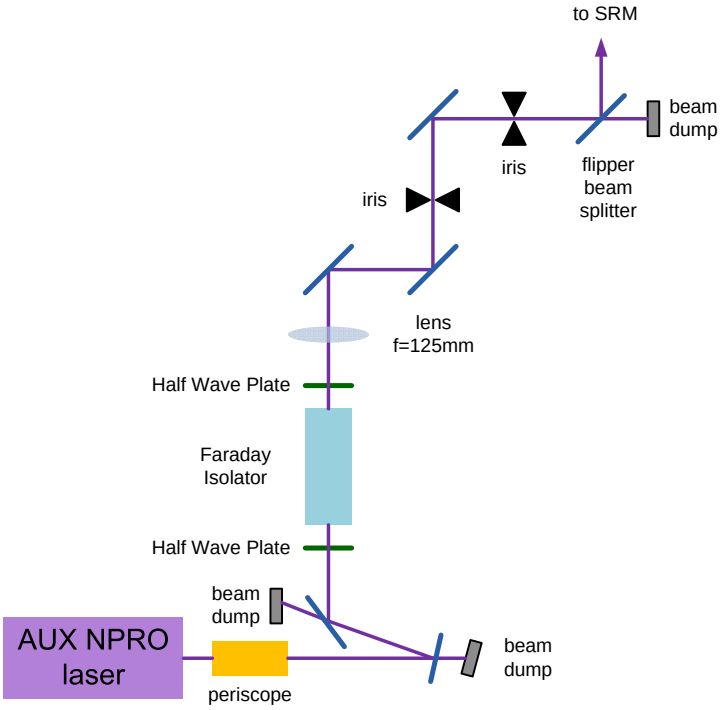

Figure 6.8: Auxiliary laser injection optical setup at the dark port: a Faraday isolator is used to shield the laser from back-reflected light; a converging lens is used for mode-matching; irises ensure beam alignment.

6.2 Arm Cavity Length Measurement

The 40m arms are Fabry-Perot cavities with high finesse. Their transmissivity versus frequency has a profile made of peaks in correspondence with the resonances. By measuring the free spectral range from the distance between these resonances it is possible to obtain the absolute length of the cavity.

To explore the cavity transmissivity profile, the PLL's local oscillator frequency is swept by several MHz, thus passing through a few cavity resonances. The resonant frequencies f_0 are determined by a fit of each resonance with a Lorentzian function as the following:

$$P(f) = \frac{1}{\sqrt{1 + \left(\frac{f - f_0}{f_0}\right)^2}} + c \tag{6.15}$$

A linear fit of the resonant frequencies, measured both below and above the main laser frequency, then provides an estimate of the cavity free spectral range (figure 6.10).

With this method, the cavity absolute length was measured with an absolute precision

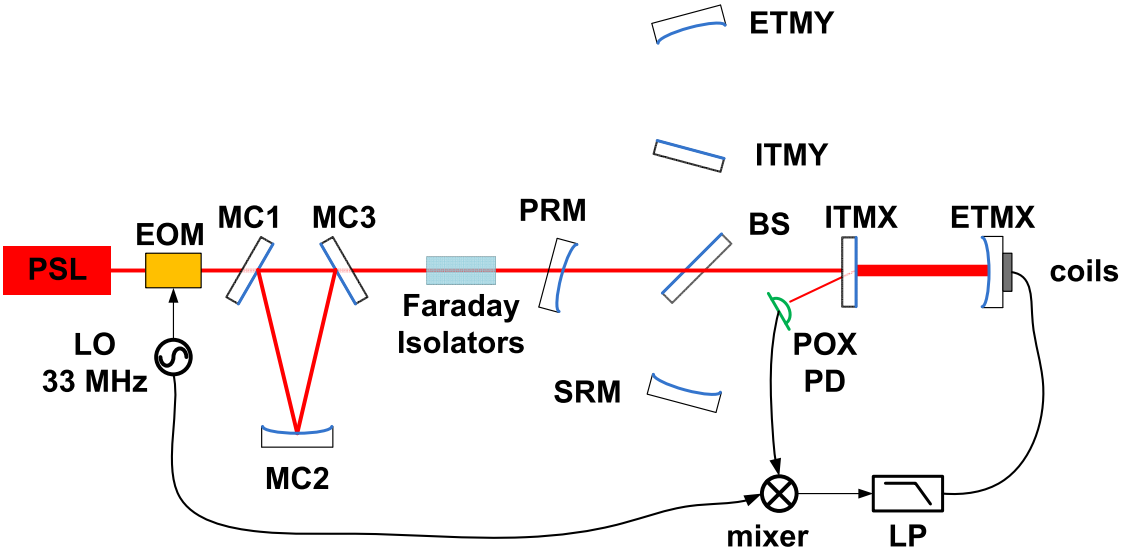

Figure 6.9: Interferometer configuration for arm length measurement. Only the arm cavity under test is aligned and locked to the main laser's carrier.

of $50\mu m$, and a relative precision of 10^{-6}. The results are summarized in table 6.1 and values agree with a previous measurement based on a Vernier technique [55].

6.3 Arm cavity g-Factor Measurement

The g-factor is essential to characterize the cavity response to laser higher order modes (HOM). In ideal conditions only the fundamental mode is allowed to circulate in the interferometer, since any high order spatial mode can affect the interferometer performances in an undesirable way: i.e. interfering with the lock acquisition process or increasing the amount of "junk" light at the dark port [48]. Knowing the g-factor, it is possible to "map" the surroundings of cavity locking points and localize the distribution of the HOM resonances.

An analysis of the arm cavity resonance profiles for high order modes was done at the 40m with the measured g-factor. This allowed us to exclude higher order modes as a cause of difficulties in locking the interferometer in some particular configuration [21].

6.3.1 The Principle

A variation of the technique used to measure absolute length can be used to measure the g-factor of the arm cavities. As explained in section 4.2, because of the Guoy phase [17], the laser higher order modes resonate in a Fabry-Perot cavity at different frequencies than the fundamental mode. The distance in frequency between two consecutive and degenerate higher order modes TEM_{lmn} and $\mathrm{TEM}_{l,m+1,n}$ is equal to the cavity *Transverse*

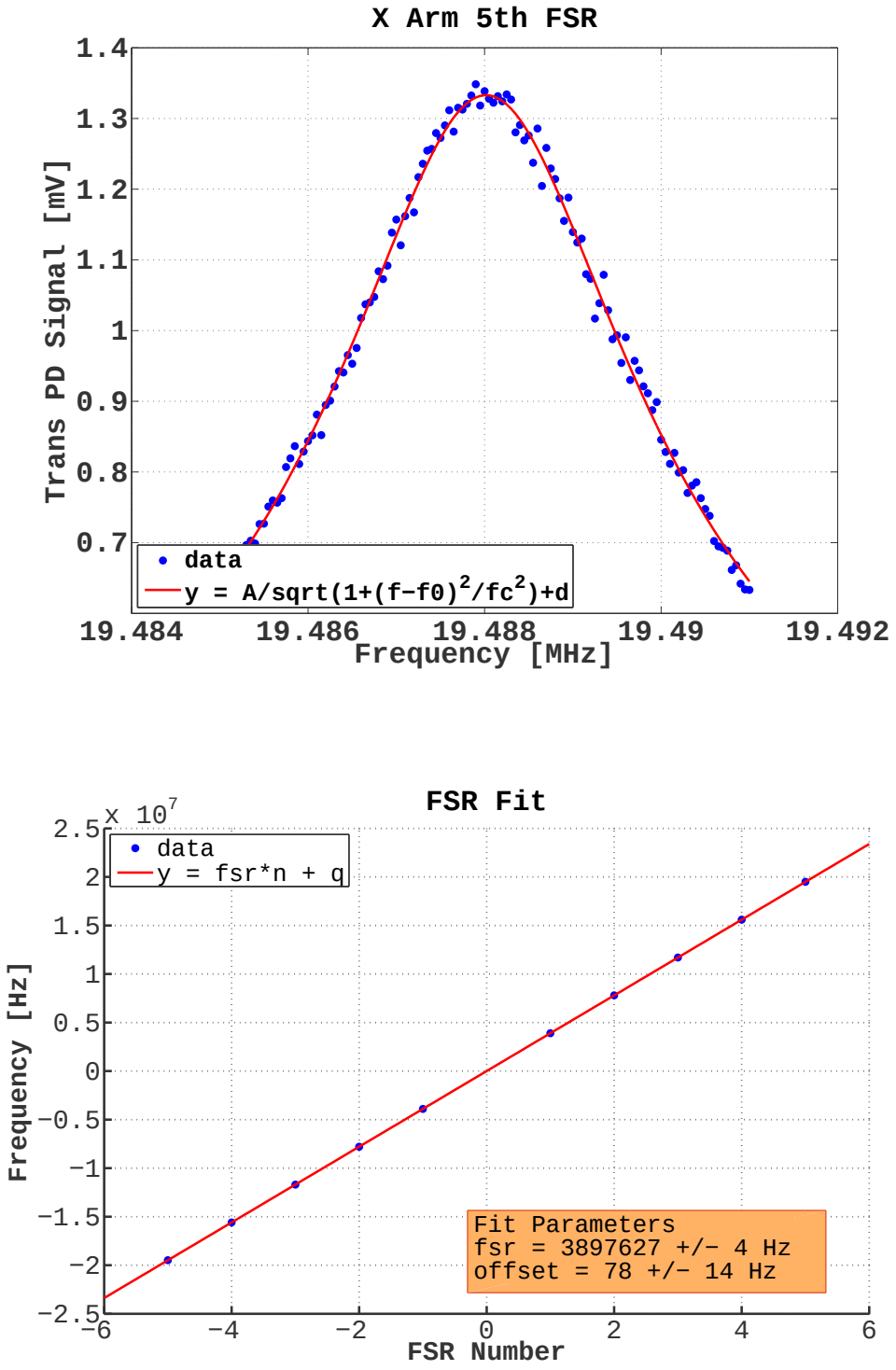

Figure 6.10: Top: X arm transmitted power in correspondence with a cavity resonance peak. The x-axis is the relative frequency between the two lasers, as set by the PLL. To obtain the resonance parameters, the data is fit with a Lorentzian function centered at the resonant frequency (eq. 6.15). Bottom: linear fit of 10 resonance measurements used to determine the cavity FSR. A small offset of unknown origin is present in the measurement. It seems to be an actual offset of the resonant frequency rather than a measurement artifact, since it persists when sweeping the frequencies forward or backward.

Mode Spacing (TMS):

$$TMS = FSR \times \frac{1}{\pi} \cos^{-1}(\pm\sqrt{g}) \tag{6.16}$$

where FSR is the free spectral range relative to longitudinal modes, and g is the g-factor.

The two-laser technique can measure the TMS from the interference between a higher order mode and the fundamental one. The HOM of one beam beats with the fundamental mode of the other and the g-factor is obtained by comparing the beat frequency with the TMS (as in equation 6.16).

Measurement of Transverse Mode Spacing

The beat between the TEM_{00} mode and the TEM_{01} (or TEM_{10}) mode can be detected in two ways:

1. the arm cavity is locked to the TEM_{00} of the main laser and the auxiliary laser's frequency is tuned at one TMS away from the main laser;

2. the arm cavity is locked to the TEM_{01} of the main laser, and the auxiliary laser is tuned to the arm's FSR.

In the first case, at the transmission, the TEM_{00} beats with the TEM_{01} of the auxiliary laser.Vice versa, in the second case the TEM_{01} of the main beam beats with the TEM_{00} of the auxiliary laser. In both cases, the beat note would appear at the TMS frequency. The arm cavities of the 40m were measured in both ways. In any case, the TEM_{01} (or TEM_{10}) is enhanced by inducing a slight misalignment in the cavity by tilting either the ETM or the ITM: a tilt in pitch to enhance the TEM_{10} mode, in yaw for TEM_{01}.

In the first measurement method (i.e. arm cavity locked to the TEM_{00} of the main laser), the fields E_1 and E_2 of the main and the auxiliary laser, respectively, at the cavity output can be written by expanding them up to the first higher order mode:

$$E_1 = \sqrt{P_1}\, e^{i\omega_1 t} |00\rangle \tag{6.17}$$

$$E_2 = \sqrt{\alpha P_2}\, e^{i\omega_2 t} |00\rangle + \sqrt{(1-\alpha)\, P_2}\, e^{i\omega_2 t} |01\rangle\,. \tag{6.18}$$

where the quantities in kets represent the Hermite-Gaussian basis states and α is a coefficient representing the fraction of the total power in the specific mode. The TEM_{01} of the main laser is not considered because the TEM_{00} is largely dominant. As ω_2 is scanned, α changes, giving more power to one mode or the other as the frequency equals an integer multiple of the free spectral range or of the transverse mode spacing. Following 6.17, the power at the transmission photodiode can be written as:

$$(E_1 + E_2)\,(E_1 + E_2)^* = P_1 + P_2 + \tag{6.19}$$

$$2\sqrt{\alpha P_1 P_2}\, e^{i(\omega_1-\omega_2)t} + \tag{6.20}$$

$$2\sqrt{(1-\alpha) P_1 P_2}\, e^{i(\omega_1-\omega_2)t} \langle 01|00\rangle \tag{6.21}$$

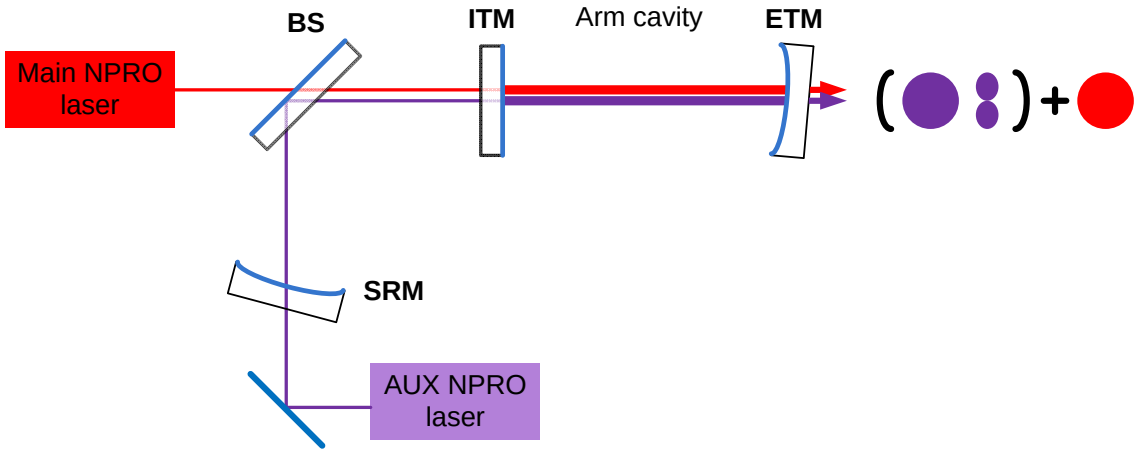

Figure 6.11: Arm cavity setup for g-factor measurement. The cavity is slightly misaligned in pitch or yaw, depending whether the TEM_{01} or TEM_{10} has to be measured.

where the first term is at DC, and the following two terms give rise to an amplitude modulation at the beat note frequency $(\omega_2 - \omega_1)$. Scanning ω_2 until it becomes a frequency multiple of the FSR, α tends to 1 and a beat is detected between the two fundamental modes. Further tuning ω_2 until it approaches the TMS frequency, α tends to zero and a beat note appears at the transmission.

This beat is not detectable by a simple photodiode. In fact the dot product between $|00\rangle$ and $|01\rangle$ is zero in general, due to the phase profile of the TEM_{01} wave front (Figure 6.12). In principle the beat cannot be detected by a photodiode perfectly centered on the

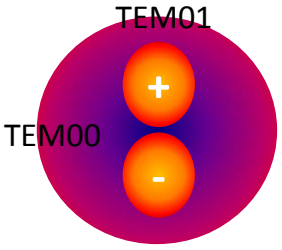

Figure 6.12: TEM_{01} mode phase profile. Because of the opposite phase between the two lobes, the interference with the wave front of a TEM_{00} mode has zero amplitude.

beam axis and orthogonal to the wave front. In reality the symmetry of the field on the xy plane is easily broken as soon as the signal is detected by a photodiode. However, to enhance the signal the beam is partially blocked by a razor blade placed in proximity to the photodetector.

6.3.2 Results

The measurement of the 40m arm cavity is done by first misaligning the cavity in pitch, then in yaw, detecting the resonance of TEM_{01}, and then of TEM_{10} respectively. The two resonances are found at two different frequencies, separated by 19 kHz in the Y arm, and

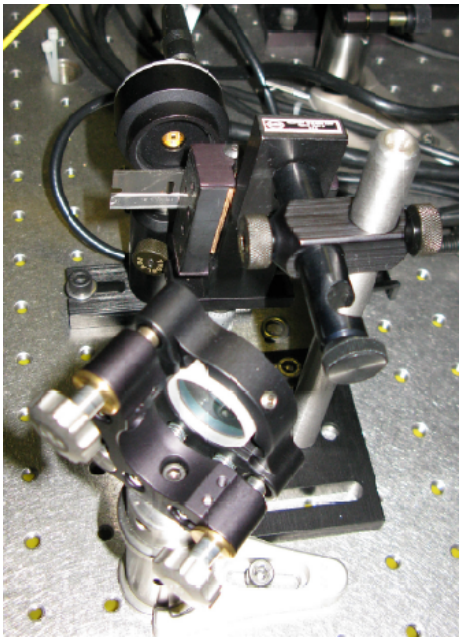

Figure 6.13: To detect the beat between the TEM_{01} and TEM_{00}, the symmetry of the wave front profile is broken by blocking part of the beam spot with a razor blade. The blade is placed as close as possible to the photodiode, to avoid diffraction fringes. The position of the blade is tuned with a micrometer screw.

15 kHz in the X arms. The difference between the horizontal and the vertical modes is due to the astigmatisms of the end mirrors. From the split in frequency it is possible to estimate the difference between the radii of curvature in the two directions of the mirrors. By separating the expressions for the x and y g-factors, the transverse mode spacing is written as

$$TMS_{01} = \frac{c}{2\pi L}\cos^{-1}\sqrt{1-\frac{L}{R_V}} \tag{6.22}$$

$$TMS_{10} = \frac{c}{2\pi L}\cos^{-1}\sqrt{1-\frac{L}{R_H}} \tag{6.23}$$

where R_H and R_V are the radii of curvature of the end mirror along the horizontal and the vertical direction, respectively.

Measurements of transmitted power versus beat frequency for the X arm are shown in figure 6.14 and a summary of g-factor measurements is in table 6.1.

The calculated values for the radii of curvature of the end mirrors agree within 2% with the design specs of the optics[2].

Application of measurement results

Using the absolute length and the g-factor measurements, it is possible to model the resonance profile of the HOMs in the arm cavity. Simulations excluded the presence of

[2]Astigmatism is not specified. Reliable measurements of the optics phase maps are not available for comparison. The phase maps measured at the installation time were affected by a systematic error [56].

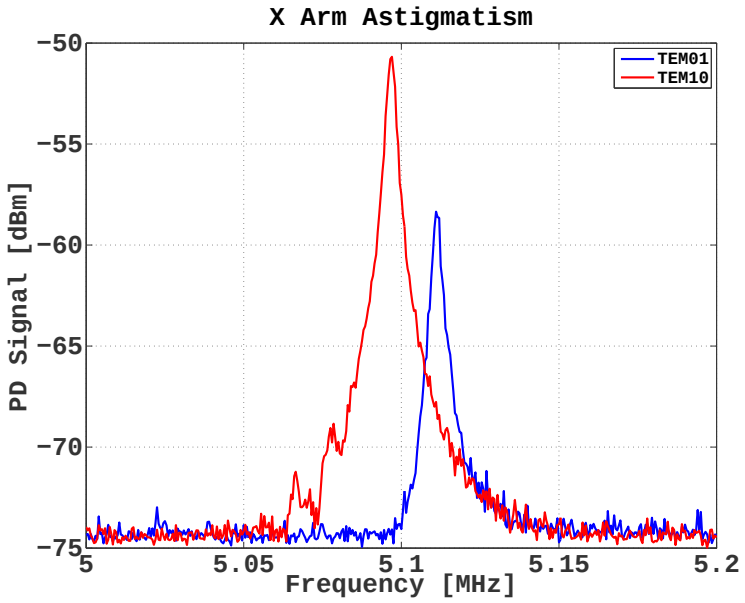

Figure 6.14: Transmitted power from X arm from cavity misalignment in pitch (blue curve) or yaw (red curve) versus beat frequency between the two lasers. The separation between the resonance frequencies of TEM_{01} and TEM_{10} is the effect of the end mirrors' astigmatism.

any of the first (and larger) HOMs within the cavity linewidth (figure 6.15).

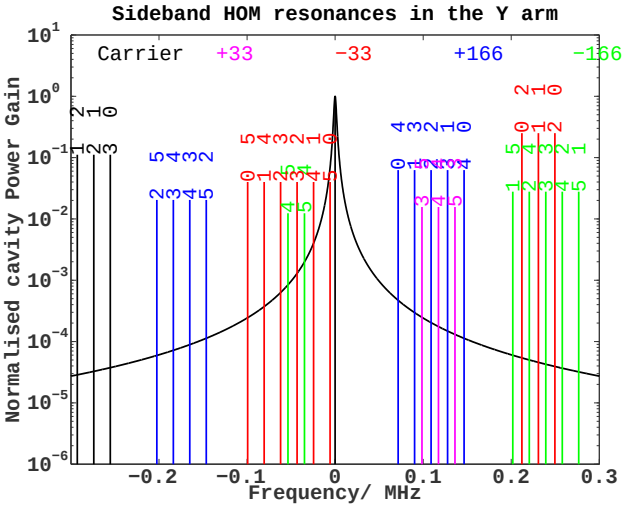

Figure 6.15: Reconstruction of resonance distribution of HOM around the carrier line, for the measured values of arm absolute length and g-factor (Plot obtained with Matlab code courtesy of John Miller).

6.4 Power Recycling Cavity Length Measurement

It is also possible to measure the resonance profile of the power recycling cavity in a way similar to that used for the arm absolute length measurement. In this case the auxiliary

beam still enters the cavity from the SRM, but the transmitted power is measured at the bright port of the interferometer (REFL signal) -figure 6.16. The arm cavities and the signal are excluded by holding them misaligned. Because of the complex reflectivity of the Michelson compound mirror, the power recycling cavity gain has a less simple dependence on frequency than the arm's Fabry-Perot: the resonance finesse is frequency dependent, and the cavity response is different depending on whether it is locked to the main beam carrier or to the sidebands.

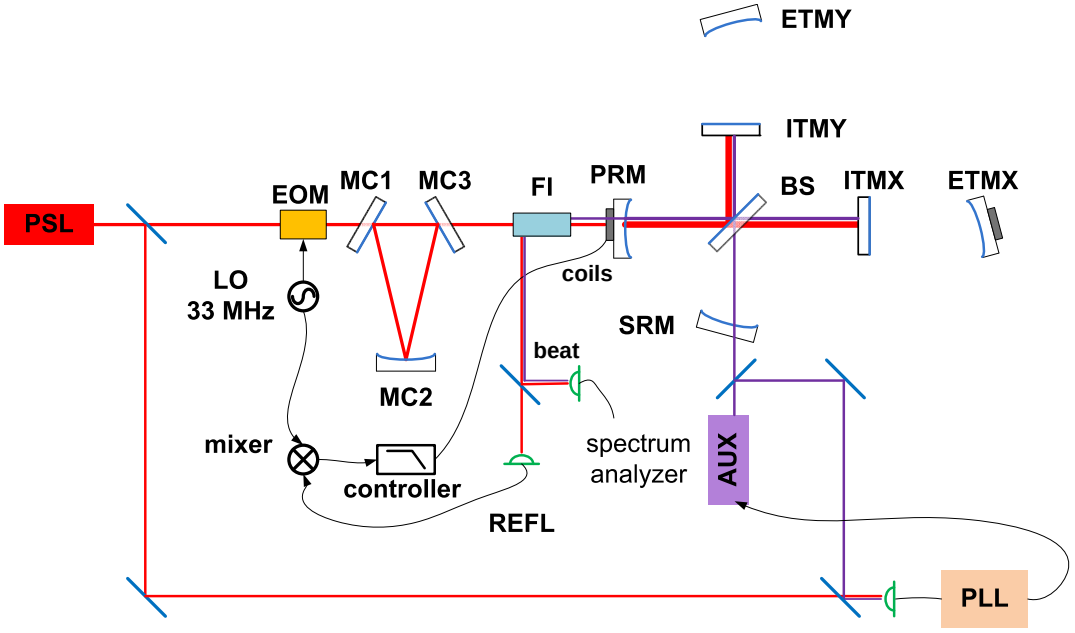

Figure 6.16: IFO configuration PRC length measurement. The cavity is locked to the carrier, and the rest of the interferometer is misaligned.

Referring to figure 6.16, the transmitted field E_t at the REFL port as a function of the beat frequency $\omega_B = (\omega_{psl} - \omega_{aux})$ is given by:

$$E_t = \frac{-t_{prm} r_{itm} e^{i2\omega_B l_{prc}/c} \sin\left(\frac{\omega_B l_{asy}}{c}\right)}{1 + r_{prm} r_{itm} e^{i2\omega_B l_{prc}/c} \cos\left(\frac{\omega_B l_{asy}}{c}\right)} \tag{6.24}$$

where t_{prm} is the PRM transmittance; r_{itm} the ITM reflectance; l_{asy} the length of the Schnupp asymmetry; and l_{prc} the length of the power recycling cavity ($l_{prc} = l_{prm-bs} + (l_x + l_y)/2$.

The measurement results are in good agreement with the analytical model in 6.24 (figure 6.17). Part of the residuals are attributed to the fact that the cavity alignment is not perfectly constant for the entire duration of the measurement and thus the circulating power changes during the course of the experiment.

This measurement has provided an estimation of the cavity length to (2.224 ± 0.005) m and of the Schnupp asymmetry to (0.457 ± 0.005) m, in which the 5 mm error is obtained by a non-linear least square statistical fit. Since the actual PRC length is not known, the

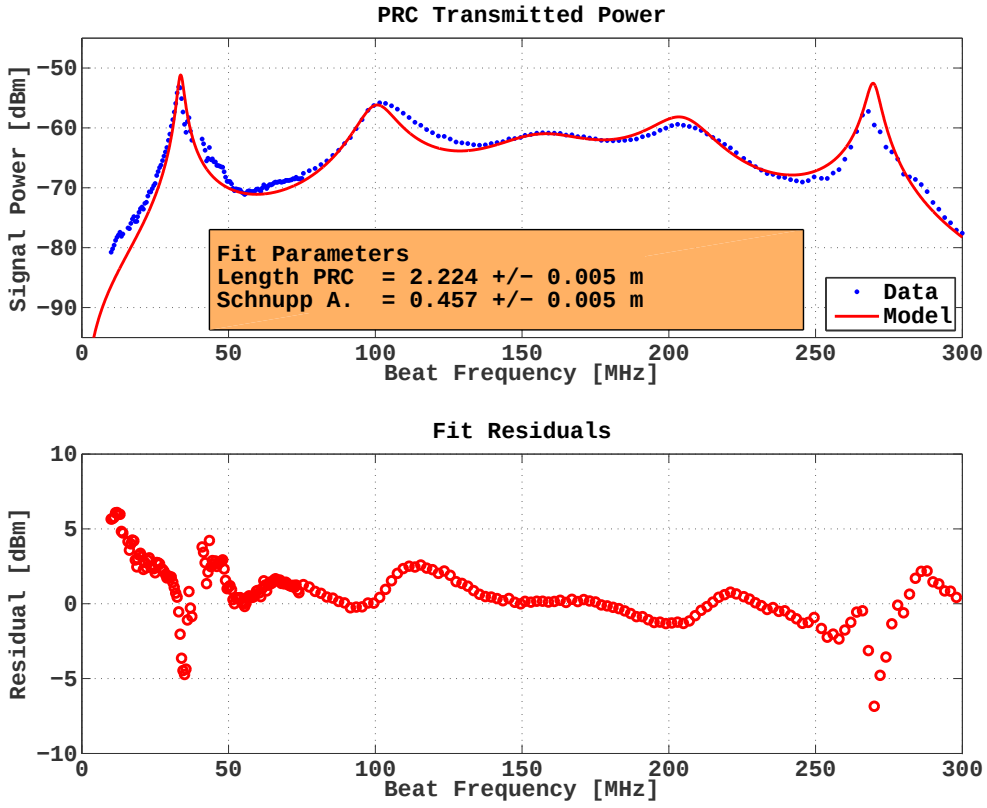

Figure 6.17: PRC frequency scan. Power measured at the interferometer bright port (REFL). Low frequency alignment fluctuations of the cavity during the course of the measurement limit the precision of the fit with the analytical model.

measurement can only be compared with the design value of 2.257m; the measurement of the Schnupp asymmetry compares well with previous independent measurements that set it at 0.451m.

The electronics used for the PRC measurement, although precise enough for the arm cavity length, require further improvements to achieve the sub-millimeter resolution desirable for the recycling cavity lengths. The duration of the measurement is limited by the hold-in range of the PLL, which, in its current version, does not allow for faster frequency scans[3]. A better performing PLL, with a filter modified for larger hold-in and lock-in ranges, would likely shorten the same measurement procedure to less than one minute, thus avoiding low frequency alignment drifts of the cavity. Also, the duration of the length measurement of the power recycling cavity would be shorter for longer recycling cavities like the ones planned for the 2010 40m Upgrade or Advanced LIGO (∼55m).

[3]The 300 MHz scan in Figure 6.17 requires about 10-15 minutes.

6.5 Signal Recycling Cavity Length Measurement

Similar to the power recycling cavity, the technique could be applied to the signal recycling cavity. The results would be extremely interesting since the RSE signal extraction scheme and the response of the full interferometer to the sidebands strongly depend on the absolute length of the signal recycling cavity. The SRC has not been measured yet, but its measurement has been planned for the 40m Upgrade. The interferometer will be set such that the entire dual recycled Michelson will be locked, with the injection still at the dark port and the transmission readout at the interferometer's reflection port.

6.6 Summary of results

An effective technique to measure cavity absolute length and g-factor was developed and tested at the Caltech 40m prototype interferometer. It proved that the arm cavity length can be measured with a precision of 10^{-6}, and the g-factor can be measured with 10^{-4} precision. That also provides a measurement of the end mirrors curvature with a precision of 10^{-4}, which is enough to resolve optics astigmatism capable of breaking the degeneracy of TEM_{01} and TEM_{10}.

The measurement is of immediate utility to verify the compliance of the cavities with their nominal optical design. Also, because of its simplicity and because it does not require modifications of the interferometer configuration, the technique is able to provide measurements of the interferometer in science mode. Such information allows us to promptly know the resonance profile of the cavities in the vicinity of their working point, or possible changes in mirror radius of curvature which may cause thermal lensing effects [57].

A summary of the measurements on the 40m interferometer as in its 2004-2009 configurations given in table 6.1.

Parameter	Value
ROC_{H-X}	55.8957 ± 0.0045m
ROC_{V-X}	56.7937 ± 0.0038m
ROC_{H-Y}	56.1620 ± 0.0013m
ROC_{V-Y}	57.3395 ± 0.0011m
L_X	38.4583 ± 0.00005m
L_Y	38.6462 ± 0.0003m
PRCL	2.224 ± 0.005m
Schnupp asy	0.457 ± 0.005m

Table 6.1: Summary of cavity parameters measurements

Conclusions

The first generation of gravitational wave interferometers has successfully concluded its task of collecting science data for several years at the design sensitivity. The next generation of interferometers will focus on increasing the event detection rate. The forthcoming challenge will be to ensure the detectors achieve the design performances, limited only by the fundamental noise sources.

In this thesis we performed a quantitative analysis to define adequate margins of precision for setting cavity lengths according to the optical design. To this end, we studied the effects of macroscopic offsets in the optical cavity lengths with three main objectives:

- predicting the changes in our ability to decouple the degrees of freedom and thus of applying an effective control scheme in the presence of length mismatches
- understanding noise coupling paths from common mode noise into the GW channel in the presence of macroscopic length offsets
- developing a cavity length measurement technique to characterize the optical layout and diagnose the interferometer performance.

We found that it is essential that the RF sidebands are nearly anti-resonant in the arm cavities. When this is not the case, and the sidebands gain phase upon reflection from the ITMs, the Pound-Drever-Hall error signals used to control the interferometer's degrees of freedom are altered. Also, asymmetries between the sidebands fields arise in the two Michelson arms and may compromise our ability to lock the recycling cavities. In these circumstances, adjustments are necessary to the lengths of the recycling cavities. The canonical Resonant Sideband Extraction requirements are no longer satisfied and numerical simulations are necessary to determine appropriate cavity length adjustments. These allow us to recover the interferometer sensitivity to differential arm length displacement.

We studied the role of macroscopic offsets on couplings of noise in the oscillator used to generate the RF sidebands, and in the main laser into the dark port of the interferometer. We distinguished between direct optical couplings, and cross-couplings due to the control loops of the auxiliary degrees of freedom. By performing numerical simulations we found that offsets of a few centimeters on any cavity do not significantly affect the optical noise couplings or the cross couplings, as microscopic offsets do. The extreme case in which one of the sidebands is resonant in either or both arm cavities sees a significant increase in

the couplings of laser frequency noise and oscillator phase noise. However, even in this extreme case, the noise budget of the DARM readout signal does not change significantly.

The analysis of control signals and noise demonstrated the possible problems of an RF sideband resonating in the arm cavities: this condition can be avoided by simply setting the arm cavity lengths a few centimeters off from their anti-resonant length. As long as this condition is satisfied, a millimeter precision on the arm cavity length is sufficient. Sub-millimeter precision is desirable for the recycling cavity and the Schnupp asymmetry to have better decoupling among the short degrees of freedom.

To measure the length of the arm and of the recycling cavities, we developed an interferometric technique that uses an auxiliary laser beam. We proved that a precision of 10^{-6} can be achieved on the arm cavities, and 10^{-4} on the recycling cavities. The technique is simple and non-invasive enough to be used on the interferometer during commissioning time without affecting its configuration. By a variation of this technique we measured the g-factor of the arm cavities. These measurements allows us to: a) track changes in the radius of curvature of the arm's optics as in the case of intense thermal loads; and b) predict the resonance profile of higher order spatial modes in the interferometer.

We immediately applied the modeling tools developed for length analysis and the experimental results of the cavity characterizations to the design and the construction of the Caltech 40m advanced interferometer. To improve the control system of the interferometer and its sensitivity to differential arm motion, we modified the base-line optical layout by introducing corrections to the cavity lengths. We thus defined a set of sensing and control signals to decouple the degrees of freedom, and around these we designed and built a low-noise RF system necessary for their implementation.

Importantly, all the tools, knowledge and results achieved at the 40m prototype with this thesis are directly exportable to the Advanced LIGO interferometers, where the implementation of the optical design and control scheme will be crucial to achieve the required gravitational waves sensitivity.

Appendices

Appendix A

Nominal RSE Design

Here we discuss a set of conditions that define the working point of the Resonant Sideband Extraction (RSE) scheme.

A.1 Rules and Conventions

The resonant condition of an optical cavity depends on the gain factor:

$$g_{rt} = r_i r_o \exp\left(i2\omega L/c\right)$$

where r_i and r_o are the reflectances of the cavity input and output mirror, respectively.

It turns useful to rewrite the gain factor as a function of frequency:

$$g_{rt}(\omega_0 + \Omega) = r_i(\omega_0 + \Omega) r_o(\omega_0 + \Omega) \exp\left(i2\omega_0/Lc\right) \exp\left(i2\Omega L/c\right) \tag{A.1}$$

where Ω is the frequency deviation from the carrier ω_0.

Referring to the state of a cavity, some confusion may arise from using the terms resonant or anti-resonant. Here we define the resonant condition according to the phase gain of the light after a round trip. For us resonant means having a phase gain $\phi = Arg[g_{rt}] = 0$. Anti-Resonant means $\phi = Arg[g_{rt}] = \pi$.

- When the light is resonant in the arms, since $r_o \approx +1$, these can be replaced by compound mirrors of reflectivity $\sim +1$:

$$r_{\text{arm}} = -r_i + \frac{t_i^2}{r_i} \frac{g_{rt}}{1 - g_{rt}} = -r_i + \frac{1 - r_i^2}{r_i} \frac{r_i r_o}{1 - r_i r_o} \approx -r_i + 1 + r_i = +1$$

- When not resonant, the arms show a reflectivity equal to -1.

- When resonant, the Michelson has the reflectivity of the arm cavities, i.e $+/-1$, depending if these are resonant or not.

- For a carrier resonant in the arms, the Michelson-Arms compound mirror has reflectance +1. For frequencies non resonant in the arms, it has reflectance -1.

- The Michelson compound mirror has identical reflectance and transmittance on both sides. When the light is resonant in it, that is the microscopic offset of its arms is zero, its scattering matrix looks like this:

$$S_{\text{Mich}} = \begin{pmatrix} 1 & 0 \\ 0 & 1 \end{pmatrix}.$$

A.2 Arm Length

The length of the arms is chosen so that the carrier, but neither sideband, can resonate in the Fabry-Perot cavity. Then the condition on g_{rt} for the sidebands becomes:

$$g(\omega) = r_i r_o \exp\left(i\Omega_m \frac{2L}{c}\right) = -1$$

The sideband modulation frequency has to be such that

$$L_{arm} = \left(n + \frac{1}{2}\right) \frac{c}{2f_m}. \tag{A.2}$$

Since $f_2 = 5f_1$, it is sufficient that the condition is true for f_1, for it to hold for f_2 simultaneously. Whereas if the condition is true for f_2, it does not necessary hold for f_1 too.

In reality the exact anti-resonant condition has to be avoided since it would allow the even harmonics of Ω_m to resonate in the cavity. Because of that a little offset is set on either the modulation frequency or the cavity length.

Also higher order modes of the laser in the cavity have to be taken into account to avoid the degenerate case in which they also resonate (more on that in Section 6.3).

A.3 Recycling Cavities

The central cavity of the interferometer is designed such that it looks under-coupled to signals originated in the arm cavities (i.e. acoustic sidebands), and over-coupled to signals coming from the interferometer input. This has the advantage of reducing the bandwidth of the interferometer's common mode while, at the same time, broadening that of the differential mode, where the GW signals live.

A.4 Power Recycling Cavity Length

The cavity gain of the power recycling cavity is

$$\begin{aligned} g_{prc}(\omega) &= r_{prm} r_{mic}(\omega) \exp\left(i\omega \frac{2L_{pr-bs}}{c}\right) \\ &= r_{prm} r_{arm}(\omega) \exp\left(i\omega_0 \frac{2L_{prc}}{c}\right) \exp\left(i\Omega_m \frac{2L_{prc}}{c}\right) \end{aligned}$$

in which $L_{prc} = L_{prm-bs} + (l_x + l_y)/2$ is the effective length of the cavity.

The carrier and both sidebands have to be resonant in the coupled cavity. For the carrier, since $r_{arm}(\omega_0) = 1$, that means that it has to be anti-resonant in the PRC alone:

$$\omega_0 \frac{2L_{prc}}{c} = 2n\pi.$$

For the sidebands, since $r_{arm}(\Omega_m) = -1$, it has to be that:

$$\Omega_m \frac{2L_{prc}}{c} = (2n+1)\pi$$

and the condition on the power recycling cavity length is:

$$L_{prc} = \left(n + \frac{1}{2}\right) \frac{c}{2f_m}. \tag{A.3}$$

Imposing the condition for f_1 ensures that it is also satisfied for f_2. For the 40m Upgrade $n = 0$.

A.5 Signal Recycling Cavity Length

The cavity gain of the signal recycling cavity is

$$\begin{aligned} g_{src}(\omega) &= r_{srm} r_{mic}(\omega) \exp\left(i\omega \frac{2L_{srm-bs}}{c}\right) \\ &= r_{srm} r_{arm}(\omega) \exp\left(i\omega_0 \frac{2L_{src}}{c}\right) \exp\left(i\Omega_m \frac{2L_{src}}{c}\right) \end{aligned}$$

in which $L_{src} = L_{srm-bs} + (l_x + l_y)/2$ is the effective length of the cavity.

In a RSE signal extraction scheme with dual recycling, the resonance conditions in the signal recycling cavity require both the carrier and the f_2 sidebands to be resonant, and that the f_1 to be non-resonant. That is:

$$\begin{aligned} \omega_0 \frac{2L_{src}}{c} &= 2n\pi \\ \Omega_1 \frac{2L_{src}}{c} &= (2n+1)\pi \\ \Omega_2 \frac{2L_{src}}{c} &= 2n\pi \end{aligned}$$

For these conditions to hold simultaneously, the cavity length has to be

$$L_{src} = n\frac{c}{2f_2}. \tag{A.4}$$

For the 40m Upgrade $n = 1$.

A.6 Schnupp Asymmetry

The length of the Schnupp asymmetry is chosen such that the power of the f_2 sidebands circulating in the signal recycling cavity is maximized. This condition requires that the transmissivity of the power recycling cavity is also maximized, that is, that the cavity is critically coupled to the signal recycling cavity.

The condition for critical coupling requires that the Michelson's reflectivity to f_2 equals that of the HR surface of the power recycling mirror. That is

$$r_{prm}(\Omega_2) = r_{mic}(\Omega_2) = -\cos\left(\frac{\Omega_2 \Delta l}{c}\right) \tag{A.5}$$

where $\Delta l_{asy} = l_y - l_x$ is the Schnupp asymmetry. By inverting Eq. A.5 one gets:

$$\Delta l = \frac{c}{\Omega_2}\cos^{-1}\left(-r_{prm}\right).$$

A.7 40m Upgrade Ideal Optical Parameters

Here we list the ideal cavity lengths chosen accordingly to the modulation frequencies in table 4.1, in which the arm cavity is designed so to make f1 anti-resonant.

	Arms	**PRC**	**SRC**	**Schnupp A.**
Length	$\left(n+\frac{1}{2}\right)\frac{c}{2f_1}$	$\left(m+\frac{1}{2}\right)\frac{c}{2f_1}$	$k\frac{c}{2f_2}$	$\frac{c}{\Omega_2}\cos^{-1}\left(-r_{prm}\right)$

Table A.1: Summary of Cavity Ideal Lengths for RSE. n, m and k are integers.

	Arms	**PRC**	**SRC**
Carrier	resonant	anti-resonant	resonant
f_1 **SB**	anti-resonant	resonant	non-resonant
f_2 **SB**	anti-resonant	resonant	resonant

Table A.2: Summary of RSE Resonance Conditions.

	Arms	**PRC**	**SRC**	**Schnupp A.**
Length [m]	$47.4124-\delta$	6.7732	5.4186	0.0309

Table A.3: Summary of design ideal cavity lengths. The arm length is chosen so to make f_1 almost anti-resonant: δ is an offset (10 cm in this thesis) used to avoid exact anti-resonance.

Appendix B

RF System

B.1 Overview

The 2010 upgrade of the 40m will modify the interferometer optical layout so that it represents more faithfully the latest Advanced LIGO configuration [58].

One of the main changes from the old configuration, is the use of lower modulation sidebands: 11 MHz and 55 MHz. Almost all the parts of the RF system will have to be upgraded.

The main changes will interest the following subsystems:

- **phase modulation**: a new, single, broadband EOM
- **frequency generation**: modulation and demodulation signals generated by a new dedicated unit
- **signal demodulation**: new, single, signal demodulation unit, including 3rd harmonic demodulation
- **photodetectors**: resonant photodetector with 2mm photodiodes

This document describes the design and construction of the modulation/demodulation system. The upgrade of the photodetectors is presented separately in LIGO DOC T1000209.

B.2 RF System Design

The RF system is made of three parts:

1. The first part of the RF system provides the modulation signals necessary to generate three sets of sidebands: $f_1 = 11$MHz, $f_2 = 55$MHz, $f_{mc} = 29.5$MHz.
2. In the second part, the modulation signals are used to add sidebands on the laser beam at the PSL table.
3. The third part demodulates the signals from the photodiodes with pick-off signals of the modulations generated in the first part.

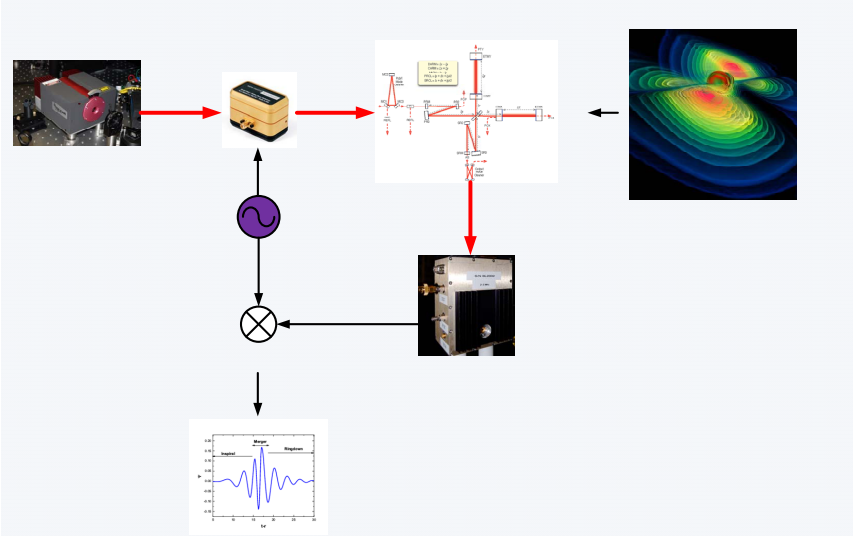

Figure B.1: RF System cartoon.

B.2.1 Frequency Generation

In the previous 40m, the modulations were obtained separately from three Marconi/IFR2023 frequency generators, phase-locked to each other.

Since the required tunability of the modulation frequency is less than few tens of kHz, a wide range frequency generator is superfluous. A dedicated crystal oscillator can perform the task as well, or better. In fact Wenzel crystals guarantee less phase and amplitude noise than a Marconi.

The 40m Upgrade frequencies are generated by only two crystal oscillators: one at 11 MHz, and the other at 29.5 MHz. The first provides directly f_1, and also, indirectly, f_2 via a 5-time frequency multiplier. A Wenzel frequency multiplier guarantees a low relative phase noise between the two sidebands. The second crystal provides f_{mc}.

The modulation signals get amplified and then split in two signals: one to drive the electro-optical modulator (Part 2), the other to be used for demodulation (Part 3).

B.2.2 Phase Modulation: Broadband EOM

The Mach-Zehnder interferometer scheme used to impose the two phase modulations is abandoned in favour of a single triple-resonant EOM [59, 33]. A KTP 4064 broadband EOM by New Focus is connected to a triple-resonant circuit tuned to the EOM capacitance. The three modulations get combined by a 3-way non-resistive splitter/combiner, and drive the resonant EOM.

B.2.3 Demodulation

The 40m upgrade will use the following photodiodes: REFL11, POP11, REFL55, AS55, POP55, POP22, POP110. Additionally 3rd harmonic resonant photodiodes as REFL33, AS33, REFL165, AS165 will be implemented.

To extract the corresponding signals the necessary demodulation frequencies are the 1st, 2nd, 3rd, 5th, 10th, 15th multiples of f_1. While f_1 and f_2 come directly from the Frequency Generation part of the RF system, the other multiples have to be generated by a dedicated demodulation unit.

The function of the unit, is to collect the signals from the Frequency Generation Unit, amplify it, generate the necessary harmonics, and then output the LO signals for the demodulation boards.

B.2.4 Requirements

The minimum requirements on the RF systems are the following:

- the SNR of the Wenzel oscillators should be preserved as much as possible along the line to the EOM and the demodulators
- the EOM should allow us to tune the modulation depth $\gamma = 0.1 - 0.3$

All the parts should be robust, durable, and time resistant.

Power Levels

According to the commercial specs, the KTP 4064 EOM should have an efficiency $\beta =$ 13 mv/rad. In reality, the best we've measured so far is about 9 mV/rad (see [59]). Since we did not measure β at the time of the initial design, we relied on the specs. Based on that, we calculated the required signal power:

$$V_i = \gamma/\beta = (11 - 33)\ V \rightarrow P_i \approx (28 - 40)\ \text{dBm} \tag{B.1}$$

There are not off-the-shelf RF amplifiers available in the market, with low noise figure ($\leq$ 10) and able to output that amount of power, without need of fans for air cooling and large heat sinks. For us the choice was between the Mini-Circuit ZHL-2, and the ZHL-1-2W. The first could offer 28 dBm max power output (1 dB compr.), the second 33 dBm. The ZHL-2 had less heat dissipation, so we picked that.

Since the amplifier could not guarantee more than 30 dBm, we had to require that the EOM resonant circuit provided a gain of 10 dB, at resonance. A prototype of the circuit showed that it was possible [59].

The other contraint was the necessary output power at the demodulation boards [LIGO D990511]. The LO had to have an input power level of 2 dBm.

Phase Noise

The phase noise specified by Wenzel for their crystals is as in the table in Figure B.2.

Once that the source's noise is known, the SNR at the output can be calculated as in Appendix B.5.

Phase Noise L(f)	
10 Hz	-120 dBc/Hz
100 Hz	-150 dBc/Hz
1 kHz	-165 dBc/Hz
10 kHz	-165 dBc/Hz

Figure B.2: Wenzel SC Streamline Crystal Oscillator Phase Noise Specs.

Harmonic Distortion

After passing through amplifiers, together with the main line of an oscillation, there are also harmonics of the fundamental frequency. We also investigated the effect of such additional harmonics on the length sensing and control scheme of the 40m Upgrade.

With *Optickle*, we simulated the effect of higher order harmonics by introducing additional frequencies to the main field source vector. We looked at the effect of changing the amplitude of the harmonics on the linearity range of the error signals used to control the interferometer's main DOF.

The additional frequencies circulating in the interferometer start beating with the carrier, the main sidebands and with each other generating signals that couple into the error signals used to control the interferometer.

From an analysis over different order of harmonics, and amplitudes, we set limits on the power relative to that of the carrier. A summary of the results is shown in Figure B.3.

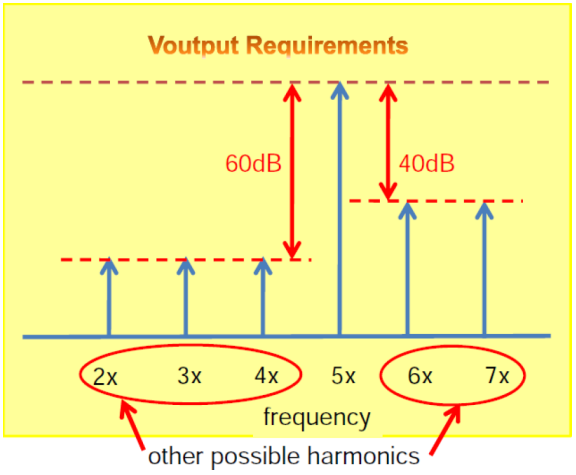

Figure B.3: Requirements on maximum relative amplitude between i-th harmonic and f_1 modulation.

Figures B.4 and B.5 show plots of numerical simulations including high order harmonics. The g_i parameter on the legend measures the *amplitude* ratio between the main signal at 11 MHz and the ith harmonic.

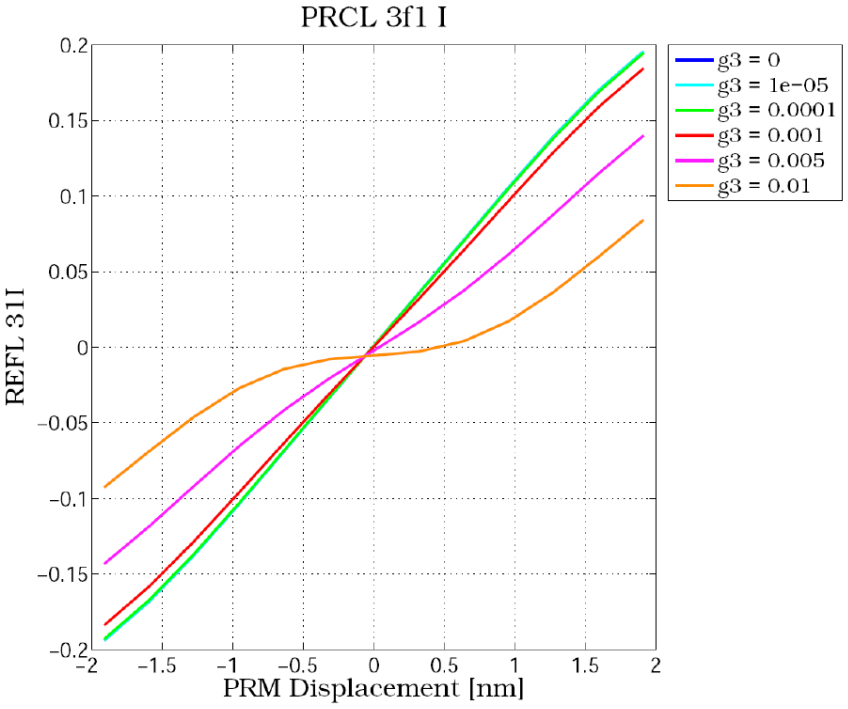

Figure B.4: One the proposed error signals for the control of the PRC, REFL3f1 is plotted. The PRC control signal's gain becomes zero when the 3rd order harmonics is -60dB below the main modulation. The linearity range of the PDH control signals is also reduced.

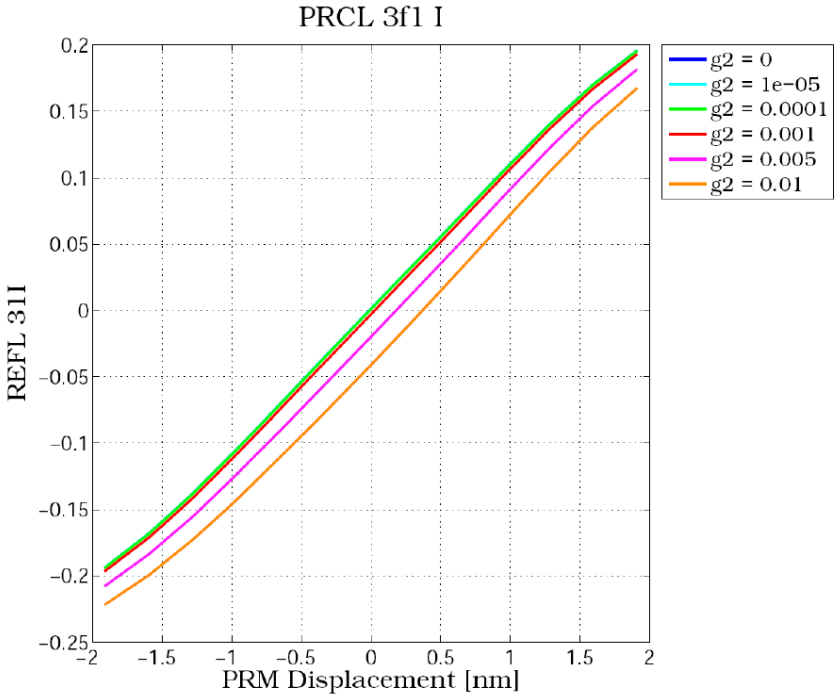

Figure B.5: This plot shows how the locking point can depend on the amplitude of a line at 22 MHz ($2f_2$.

B.3 Frequency Generation Unit

A schematic of the Frequency Generation Unit is shown in Figure B.7.

Figure B.6: 40m Frequency Generation Unit.

The following is a list of the unit's components.

- **crystal oscillators**: 11.065 MHz Wenzel SC Streamline, 29.485 MHz Wenzel SC Streamline;
- **frequency multiplier**: Wenzel 5x LNOM
- **amplifiers**: Mini-Circuit ZHL-2, Mini-Circuit ZFL-1HAD

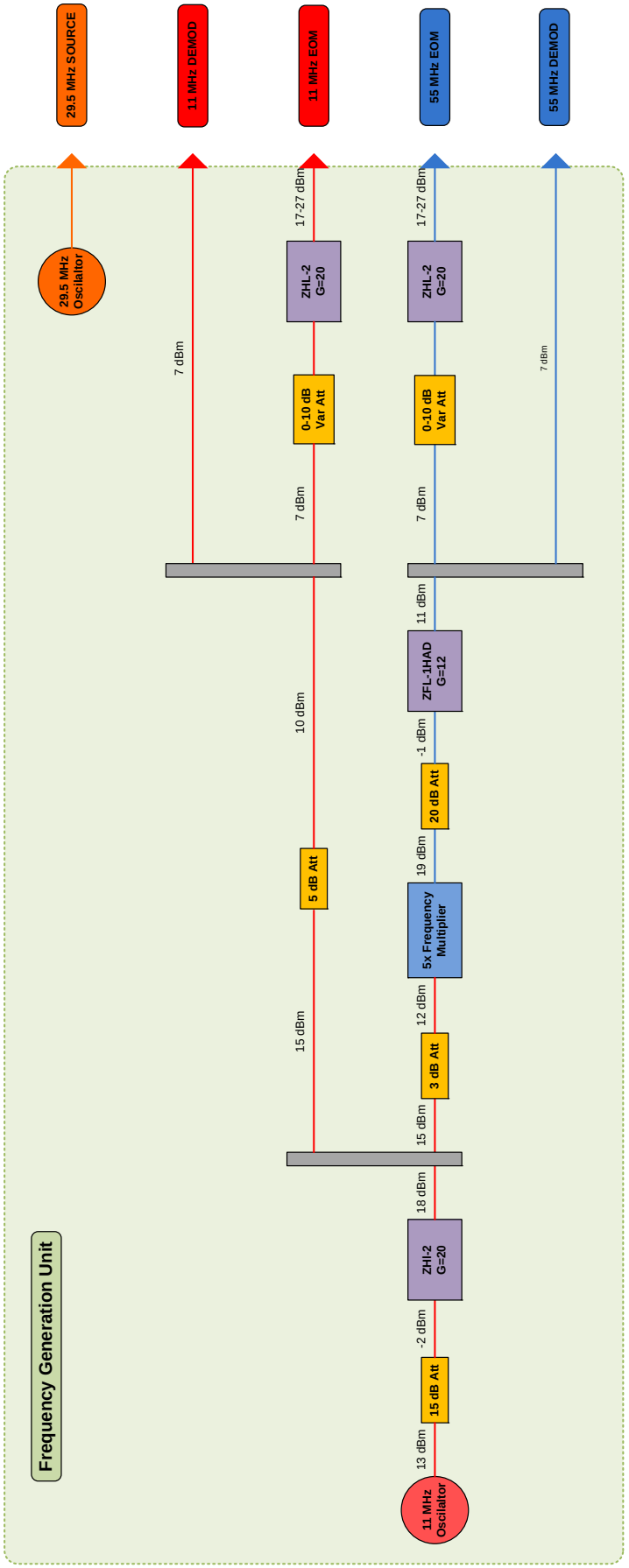

Figure B.7: Frequency Generation Unit diagram.

- **power splitters**: Mini-Circuit ZFSC-2-1W-S+
- **attenuators**: Aeroflex-Weinschel manual step attenuator 3007, Teledyne-Cougar UTF0015 voltage controlled attenuator (purchased but currently not installed), Mini-Circuit power attenuators (SMA)
- **voltage regulators**: Wenzel LNVR 18V-to-15V and 28V-to-24V
- **cables**: RG405 (0.086") coated custom made by Cross RF, Inc.
- **RF connectors**: SMA isolated feedthrough connetcors, N-female to SMA-female feedthrough adapters
- **power connectors**: CPC 4-pin power connector
- **switches**: Schurter MSM 19 LA switch

B.3.1 Powering

The power inputs are: +28V, +18V, GND. A 28-to-24V Low-Noise Voltage Regulator (LNVR) is used to power each of the ZHL-2 amplifiers. The rest of the components gets the 15V DC power from the 18-to-15V LNVR. The LED light of the power switch is also power by one of the 28-24 LNVRs.

Decoupling Capacitors

Bypassing/Decoupling capacitors are attached to the DC power inputs of the ZHL-2 amplifiers. A 10 uF, electrolytic capacitor, and a 0.1 uF ceramic capacitor have been directly attached in parallel to the embedded capacitor at the +24V input connector. The leads were trimmed to avoid their stray capacitance.

The capacitors serve two analogous functions:

- **Decoupling**: The amplification of an input oscillation makes that amplifier absorb a current with the same frequency (more current is absorbed at the crests, less at the bottoms). That becomes a way for the RF signals to couple into the DC line, and thus to affect the other components of the system. The input capacitors are large enough to provide RF filtering at the DC inputs, so that possible RF leakages from other components do not disturb the amplifier.
- **Buffering**: In case of high power amplifier, the required input current fluctuations can be larger and faster than the DC power supply can provide. A large capacitor may provide the necessary buffering.

Two capacitors are needed, one much larger than the other, in order to provide an effective capacitive impedance over a wider frequency range. (Big capacitors have smaller self resonant frequency; that is, they stop to work as capacitors above that point).

Tutorials on how to pick bypassing/decoupling capacitors for high frequency systems can be found in [60, 61].

B.3.2 Grounding

Good grounding has to be provided to the RF components at all time. Since it is not easy to guarantee even contact between the cases and the support surface, we preferred to provide ground to the components only via the input and output connections.

An isolating board made of Teflon has been used as support surface. The components are attached to the board with screws going through it, and locked by nuts on the other side.

To ensure that the components would not share the ground with the chassis and the electronics rack where the box is installed, all the feedthrough connections have been designed to avoid direct contact with the front and the back panels. G10 plastic rings, hand-made in the campus machine shop, are housed inside the connectors' through-holes. Then Teflon washers are sandwiched between the feedthrough connectors' metal washers/nuts and the front panel.

B.3.3 Thermal Dissipation

The electrical isolation of the components from the chassis, poses the issue of heat dissipation. In particular, the LNVRs and the ZHL-2 amplifiers tend to overheat without a proper system to sink their heat.

The solution for the LNVRs, was to attach them directly to the back panel, inserting a thin layer of MICA plastic at the interface. MICA was chosen for its high thermal conductivity. To further improve the contact between the panel and the cases, a thin layer of thermal paste was spread on both surfaces of the MICA sheet (Figure B.8).

For the amplifiers, L-shaped heat-sinks made bending a 3/8" copper sheet, were installed in between the air heat-sink and the amplifier's case. The short side of the L was put in contact with the side wall of the chassis by inserting a MICA sheet covered with thermal paste between the two. Nylon screws were used to lock the heat sink to the panel (Figure B.9).

Temperature Sensor

A temperature sensor was installed on the surface of one of the high power amplifiers. The sensor used was one based on the LM34 transistor, developed at the 40m for tracking the temperature of the interferometer chambers [62]. Before the installation of the heat-sinks on the amplifier, their temperature reached almost 60°C with the box lid closed. With the heat-sinks in place, the temperature was about 35°C with the lid open, and almost 40°C with the lid closed (Figure B.10).

At this time, the temperature with all three amplifiers running for a few hours and the box closed, hasn't been measured yet. It shouldn't be much higher than 40°C. If it was, the box could be used with the lid open, or new heat-sinks should be designed.

Figure B.8: LNVRs attached to the back panel. Electrical isolation is guaranteed by MICA sheets, G10 through-hole rings, Teflon washers.

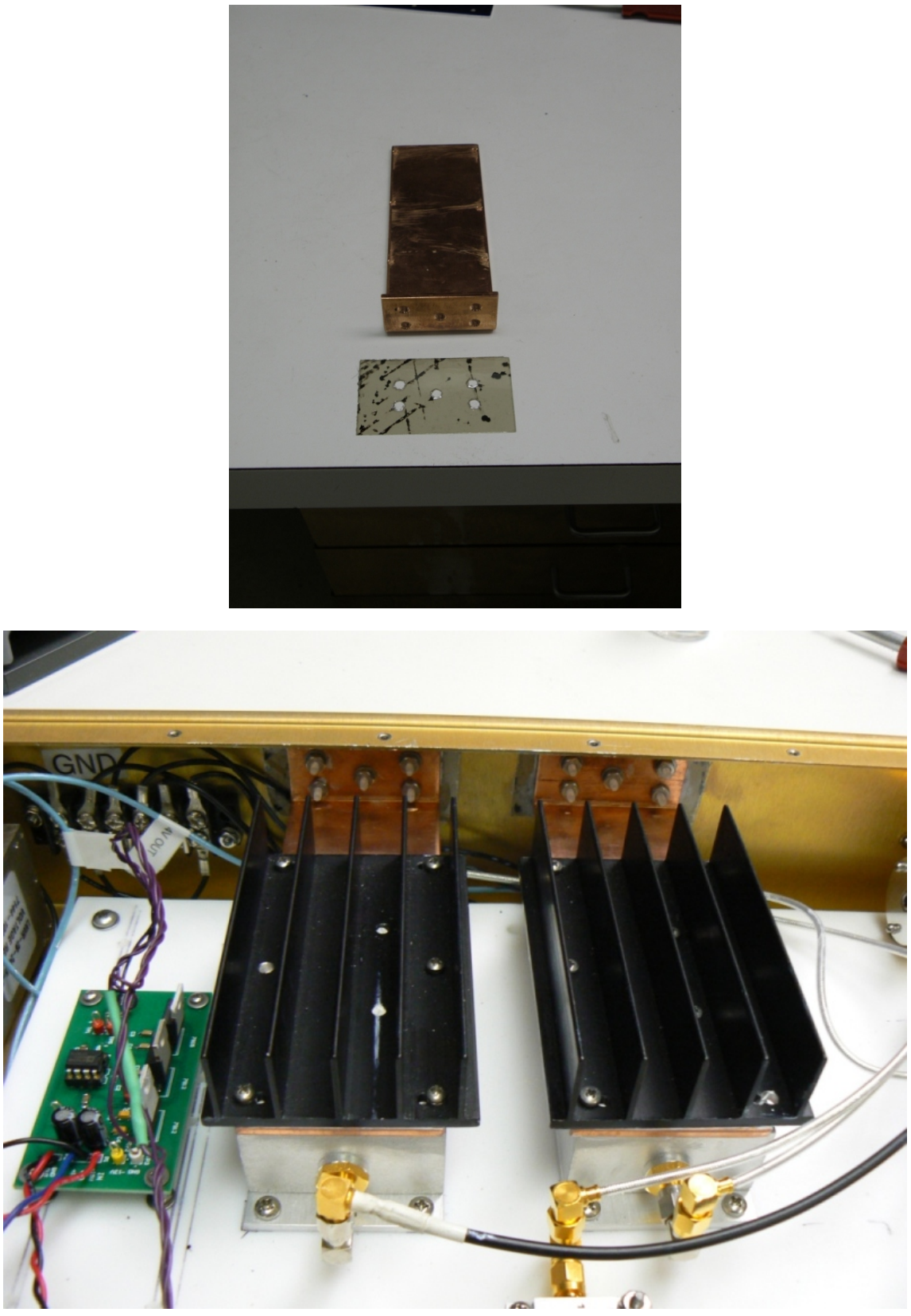

Figure B.9: Heat-sinks installed on the ZHL-2 amplifiers. Made of copper, they are electrically separated from the chassis by MICA plastic sheets covered with thermal paste. Nylon screws lock them to the chassis.

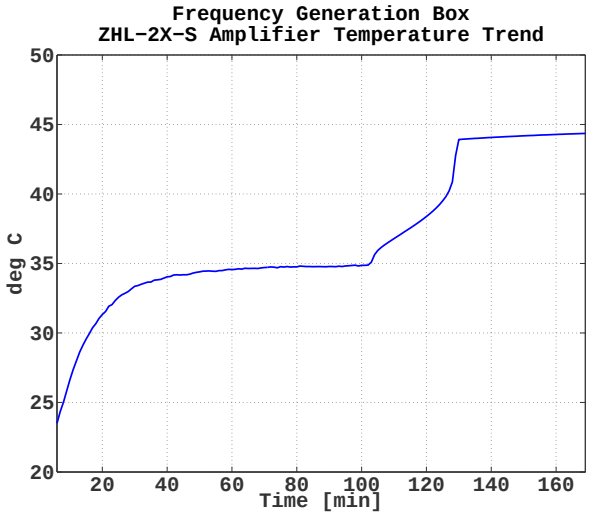

Figure B.10: Temperature trend of one of the ZHL-2, with the box lid open, and later closed. The other amplifiers were turned off at the time of the measurement.

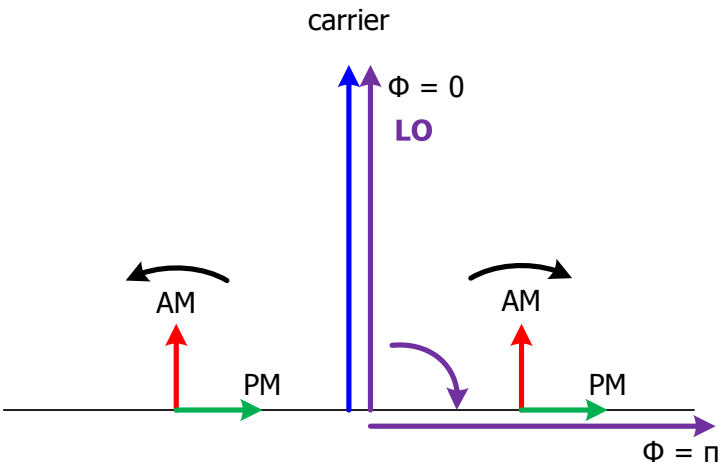

Figure B.11: LO parallel or orthogonal to the RF carrier to measure AM or PM sidebands.

B.4 Oscillator Noise

Noise sidebands in the signal from an oscillator can be measured by homodyne detection. By mixing the source with an auxiliary signal either in phase or in quadrature, one can measure the amplitude modulation or the phase modulation, respectively. In one case the LO is parallel to the RF carrier, and parallel to the amplitude sidebands. In the other, the LO is orthogonal to the RF carrier, and parallel to the phase sidebands (see Figure B.11).

The noisy signal from the source can be written as $v_s(t) = A(t)\sin(\omega t + \phi(t))$, with $A(t) = a_0(1 + h(t))$ and $\phi(t)$ describing the amplitude and the phase fluctuations, respectively. The auxiliary, and noiseless signal can be written as $v_a(t) = V_a \sin(\omega t + \varphi)$. Then,

the output of the mixer, after band-pass filtering, or DC cut-off, is:

$$v_o(t) = \frac{A(t)V_0}{2}\cos\left(\phi(t)+\varphi\right) \Rightarrow \begin{cases} \frac{A_0V_0}{2}\sin\phi(t) & \text{for} \quad \varphi = \pi/2 \\ \frac{A(t)V_0}{2} & \text{for} \quad \varphi = 0 \end{cases} \tag{B.2}$$

Taking the Fourier Transform of both sides of (B.2), one obtains phase noise, for $\varphi = \pi/2$ and amplitude noise for $\varphi = 0$.

B.4.1 Measuring Phase Noise

The phase noise of an oscillator can be measured by using a second oscillator as a reference. The result is the measurement of the combined phase noise of the pair. If the reference oscillator is much less noisy than that to be measured, then the phase noise can be attributed in full to the first.

The measurement requires the use of a PLL that connects the test oscillator and the reference oscillator. To do that, one has to be able to act as a VCO.

In our case, the oscillator under test is a Wenzel Crystal tuned at about 21.5 MHz. The VCO is a Marconi frequency generator (IFR 2023). The setup for the measurement is shown in Figure B.12.

Here $V_1(t) = V_{10}\cos(\phi_1(t))$ and $V_2(t) = V_{20}\sin(\phi_2(t)$ are the oscillations from the sources. When hey get mixed, the result is the loop's error signal $V_e(t) = KV_{10}V_{20}\sin(\phi_1(t) - \phi_2(t))$, where K is the mixers gain. An SR560 amplifies the signals by a factor G, and produces the control signal $V_c = GV_e$ that drives the Marconi's VCO.

The diagram representing the PLL is shown in Figure B.13. In particular in Figure B.13(b) the PLL linearity assumption holds, and the loop is assumed to be already locked. The Marconi plays the part of a noiseless VCO, such that the noise is shifted entirely over the oscillator under test. The following relations hold for the locked PLL:

$$e = \theta_i - \theta_0 - n \tag{B.3}$$

$$v_e = K_d v_e \tag{B.4}$$

$$v_c = K_a v_d \tag{B.5}$$

$$\theta_0 = K_0/s \tag{B.6}$$

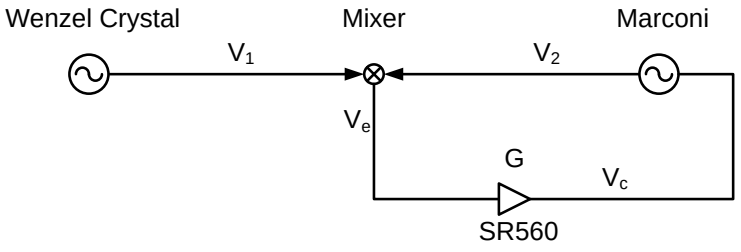

Figure B.12: Phase Noise Measurement Setup

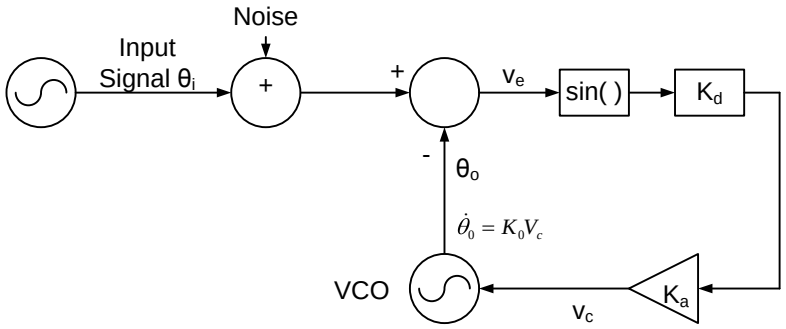

(a) PLL in time domain

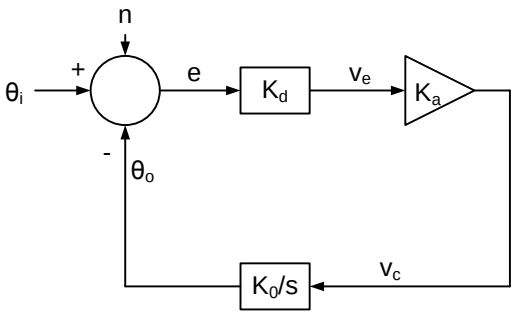

(b) Linearized PLL in s-space

Figure B.13: PLL diagrams: noise n, error signal e, control signal v_c, mixer gain k_d, preamplifier gain k_a.

The open loop gain is

$$G(s) = \frac{K_a K_d K_0}{s} \tag{B.7}$$

and it relates the spectrum of the error signal and that of the noise:

$$\hat{e} = \frac{1}{1+G}\ \hat{n}. \tag{B.8}$$

Since we can measure $\hat{v}_c$, K_d and K_0 separately, and K_a is also known, we can obtain the phase noise:

$$\hat{n} = \frac{1 + K_a K_d K_0/s}{K_a K_d}\ \hat{v}_c \tag{B.9}$$

Measuring the Calibration

The calibration from phase [rad] to volts is given by K_d. It can be measured with the loop open, by looking a the output of the mixer, v_e. There, a sine appears as a consequence of the mismatch between the frequency of the two oscillators due to the open loop. The peak amplitude V_{pk} of the wave is the voltage change corresponding to a phase of $\pi/2$.

$$v_d = K_d \sin(\phi) \tag{B.10}$$

$$K_d = v_d(\pi/2) \tag{B.11}$$

Unit Conversion

$$\delta\phi_{rms}(f)_{[\mathrm{dBc/Hz}]} = 20 \log \left(\frac{\sqrt{2}}{2} \delta\phi_{rms}(f)_{[rad/\sqrt{Hz}]} \right) \tag{B.12}$$

B.4.2 Measurements

The setup used for the measurement is shown in Figure B.14. The Mixer used was the ZFM-3 by Mini-Circuit, with an LO level of +13dBm. The frequency reference was obtained by an IFR2023 frequency generator locked to a Rubidium Frequency Standard.

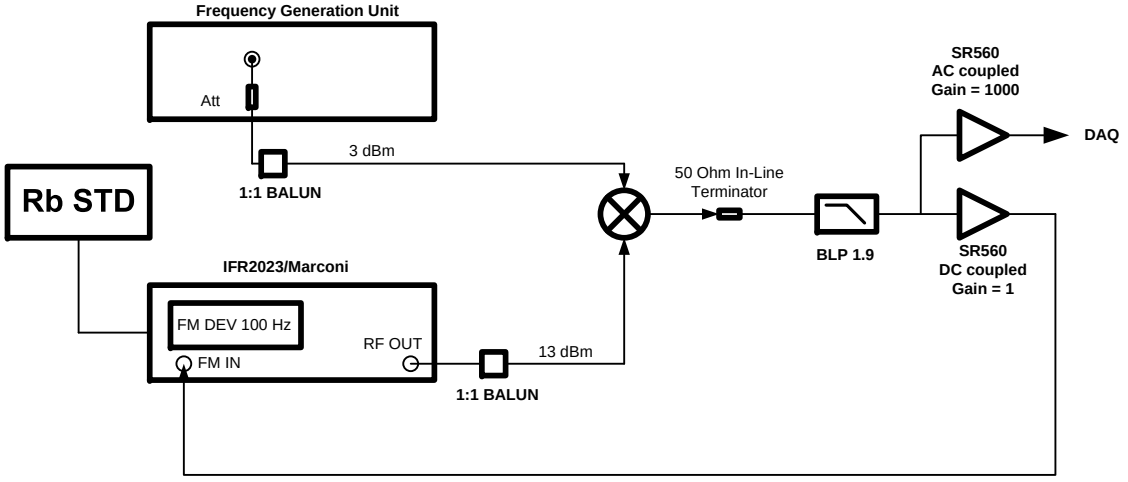

Figure B.14: Phase Noise Measurement Setup.

The results of the measurements over all output channels of the Frequency Generation box are shown in the plot in Figure B.15.

B.4.3 Measuring Amplitude Noise

The amplitude noise of an oscillator can be measured by homodyning the source signal with itself. The measurement setup is shown in Figure B.16.

The signal is first band-passed, then attenuated and split by two. The outputs of the power splitter are attenuated and mixed. The connection between the splitter and the mixer must have the same length for phase preservation (length difference no longer than 1-2 deg). The output of the mixer is low-passed and amplified by a DC coupled preamplifier.

The calibration factor was measured from the DC output level of the mixer. The spectrum density has to be divided by that factor in order to obtain the proper unit.

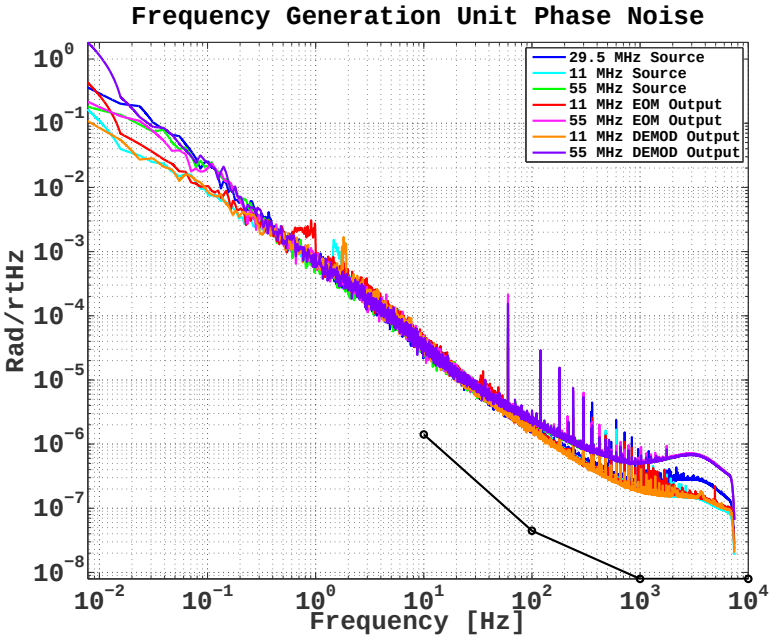

Figure B.15: Phase Noise Measurements on the output channels of the RF Frequency Generation box.

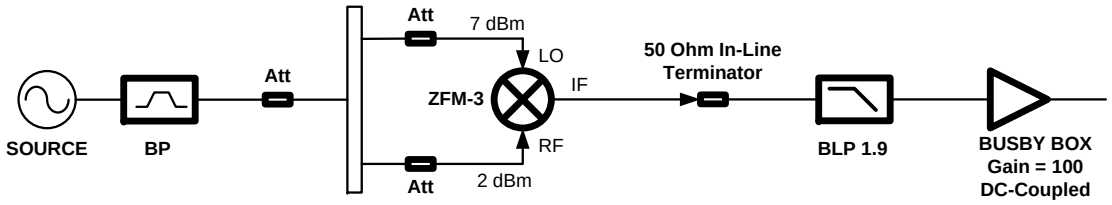

Figure B.16: Amplitude Noise Measurement Setup.

The mixer used was by Mini-Circuit and had a LO level of +7 dBm. The preamplifier was the *Busby Box* with low noise at 1 nV/$\sqrt{\text{Hz}}$.

The results of the measurements are shown in Figure B.17.

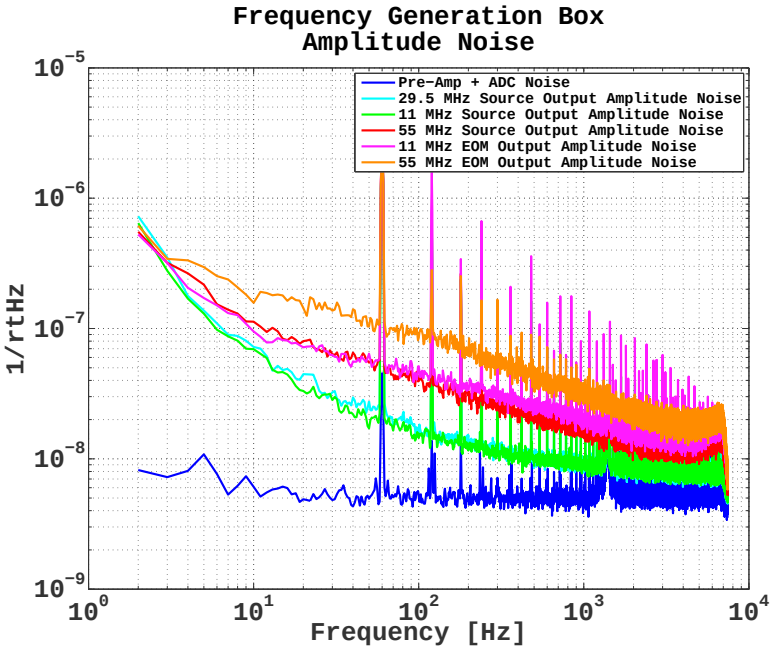

Figure B.17: Amplitude Noise Measurements.

B.5 Amplifier Noise Figure

The Noise Figure of an amplifier is the ratio, in decibels, of the output of a "real" amplifier to the output of a "perfect"(noiseless) amplifier for the same gain, with a resistor R_s connected in series to the input (Fig. B.18). The Noise Figure does not provides an absolute value of the noise added by an amplifier. It rather expresses noise relatively to that of the Johnson's noise of the source impedance.

$$\text{NF}(Z_{in} \gg R_s) = 10\log_{10}\left(\frac{4k_B R_s T + v_n^2}{4k_B R_s T}\right) \tag{B.13}$$

Here's ho to convert from NF to SNR:

$$\text{SNR}_{\text{dB}} = 10\log_{10}\left(\frac{v_s^2}{4k_B T R_s}\right) - \text{NF}_{\text{dB}}(R_s) \tag{B.14}$$

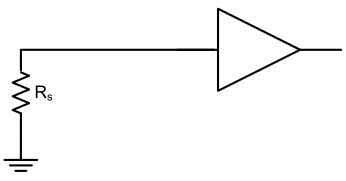

Figure B.18: Diagram representing the definition of Noise Figure.

where v_s is the rms signal amplitude, R_s is the source impedance and NF is the noise figure of the amplifier for source impedance R_s. For example, for the MAX4107 opamp contained in the 40m PD'c circuit, which has a noise $v_n = 0.75nV/\sqrt{Hz}$, and for a 50Ω source impedance, we have NF($R_s = 50\Omega$) = 2.3dB.

B.5.1 RF Amplifiers

For RF amplifiers, in which the input impedance is matched with the source impedance, both being 50Ω, then the the factor of four in the Johnson's noise power gets dropped:

$$v_{in}^2 = 4k_B R_s T \left(\frac{Z_{in}}{R_s + Z_{in}} \right)^2 = k_B R_s T \tag{B.15}$$

The Noise Figure at RF is then *for a typical 50Ω input impedance RF amplifier; i.e. the amplifiers from Mini Circuit*[1]:

$$\mathrm{NF}_{\mathrm{amp}}^{\mathrm{RF}} = 10 \log_{10} \left(1 + \frac{v_n^2}{k_B R_s T} \right). \tag{B.16}$$

B.6 Frequency Distribution Unit

A schematic of the Frequency Distribution and Demodulation Unit is shown in Figure B.19.

B.7 Drawings

[1] Note that the factors of 4 have been dropped from the Johnson's noise term because of the amplifier's input impedance. See Horowitx-Hill, pag. 435)

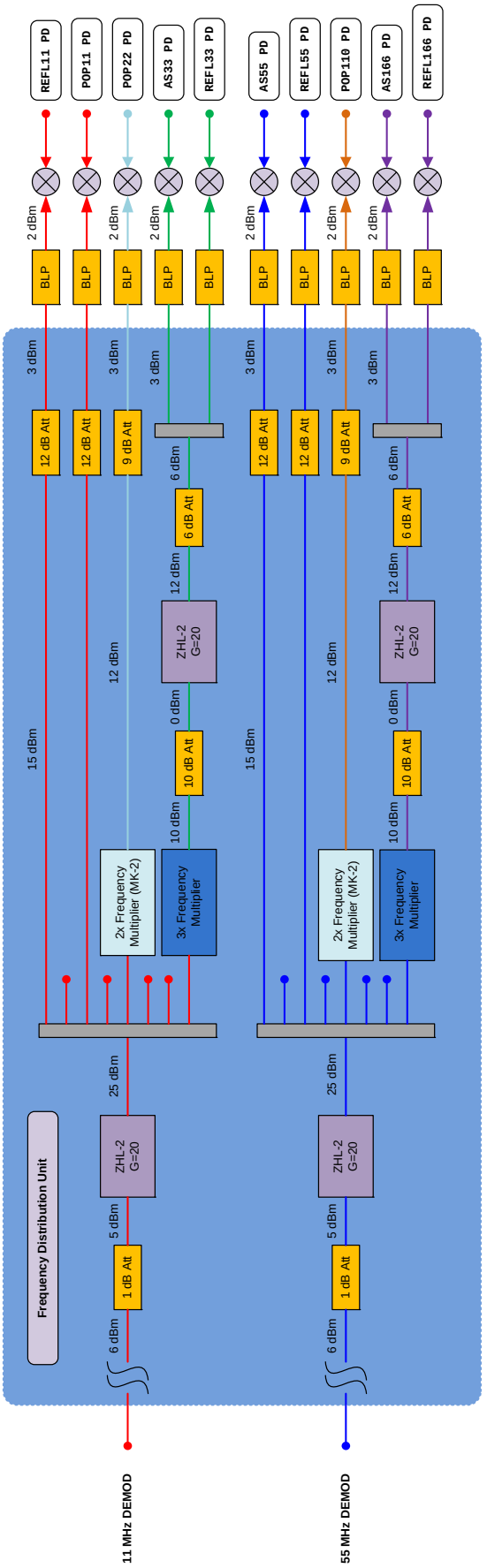

Figure B.19: Frequency Generation Distribution Unit diagram.

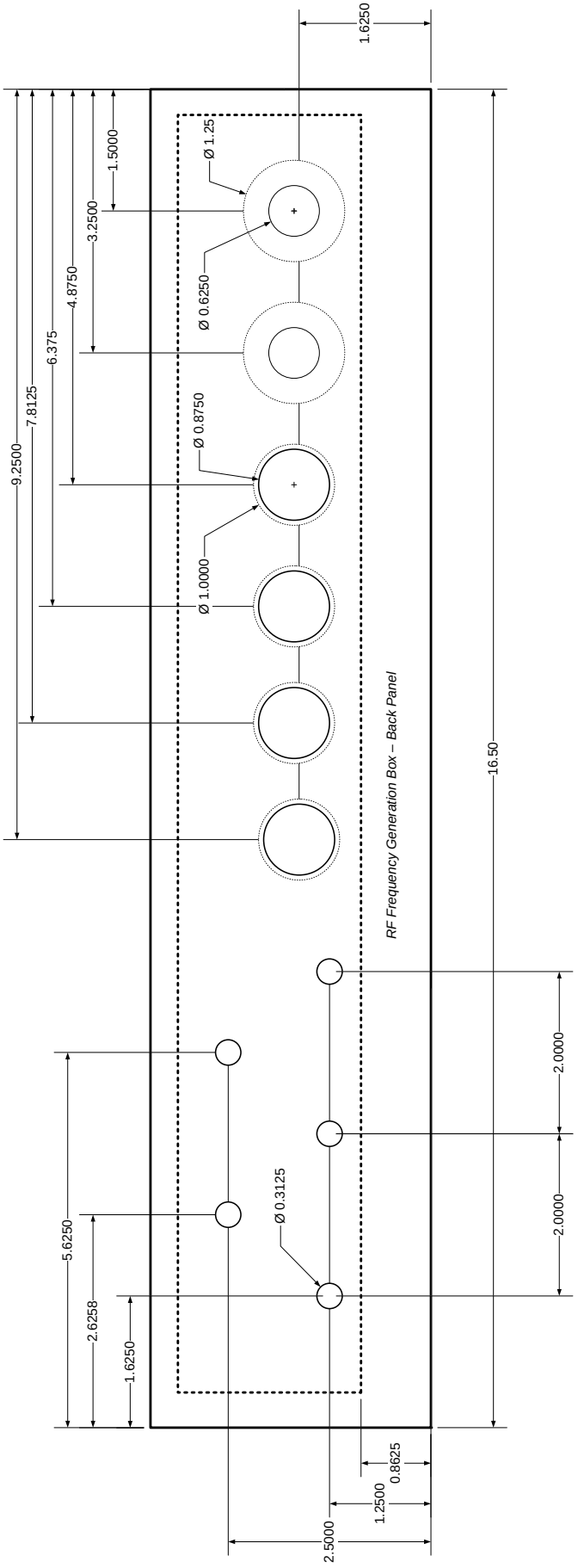
1.6250
Ø 1.25
Ø 0.6250
Ø 0.8750
Ø 1.0000
Ø 0.3125
1.5000
3.2500
4.8750
6.375
7.8125
9.2500
16.50
2.0000
2.0000
5.6250
2.6258
1.6250
0.8625
1.2500
2.5000
RF Frequency Generation Box – Back Panel

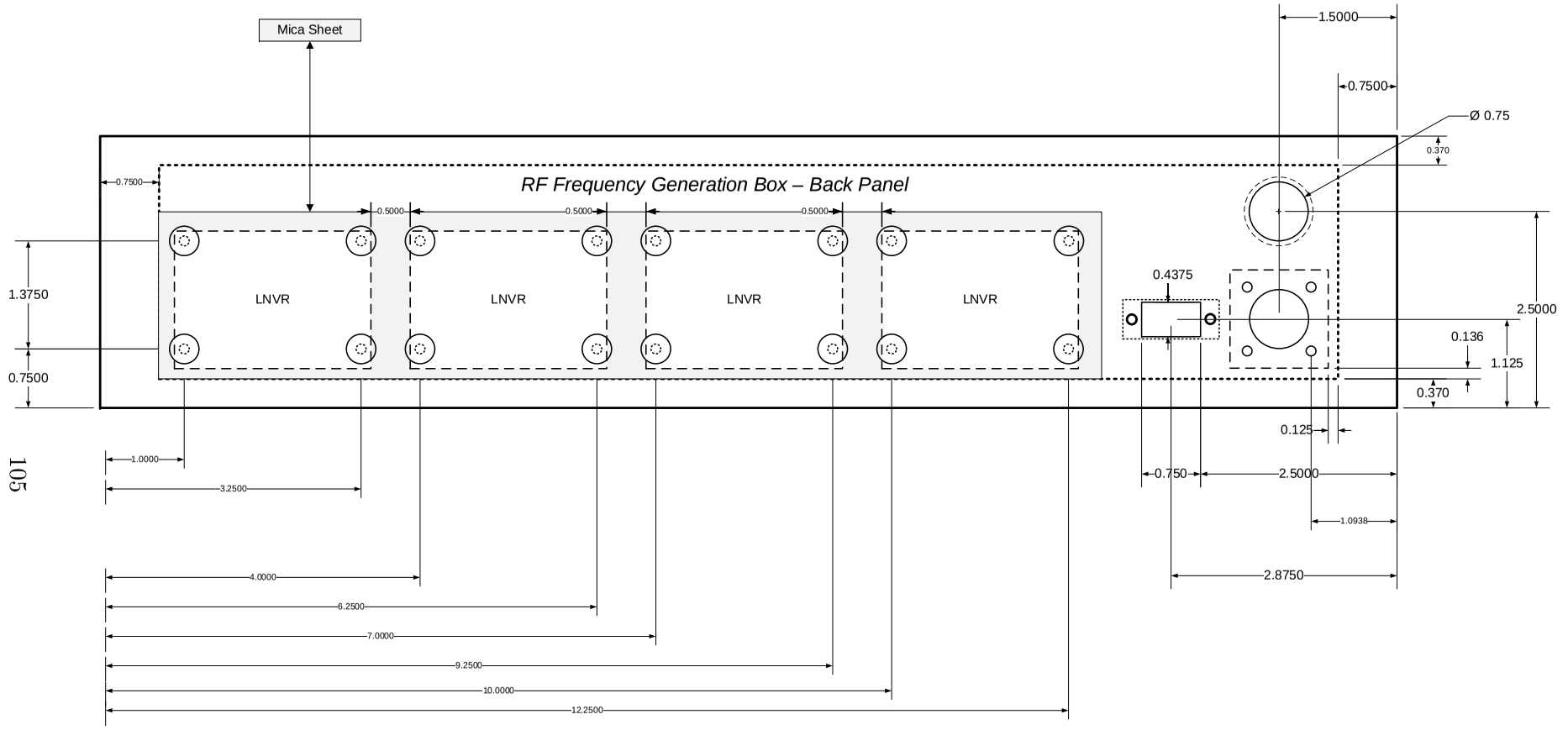
Mica Sheet
RF Frequency Generation Box – Back Panel
LNVR
LNVR
LNVR
LNVR
1.5000
0.7500
Ø 0.75
0.370
0.7500
0.5000
0.5000
0.5000
1.3750
0.7500
0.4375
2.5000
0.136
1.125
0.370
0.125
1.0000
3.2500
0.750
2.5000
1.0938
4.0000
6.2500
7.0000
9.2500
10.0000
12.2500
2.8750

105

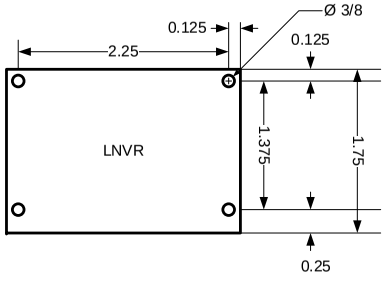
Ø 3/8
0.125
0.125
2.25
LNVR
1.375
1.75
0.25

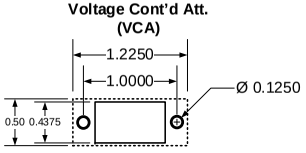
Voltage Cont'd Att.
(VCA)
1.2250
1.0000
Ø 0.1250
0.50
0.4375

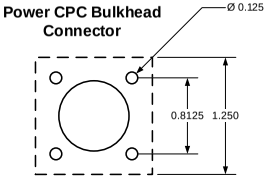
Power CPC Bulkhead
Connector
Ø 0.125
0.8125
1.250

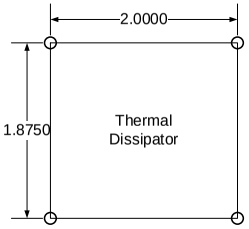
2.0000
1.8750
Thermal
Dissipator

Appendix C

Photodetectors

The 2010 Upgrade of the Caltech 40m Interferometer Prototype [27] required the design and construction of new resonant photodetectors, tuned for the new modulation frequencies of the RF signal extraction system (see Appendix B. This appendix describes the main issues encountered in this process, which was part of our research work.

C.0.1 Resonant Circuit

Figure C.1 shows the main part of the resonant circuit of the photodetector. This can be schematize by a bipolar component with an effective impedence:

$$Z = \frac{j\omega L_5 - \omega^2 R_{PD} L_5 C_{PD}}{1 - \omega^2 L_5 C_{PD} + j\omega R_{PD} C_{PD}} \tag{C.1}$$

where R_{PD} and C_{PD} are the PD's resistance and capacitance, respectively[1].

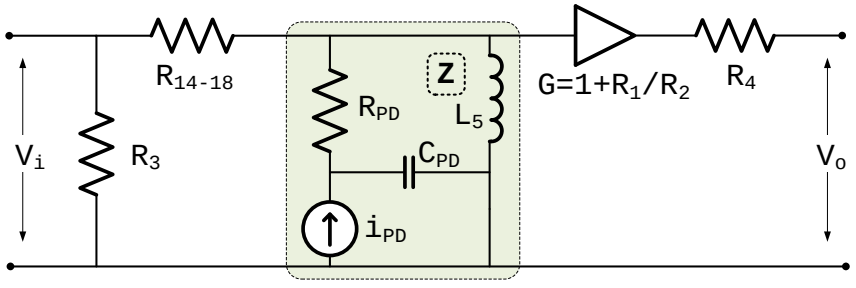

Figure C.1: 40m RF PD Simplified Schematic

The resonant frequency is:

$$\omega_0 = \frac{1}{\sqrt{L_5 C_{PD}}} \tag{C.2}$$

and it depends only on the resonant inductance and on the PD's capacitance.

[1] To avoid confusion in trying to identify the resonant impedance, note that the circuit made by the parallel of C_{PD} and the series $L_5 - R_{PD}$ as seen from the current source i_{PD} is a 3-way object and cannot be represent by a bipolar impedance

C.0.2 Response Parameters

At resonance, the resonant part of the circuit, as seen from the current source i_{PD}, has impedance:

$$Z(\omega_0) = \left(\frac{L_5}{R_{PD} C_{PD}} - j\sqrt{\frac{L_5}{C_{PD}}} \right) \tag{C.3}$$

Resonance Q

The Q-factor of the resonant circuit is expressed by the ratio of stored energy in the resonant impdedance Z over the energy loss during one cycle:

$$Q = 2\pi \frac{\text{energy stored}}{\text{energy loss per cycle}}. \tag{C.4}$$

One way to evaluate the Q of the resonant circuit is by calculating the tranfer function between the current across the inductor L_5 and the current from the PD source i_{PD}. By assuming that no current flows to R_{14-18} or the amplifier becasue of their high impedance, the current on the iductor is such that:

$$\frac{i_L}{i_{PD}} = \frac{v_L / z_L}{i_{PD}} = \frac{\omega_0^2}{\omega_0^2 - \omega^2 + j\omega_0^2 RC\omega} \tag{C.5}$$

By comparison with the general expression for a second order system:

$$H(\omega) = \frac{\omega_0^2}{\omega_0^2 - \omega^2 + j\frac{\omega_0}{Q}\omega} \tag{C.6}$$

$$Q = \frac{1}{R}\sqrt{\frac{L}{C}} = \frac{1}{\omega_0 RC} \tag{C.7}$$

From (C.7) we can see that the quality factor is directly proportional to the reactive part of the impedance, which is inversely proportional to the photodiode internal resistance; $R_{PD} \approx 10\,\Omega$. For given resonant frequency ω_0, the Q is improved by maximixing the resonant inductance, and minimizing the PD'd effective capacitance. The impedance as a function of frequency is plotted in figure (C.2), for different values of the PD's capacitance.

RF Transimpedance

The Transimpedance $\mathcal{T}$ measures the ratio between the output voltage of the amplifier and the photocurrent i_{PD}:

$$\mathcal{T} = G\frac{v_{L5}}{i_{PD}} \tag{C.8}$$

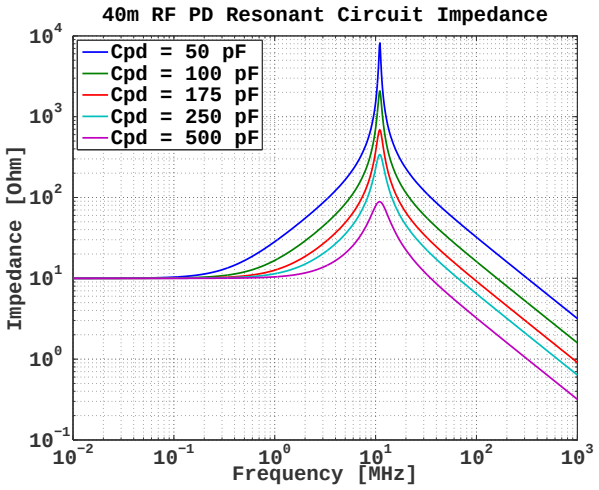

Figure C.2: 40m RF PD Resonant Circuit: Voltage across L_5 over photocurrent i_{PD}

where $G = 1 + R_2/R_1$ is the feedback gain of the amplifier. v_{L5} is the voltage across the inductor L_5 and it is obtained from the impedance Z of (C.3) by the following:

$$v_{L5} = Z \frac{j\omega L_5}{R_{PD} + j\omega L_5} \tag{C.9}$$

From (C.9) the transimpedance at resonance is obtained:

$$\mathcal{T}(\omega_{res}) = G \frac{L_5}{R_{PD} C_{PD}} \tag{C.10}$$

$$\equiv G\mathcal{Z} \tag{C.11}$$

$$\mathcal{Z} = \Re[Z_0] = RQ \tag{C.12}$$

DC Transimpedance

Because $R_{14-18} \sim 1K\Omega$, at DC almost all photocurrent goes through $R_{PD} = 10\ \Omega$ and $R_{22} = 10\ \Omega$ in series. The U7 amplifier (LT1128) reads the voltage between the two resistors and multiplies it by a loop gain $G_{DC} = (1 + R_{13}/R_{23}) = 5$. The transimpedance at DC is then:

$$\mathcal{T}_{DC} = G\ R_{22} = 50\ V/A \tag{C.13}$$

N.B. The value of the DC transimpedance as calculated in C.13 is referred to a 1 $M\Omega$ impedance. This is the opposite convention from tha one used by New Focus for the NF1811 PD. The New Focus values, both DC and RF transimpedance are referred to a 50 Ω impedance in the scope.

2f Notch Q

Notch filters are connected before the MAX4107 to stop: a) the second harmonic; b) the other sideband's frequency. The filters are made of a LC series with resonant frequency $\omega_{\text{notch}} = 1/\sqrt{LC}$. The Q-factor of the filter is:

$$Q_{\text{notch}} = \frac{1}{R_L C}$$

where R is the inductor's resistance.

Bandwidth

For how the amplifier feedback affect the bandwidth see [63].Reverse biasing the photodiode, reduces the effective shunt capacitance and thus increases the bandwidth.

C.1 PD Design

The goal of photodiode design, and commissioning, is to optimize the photodiodes so that shot noise is the dominant noise; i.e. the electronics should not add any substantial noise to that intrisinc of the light, in the measurement band and for the expected light power levels.

C.1.1 Noise Sources

The total signal at the RF output of the PD is affected by several sources of noise. Mainly these are:

- shot noise of the photocurrent
- Johnson's noise of the resonant circuit
- amplifier's noise (op-amp noise + feedback resistors' noise)

Shot Noise

The variance on the fluctuations of the PD photocurrent due to shot noise is:

$$\delta i_{SN} = \sqrt{2eI_{DC}\delta f} \tag{C.14}$$

where I_{DC} is the average current produced emitted by the photodiode for an incident average power P:

$$i = \mathcal{R}P_{inc} \tag{C.15}$$

The coefficient $\mathcal{R}$ is the *Responsivity* of the photodiode. The fluctuations in voltage at

the DC output of the photodetector due to the shot noise are

$$\frac{\delta v_{SN}}{\sqrt{\delta f}} = Z\sqrt{2e\mathcal{R}P_{inc}} \tag{C.16}$$

where Z is the resonant impedance. We can omit the division by the bandwidth δf, by assuming that we are dealing with spectral densities. From now on, for sake of notation's semplicity, we will also omit the *hat* sign from the quantities representing spectral density. Then we can simply rewrite (C.16) as:

$$v_{sn} = Z\sqrt{2eI_{DC}} \tag{C.17}$$

where $[v_{sn}] = V/\sqrt{Hz}$.

C.1.2 Nonstationary Shot Noise

The shot noise of a phase modulated light is extensively treated in [43]. Phase modulation introduces frequency and quadrature phase dependence to the noise spectrum. In particular correlations in the noise components show up at the harmonics of the modulation frequency. Depending on the modulation depth and on the phase of the noise the RMS noise can vary between $\frac{1}{2}$ and $\frac{3}{2}$ the steady noise of (C.14).

Johnson Noise

The Johnson noise of any network of impedances is given by the sum *in quadrature* of the voltages across each of the component impedances. These voltages are obtained by representing each component as a perfect (noiseless) impedance in series to a Johnson-noise voltage generator. By using that approach, it can be shown that the total Johnson noise at the terminals of the network is that of the network's equivalent impedance ([64], pag. 682-683).

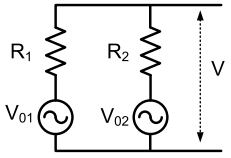

Figure C.3: Johnson noise of parallel resistors. $V_{01} = \sqrt{4k_BR_1T}$ and $V_{02} = \sqrt{4k_BR_2T}$ are the Johnson noises associated with R_1 and R_2, respectively.

In the example of Fig. C.3, given two resistors R_1 and R_2 in parallel, each assosiated to a Johnson noise $V_{01} = \sqrt{4k_BR_1T}$ and $V_{02} = \sqrt{4k_BR_2T}$ respectively, the noise of the parallel is

$$v_n^2 = \left(\frac{R_2}{R_1+R_2}V_{01}\right)^2 + \left(\frac{R_1}{R_1+R_2}V_{02}\right)^2 = 4k_B(R_1 \parallel R_2)T. \tag{C.18}$$

We call Z_s the impedance seen by the amplifier when no signal is applied to the test input of the circuit (Fig. C.4: $Z_s = (R_{14-18} + R_3) \parallel Z$.

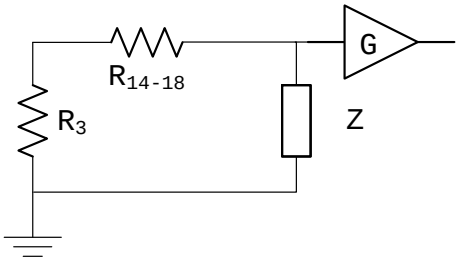

Figure C.4: 40m RF PD impedance of opamp input circuit.

Since at resonance $Z(\omega_0) = Z_0 \ll (R_{14-18} + R_3)$, $Z_s \approx Z_0$. Then the Johnson noise at the output of the resonant part of the circuit is dominated by that associated to the real part of the resonant impedance Z_0.

$$v_{n,th} \approx \sqrt{4k_B \Re[Z_0]T} = \sqrt{4k_B \mathcal{Z} T} \tag{C.19}$$

Amplifier's Noise

The input noise of a noninverting amplifier - as the MAX4107 in the 40m RF PDs - can be represented by the model in Fig.(C.5).

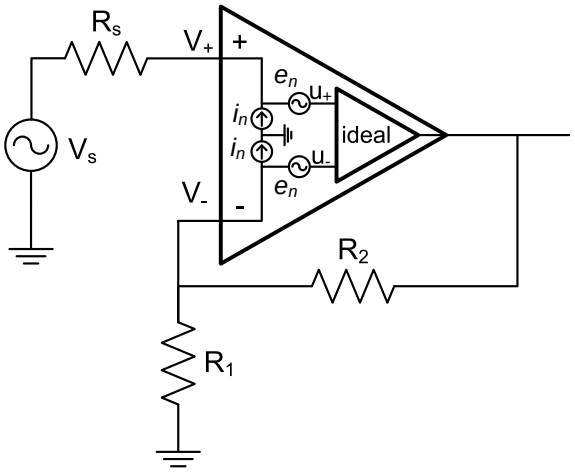

Figure C.5: Noninverting amplifier input noise model.

At each terminal of the opamp is associated a series voltage noise generator e_n and a current noise generator to ground i_n. The noise model represents such sources connected to a perfect (noiseless) amplifier. With reference to the model of Fig.(C.5), the amplifier's in-loop noise contribution e to a signal with source resistance R_s is:

$$v_{n,amp}^2 = v_+^2 + (R_s i_n)^2 \tag{C.20}$$

where the current noise i_n produces voltage noise at the input when the source impedance

is connected. The following relations apply:

$$u_+^2 = u_-^2 = v_-^2 + e_n^2 \tag{C.21}$$
$$v_+^2 = e_n^2 + u_+^2 = e_n^2 + v_-^2 + e_n^2 \tag{C.22}$$

Because the output of the op-amp presents a very little impedance to ground, the feedback resistors can be represented by an equivalence parallel resistance to ground $R_\parallel$. The voltage v_- at the negative connector is given by the sum in quadrature of the Johnson noise from $R_\parallel$, plus the voltage noise generated by the current noise across $R_\parallel$:

$$v_-^2 = 4k_BTR_\parallel + \left(i_nR_\parallel\right)^2 \tag{C.23}$$
$$R_\parallel = \frac{R_1R_2}{R_1+R_2}.$$

The in-loop input noise is then:

$$v_{n,amp}^2 = 2e_n^2 + 4k_BTR_\parallel + \left(i_nR_\parallel\right)^2 + (R_si_n)^2. \tag{C.24}$$

In the case of the MAX4107 of the 40m PDs, and, for instance $\mathcal{Z} \sim 100\ \Omega$ we have:

$$\begin{aligned} e_n &= 0.75\ nV/\sqrt{Hz} \\ i_n &= 2.5\ pA/\sqrt{Hz} \\ R_\parallel &= 45\ \Omega \\ R_s &= \mathcal{Z} \\ v_{n,amp} &= 1.70\ nV/\sqrt{Hz}. \end{aligned} \tag{C.25}$$

The in-loop noise voltage and the current voltage are now not completely uncorrelated. Calculations in which they are added can be in error by a maximum factor of 1.4 (pag. 447 of [65]).

C.1.3 RF Transimpedance

The optical response of the PD can be measured with an AM-modulated laser.

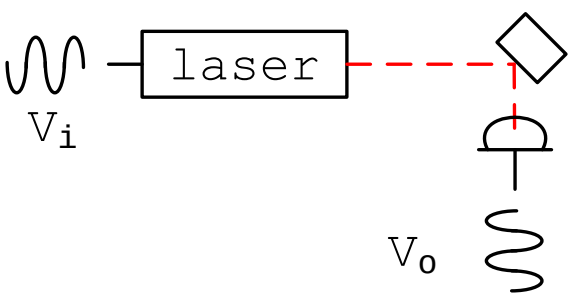

Figure C.6: Experimental setup to measure transimpedance.

The power of the AM-modualted *beam* on the PD is

$$P(t) = P_0 \left(1 + \gamma(\Omega) \sin(\Omega t)\right)$$

Ω is the modulation frequency; $\gamma(\Omega)$ is the modulation depth; P_0 is the DC beam power.

The transimpedance of the photodiodes can be measured relatively to that of a known reference photodiode. Fig.C.6 represents the procedure. In our case the reference photodiode is a New Focus 1811. An AM-modulated photodiode provides the reference beam.

With the spectrum analyzer we can measure the transfer function between the photodiode output V_o and the AM laser input V_i:

$$H(\omega) = \frac{V_o}{V_i}.$$

C.2 Noise Measurement

We want to measure the photodiode noise to check whether it is more or less than the expected shot noise. If it were more, it would mean that the electronics noise is dominating.

C.2.1 Minimum Incident Power

We need a quiet light source, only shot noise limited - at least at RF: an incandescent light bulb.

The minimum power requirement can be estimated from the dark noise measurement. The noise spectrum is composed by shot noise and dark noise:

$$\hat{V} = \hat{V}_{SN} + \hat{V}_{DN}. \tag{C.26}$$

Basically, since we are going to compare $\hat{V}$ and $\hat{V}_{SN}$ we want the shot noise to be far enough from the dark nois. We measure $\hat{V}_{DN}$ and we estimate I_{DC} so that $\hat{V}_{SN}(I_{DC}) \sim \hat{V}_{DN}$:

$$V_{SN} = \mathcal{T}_{RF}\sqrt{2eI_{DC}} \sim V_{DN} \tag{C.27}$$

$$I_{DC} = \frac{1}{2e}\left(\frac{V_{DN}}{\mathcal{T}_{RF}}\right)^2 \tag{C.28}$$

$$V_{DC}^{(\min)} \sim \frac{\mathcal{T}_{DC}}{2e}\left(\frac{V_{DN}}{\mathcal{T}_{RF}}\right)^2 \tag{C.29}$$

C.2.2 Noise

We simulates the electronics noise of the system by LISO, a program for Linear Simulation and Optimization of analog electronic circuits [66]. Figures C.8 and C.9 show the results for the 11 MHz and the 55 MHz photodiodes.

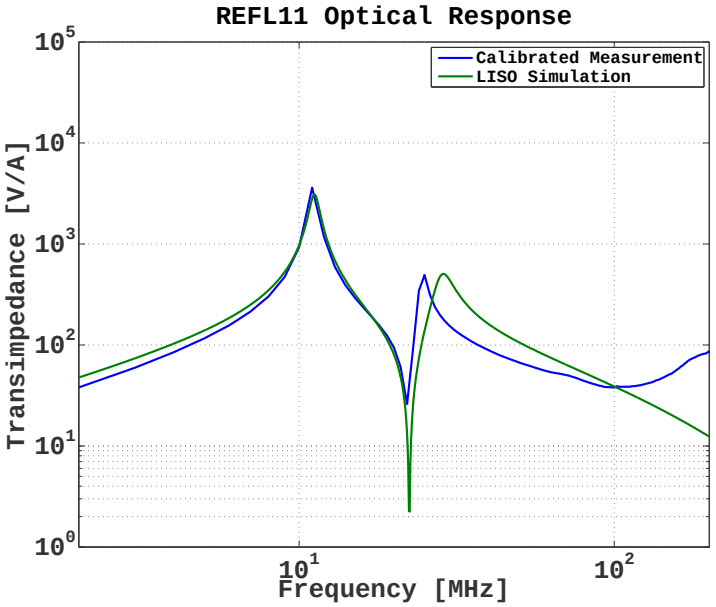

Figure C.7: REFL11 calibrated measurement vs. simulated response

.

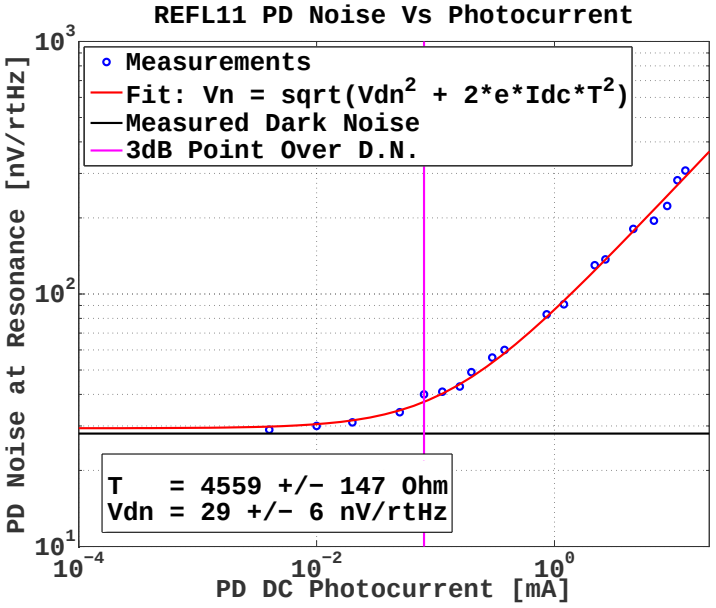

Figure C.8: REFL11 noise measurement fit with model.

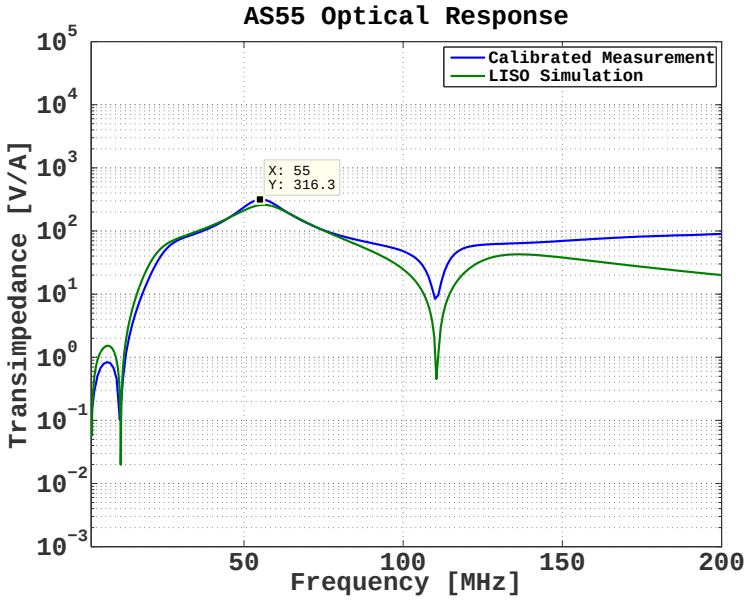

Figure C.9: AS55 calibrated measurement vs. LISO simulated response.

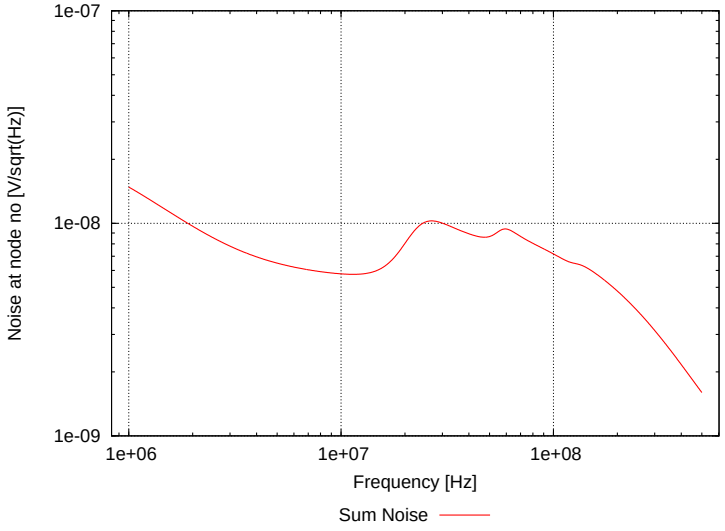

Figure C.10: AS55 LISO simulated noise.

C.3 Circuit Analysis

The 40m Upgrade photodiodes are built upon the initial LIGO design, with which they share circuit board and case (figure C.11.

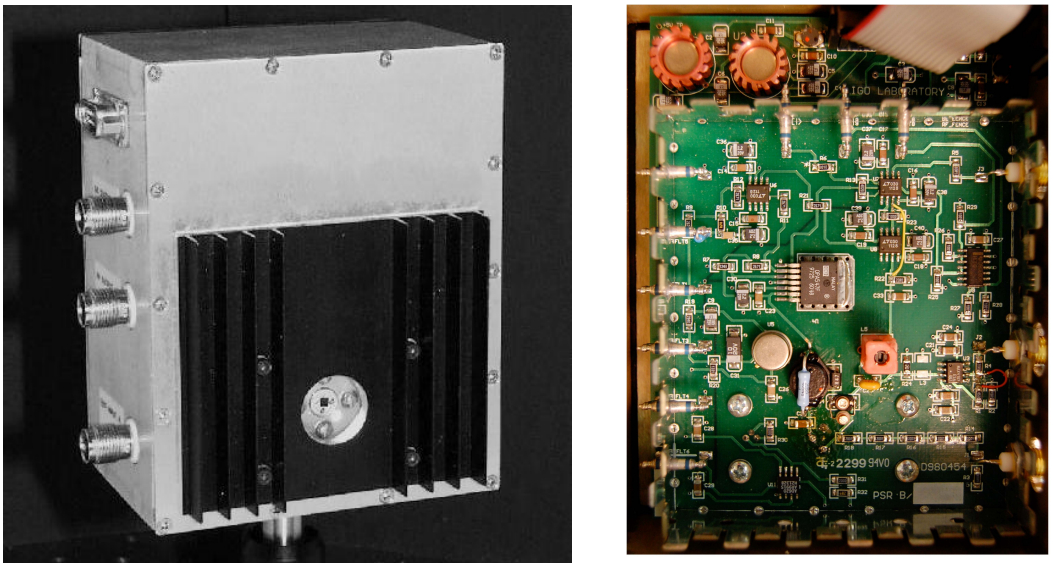

Figure C.11: RF Photodiode case (left) and internal circuit (right).

We can estimate the transimpedance by looking at the schematic of the electronics of the photodetector. Consider the schematic in Fig. C.12.

- Op-amp U8, after L5, is a buffer and feeds back to the photodiode the current that it produces. In this way the voltage drop at the terminations of the PD is kept constant to avoid the capacitance to change. The loop has a gain of 2 set by the ratio $R_{12}/R_{21} = 2$. The reason of the factor of 2 is purely empirical [Rana].
- Op-amp U6 is a summer. At the node between R_9, R_{12}, R_{21} the currents from the V_c *adjust*, the 15V bias supply and the feedback from U8 sum up.
- Op-amp U4 is just an amplifier with a gain of -1.
- The + connector of U8 shows infinite impedance: at DC, the current from L5 goes all through R_{22}.
- The voltage drop V at R_{22} is the same at the output of U8.
- The output of U7 is $V^{'} = 5 \times V$ because $R_{13}/R_{23} = 5$.
- The DC output $V_{out,DC}$ when measured with a scope of $R_s = 1M\Omega$ input impedance is

$$V_{out,DC} = R_s/(R_6 + R_s)V^{'} \approx V^{'} = 5 \times R_{22} i_{\varphi}.$$

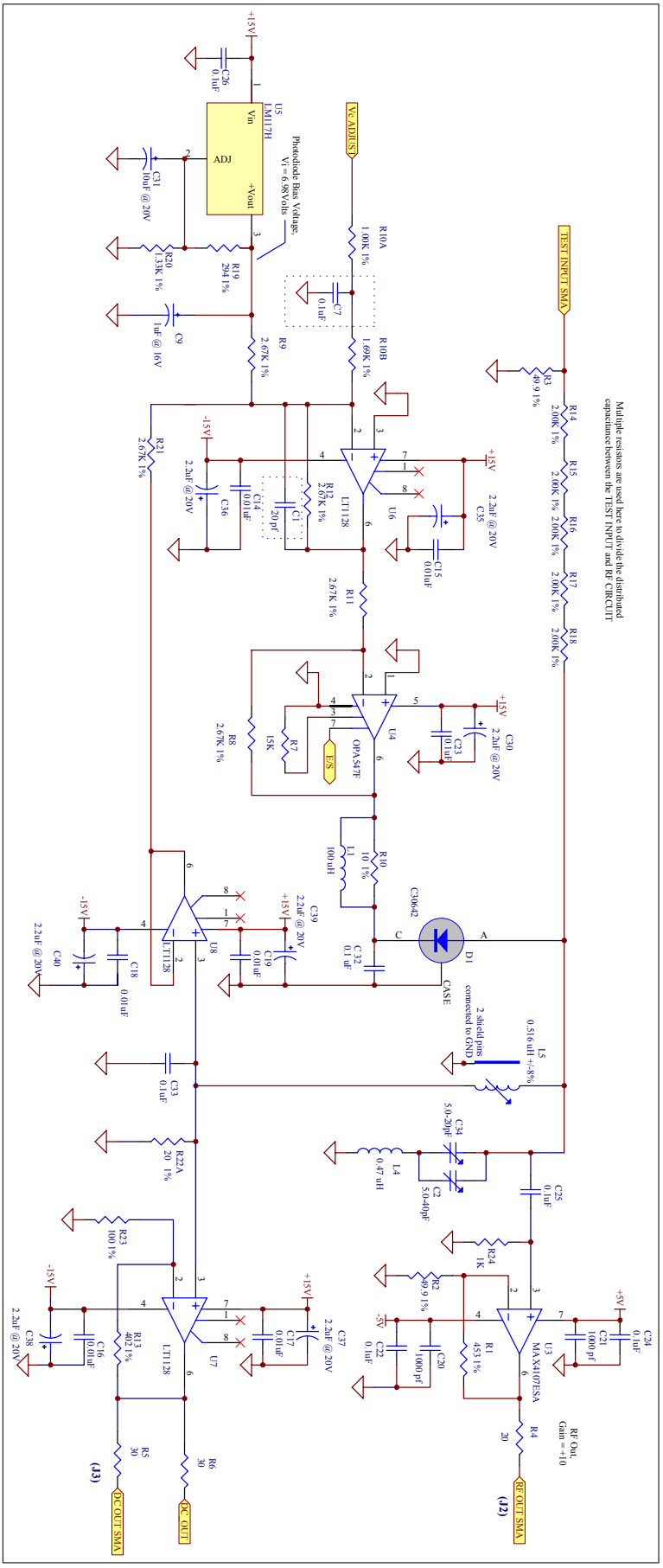

Figure C.12: 40m RF PD Circuit

- The capacitor C_{32} has the purpose of ensuring that the terminal of the photodiode is grounded at AC. It doesn't affect the resonant frequency of the resonant impedance because is is in series to the PD's capacitance.

- The RL parallel made by R_{10} and L_1 is to make the U4 (OPA547F) amplifier stable with the reactive load provided by the photodiode. The output impedance of the amplifier acts as an inductance at higher frequencies, which combines with the load capacitance C_{PD}, thus generating oscillations or peaking at the output of an amplifier. To compensate for this effect, the series isolation resistance R - provided by the RL parallel at high frequencies - is placed between the amplifier's output and C_{PD}.

Bibliography

[1] C. W. Misner, K. S. Thorne, and J. A. Wheeler. *Gravitation.* W. H. Freeman Company, New York, 1973.

[2] Daniel Sigg. Gravitational waves. In *Proceedings of TASI*, Boulder, Colorado, 1998.

[3] Rana Adhikari. *Sensitivity and Noise Analysis of 4 km Laser Interferometric Gravitational Wave Antennae.* PhD thesis, Massachusetts Institute of Technology, 2010.

[4] J. H. Taylor, L. A. Fowler, and P. M. McCulloch. Measurements of general relativistic effects in the binary pulsar psr 1913+16. *Nature*, 277(437), 1979.

[5] R.A. Hulse and J. H. Taylor. Discovery of a pulsar in a binary system. *Astrophys. J.*, 201(L55-L59), 1975.

[6] A. Abramovici, W. E. Althouse, R. W. P. Drever, Y. Gursel, S. Kawamura, F. J. Raab, D. Shoemaker, L. Sievers, R. E. Spero, K. S. Thorne, R. E. Vogt, R. Weiss, S. E. Whitcomb, , and M. E. Zucker. Ligo: The laser interferometer gravitational-wave observatory. *Science*, 56(5055):325–333, 1992.

[7] VIRGO Collaboration. The virgo project: A wide band antenna for gravitational wave detection. *Nuclear Instruments and Methods in Physics Research Section A: Accelerators, Spectrometers*, 289(3):518–525, 1990.

[8] H. Luck and the GEO600 Team. The geo600 project. *Classical and Quantum Gravity*, 14(6):1471–1476, 1997.

[9] K. Tsubono. 300m laser interferometer gravitational wave detector (tama300) in japan. In *Gravitational Wave Experiments Proc. 1st Edoardo Amaldi Conf.*, pages 112–114, Singapore, 1995. World Scientific.

[10] K. et al. Kuroda. Large-scale cryogenic gravitational wave telescope. *International Journal of Modern Physics D*, 8(5):557–579, 1999.

[11] Gregory M Harry (for the LIGO Scientific Collaboration). Advanced ligo: the next generation of gravitational wave detectors. *Class. Quantum Grav.*, 27(084006), 2010.

[12] Alberto Stochino. The ham-sas seismic isolation system for the advanced ligo gravitational wave interferometers. Master's thesis, University of Pisa, 2007.

[13] Kenji Numata. *Direct measurement of mirror thermal noise*. PhD thesis, University of Tokyo, 2002.

[14] Thomas R. Corbitt. *Quantum Noise and Radiation Pressure Effects in High Power Optical Interferometers*. PhD thesis, Massachusetts Institute of Technology, 2008.

[15] M. Punturo and et al. The third generation of gravitational wave observatories and their science reach. *Classical and Quantum Gravity*, 27(084007).

[16] Tom Prince. LISA: Probing the Universe with Gravitational Waves, 2009.

[17] Anthony Siegman. *Lasers*. University Science Books, 1986.

[18] Eric D. Black and Ryan N. Gutenkunst. An introduction to signal extraction in interferometric gravitational wave detectors. *Am. J. Phys.*, (4), 2003.

[19] Carlton M. Caves. Quantum-mechanical noise in an interferomter. *Phys. Rev. D*, 23(8), 1980.

[20] Masaki Ando. *Power recycling for an interferometric gravitational wave detector*. PhD thesis, University of Tokyo, 1998.

[21] Robert Ward. *Length sensing and control of a prototype advanced interferometric gravitational wave detector*. PhD thesis, California Institute of Technology, 2010.

[22] Daniel Sigg. Frequency Response of the LIGO Interferometer. Technical Report T970084-00-D, LIGO, 1997.

[23] Kenneth A. Strain, Guido Muller, Tom Delker, David H. Reitze, David B. Tanner, James E. Mason, Phil A. Willems, Daniel A. Shaddock, Malcolm B. Gray, Conor Mow-Lowry, , and David E. McClelland. Sensing and control in dual-recycling laser interferometer gravitational-wave detectors. *Applied Optics*, (7), 2003.

[24] R. W. P. Drever, J. L. Hall, F. V. Kowalski, J. Hough, G. M. Ford, A. J. Munley, , and H. Ward. Laser phase and frequency stabilization using an optical resonator. *Appl. Phys. B*, 31:97–105, 1983.

[25] Alan J. Weinstein. Conceptual Design of the 40 meter Laboratory Upgrade for prototyping a Advanced LIGO Interferometer. Technical Report LIGO-T010115, LIGO, 2001.

[26] Rich Abbott, Rana Adhikari, Stefan Ballmer, Lisa Barsotti, Matt Evans, Peter Fritschel, Valera Frolov, Guido Mueller, Bram Slagmolen, and Sam Waldman. Advanced LIGO Length Sensing and Control Final Design. Technical Report LIGO-T1000298T, LIGO, 2010.

[27] R. Adhikari, Y. Aso, S. Ballmer, R. Bork, J. Miller, S. Vass, R. Ward, A. Weinstein, A. Brooks, and D. Yeaton-Massey. Upgrade of the 40m interferometer. Technical Report LIGO-T080074-00-R, LIGO, 2010.

[28] Koji Arai. Courtesy.

[29] Stuart Aston and Clive Speake. Geometric osem sensor development. LIGO Document T040043-01-K, LIGO, 2004.

[30] Janeen Hazel, Mike Fine, Jay Heefner, Seiji Kawamura, and Shinji Miyoki. Small optics suspension prototype test results. LIGO Document T960179-00-D, LIGO, 1996.

[31] Bram J. J. Slagmolen, Adam Mullavey, Rana Adhikari, and David E. McClelland. Tip-tilt mirror specifications and design. LIGO Document T0900096-v1, LIGO, 2010.

[32] Eric Ponslet. Isolation stacks preliminary design methodology. LIGO Document T960026-00-D, LIGO, 1996.

[33] Kiwamu Izumi. Development of Triple Resonant EOM for Advanced Detectors. LIGO DOC G1000297, Caltech, LIGO 40m, 2010.

[34] Martin Regehr. *Signal extraction and control for an interferometric gravitational wave detector*. PhD thesis, California Institute of Technology, 1995.

[35] Nergis Mavalvala. *Alignment Issues in Laser Gravitational Wave Detectors*. PhD thesis, Massachusetts Institute of Technology, 1997.

[36] Jun Mizuno. *Comparison of optical configurations for laser interferometric gravitational wave detectors*. PhD thesis, Universitat Hannover, 1995.

[37] P. Fritschel, R. Adhikari, S. Ballmer, and M. Evans. Arm Cavity Finesse for Advanced LIGO. Technical Report T070303-01-D, LIGO, 2007.

[38] Matthew Evans. *Lock Acquisition in Resonant Optical Interferometers*. PhD thesis, California Institute of Technology, 2002.

[39] O. Miyakawa and R. Ward. Lock Acquisition Scheme for the Advanced LIGO Optical Configuration. *J. Phys.: Conf. Ser.*, 32(265), 2006.

[40] Matthew Evans. *Optickle*. LIGO, 2007. T070260-00.

[41] James Mason. *Signal Extraction and Optical Design for an Advanced Gravitational Wave Interferometer*. PhD thesis, California Institute of Technology, 2001.

[42] R Adhikari, M Evans, V Frolov, K Kawabe, N Smith, and S J Waldman. DC readout Normalization for Enhanced LIGO. LIGO DOC LIGO-T0900023-00-I, LIGO, 2009.

[43] T. M. Niebauer R. Schilling K. Danzmann A. Rudiger and W. Winkler. Nonstationary shot noise and its effect on the sensitivity of interferometers. *Physical Review A*, 43(9):5022–5029, May 1991.

[44] Koji Arai, Masaki Ando, Shigenori Moriwaki, Keita Kawabe, and Kimio Tsubono. New signal extraction scheme with harmonic demodulation for power-recycled fabry-perot-michelson interferometers. *Physics Letters A*, 273:15–24, 2000.

[45] Koji Arai and the TAMA Collaboration. Sensing and controls for power-recycling of tama300. *Class. Quantum Grav.*, 19:1843–1848, 2002.

[46] J B Camp, H Yamamoto, and S E Whitcomb. Analysis of light noise sources in a recycled Michelson interferometer with Fabry-Perot arms. *J Opt soc Am A*, 17(1):120–128, 2000.

[47] K. Somiya, Y. Chen, S. Kawamura, and N. Mio. Frequency noise and intensity noise of next-generation gravitational-wave detectors with RF/DC readout schemes. *Physical Review D*, 73, 2006.

[48] Stefan Ballmer. *LIGO interferometer operating at design sensitivity with application to gravitational radiometry.* PhD thesis, Massachusetts Institute of Technology, 2006.

[49] Koji Arai, Alberto Stochino, and Rana Adhikari. Precise measurement on longitudinal and transverse mode spacings of an optical cavity using an auxiliary laser. Technical Report LIGO-DOC G080467-00-I, LIGO, 2008.

[50] Akito Araya et al. Absolute-length determination of a long-baseline fabryperot cavity by means of resonating modulation sidebands. *Applied Optics*, 38(13), 1999.

[51] M. Rakhmanov, M. Evans, and H. Yamamoto. An optical vernier technique for in situ measurement of the length of long fabry-perot cavities. *Meas. Sci. Technol.*, 10:190–194, 1999.

[52] M. Rakhmanov, F. Bondu, O. Debieu, and R. L. Savage Jr. Characterization of the ligo 4 km fabry-perot cavities via their high-frequency dynamic responses to length and laser frequency variations. *Class. Quantum Grav.*, 21, 2004.

[53] F. M. Gardner. *Phaselock Techniques.* Wiley-Interscience, 1966.

[54] James B.Armor, Jr., and Stanley R. Robinson. Phaselock control considerations for coherently combined lasers. *Applied Optics*, 18(18), 1979.

[55] M. Rakhmanov, M. Evans, and H. Yamamoto. An optical vernier technique for in situ measurement of the length of long fabry-perot cavities. *Meas. Sci. Technol.*, 10:190–194, 1999.

[56] Hiroaki Yamamoto. Private communication, 2010.

[57] Aidan F. Brooks. *Hartmann Wavefront Sensors for Advanced Gravitational Wave Interferometers.* PhD thesis, The University of Adelaide, 2007.

[58] ISC Group. Advanced LIGO Length Sensing and Control Final DesignAdvanced LIGO Length Sensing and Control Final Design. Technical Report LIGO T1000298, LIGO, 2010.

[59] Kiwamu Izumi. *Triple Resonant EOM*. LIGO 40m, http://lhocds.ligo-wa.caltech.edu:8000/40m/Upgrade_09/Multi_Resonant_EOM. 40m Wiki.

[60] Yun Chase. *Introduction to Choosing MLC Capacitors For Bypass/Decoupling Applications*. AVX Corporation.

[61] Richard Mask Walter Jung. *Picking Capacitors, Vol I, II*, audio edition, 1980.

[62] Caryn Palatachi. Temperature Sensors for the 40m Interferometer. Technical Report T0900287, Caltech LIGO 40m, 2009.

[63] Jerald Graeme. *Photodiode Amplifiers: OP AMP Solutions*. McGraw-Hill Professional, 1995.

[64] R.E. Ziemer and W. H. Tranter. *Principles of Communications*. John Wiley & Sons Ltd; 6th International student edition), 2009.

[65] P. Horowitz and W. Hill. *The Art of Electronics*. Cambridge University Press, Second Edition), 1989.

[66] http://www.phys.ufl.edu/LIGO/LIGO/STAIC.html.